Analysis of Fiber Reinforced Plastic Bolted Flange Joints

by

Ali KHAZRAIYANVAFADAR

THESIS PRESENTED TO ÉCOLE DE TECHNOLOGIE SUPÉRIEURE IN
PARTIAL FULFILLMENT OF THE REQUIREMENTS FOR THE DEGREE
OF DOCTOR OF PHILOSOPHY
PH.D.

MONTREAL, JULY 22, 2019

ÉCOLE DE TECHNOLOGIE SUPÉRIEURE
UNIVERSITÉ DU QUÉBEC

BOARD OF EXAMINERS

THIS THESIS HAS BEEN EVALUATED

BY THE FOLLOWING BOARD OF EXAMINERS

Mr. Abdel-Hakim Bouzid, Thesis Supervisor
Département de génie mécanique at École de technologie supérieure

Mr. Anh Dung Ngô, Thesis Co-supervisor
Département de génie mécanique at École de technologie supérieure

Mrs. Wahid Maref, President of the Board of Examiners
Département de génie de la construction at École de technologie supérieure

Mr. Guilbault, Raynald, Member of the jury
Département de génie mécanique at École de technologie supérieure

Mr. Pierre Mertiny, External Evaluator
Département de génie mécanique at University of Alberta

THIS THESIS WAS PRENSENTED AND DEFENDED

IN THE PRESENCE OF A BOARD OF EXAMINERS AND PUBLIC

ON JUNE 26, 2019

AT ÉCOLE DE TECHNOLOGIE SUPÉRIEURE

"The Moving Finger writes; and, having writ,

Moves on: nor all thy Piety nor Wit

Shall lure it back to cancel half a Line,

Nor all thy Tears wash out a Word of it."

……………………………………………………………………… Omar Khayyam

ACKNOWLEDGMENT

DEDICATION

To those who devote their lives to the cause of "peace" "equality" and "freedom"

Analyse de raccords de brides boulons plastiques renforcés de fibres

Ali KHAZRAIYAN VAFADAR

RÉSUMÉ

Les composites en plastique renforcé de fibres (FRP) sont largement utilisés dans les domaines des appareils et tuyauterie sous pression. Les assemblages à brides boulonnées en FRP ont connu un développement spectaculaire dans le domaine du transport des fluides dans les systèmes de tuyauterie. Malgré l'utilisation accrue des composites de FRP dans les assemblages à brides boulonnées et la bonne connaissance de ces structures et du comportement de leurs matériaux, la procédure utilisée pour leur conception reste celle adoptée pour les brides métalliques. Cependant, les résultats sont souvent biaisés puisque celle-ci ne prend pas en considération le comportement anisotrope des brides en composites. Par conséquent, il est nécessaire de développer une approche réaliste pour procéder à une évaluation précise de la redistribution des charges dans l'assemblage afin de prédire l'intégrité des brides boulonnés en FRP.

Cette thèse présente deux modèles analytiques de brides, un sans collerette et un avec collerette. Ces modèles sont supportés par des modèles numériques par éléments finis et des essais expérimentaux. L'étude traite l'intégrité structurelle et l'étanchéité des assemblages à brides boulonnés en FRP sur la base de l'anisotropie, ainsi qu'une analyse de la flexibilité de tous les éléments de joint, à savoir le joint, les boulons et les brides. Dans les modèles analytiques des brides avec et sans collerette, la bride en composites est subdivisée en trois parties principales, à savoir: l'anneau ou la plaque annulaire, la collerette et la coque cylindrique. L'étude expérimentale, laquelle repose une approche fiable pour évaluer le modèle analytique proposé, a été réalisée sur un banc d'essai (banc d'éclatement de joints HOBT). Le banc d'essai a été modifié pour accommoder les brides NPS 3 en FRP conçu conformément à la section X du code l'ASME. Des modèles numériques 3D avec des éléments à coque anisotrope et des éléments solides ont été réalisés pour comparer et vérifier les résultats obtenus par les approches analytiques et expérimentales.

Malgré l'analyse mathématique rigoureuse et la complexité des brides composite stratifié, la comparaison des résultats a prouvé que les modèles analytiques proposés des brides en FRP avec et sans le moyeu sont efficaces, précis et fiables pour prédire la distribution des contraintes longitudinales et tangentielles dans la bride ainsi que le déplacement radial de la bride. De plus, les résultats ont montré que le modèle FE développé pour les brides en FRP avec et sans moyeu peut reproduire parfaitement le comportement des assemblages à brides boulonnés en FRP.

Mots-clef: Plastique renforcé de fibres (FRP), assemblages à brides boulonnées, Composites, Anisotropie, Assemblage avec joint plat

Analysis of fiber reinforced plastic bolted flange joints

Ali KHAZRAIYAN VAFADAR

ABSTRACT

Fiber Reinforced Plastic (FRP) composites are extensively used in the areas of pressure vessels and piping and FRP bolted flange joints have experienced a spectacular development to provide continuity for the flow of fluid through piping systems. In spite of the increased use of FRP composites in bolted flange joints and the good knowledge of these structures and their material behavior the procedure used for their design is still that of metallic flanges. There is a major concern to appropriately address the anisotropic behavior of composite materials in a flange design. Therefore, it is necessary to make a precise evaluation of the bolt and gasket loads in order to be able to predict the integrity of FRP bolted flange joints.

This thesis presents two analytical model cases; one with the flange hub and the other one without the flange hub. These models are supported by numerical finite element modeling and experimental test data. The study treats FRP bolted flange joints integrity and leak tightness based on the anisotropy and flexibility analysis of all joint elements including the gasket, bolts, and flanges. In the analytical models for the flange with and without the hub, the composite flanges are subdivided into three major categories, namely: ring flange, hub, and shell. The experimental study was carried out on a well-equipped test bench, used for Hot Blow out test of PTFE gaskets. The rig was modified to accommodate an NPS 3 FRP bolted flange joint designed according to ASME BPV Code Section X. Furthermore, three different numerical models based on 3D anisotropic layered shell and solid element models were conducted to compare and verify the results obtained from analytical and experimental approaches.

In spite of the rigorous mathematical analysis and complexity of the laminate composite flange, comparing the results proved that the proposed analytical models for FRP flanges with and without the hub, are efficient, accurate and reliable in predicting the longitudinal and tangential stress distributions on the flange surface and radial displacement of the flange. Moreover, the results demonstrated that the FE model which is developed for FRP flanges with and without the hub can depict the true behavior of FRP bolted flange joints.

Keywords: Fiber Reinforced Plastic (FRP), Bolted Flange Joints, Composites, Anisotropy, Full face gasket

TABLE OF CONTENTS

LIST OF TABLES

LIST OF FIGURES

Page

XIV

LIST OF ABBREVIATIONS

1D	One dimensions
2D	Two dimensions
3D	Three dimensions
ACP (Pre)	ANSYS Composite PrepPost
ACP (Post)	ANSYS Composite PostProcessor
Al	Aluminium
ANSI	American National Standard Institute
ASME	American Society of Mechanical Engineers
B	Bore
Ca	Calcium
DIN	Deutsches Institut Fuer Normung
EPDM	Ethylene Propylene Diene Terpolymer
f	Flange
Fe	Iron
FEM	Finite Element Model
FRP	Fiber Reinforced Plastic
GRFP	Glass Reinforced Fiber Plastic
HOBT	Hot Blowout Test
LVDT	Linear Variable Differential Transformer
Mg	Magnesium
NPS	Nominal Pipe Size

O	Oxygen
PVP	Pressure Vessel and Piping
PTFE	Polytetrafluoroethylene
Si	Silicium
Ss	Stainless Steel
UV	Ultra-violet

LIST OF SYMBOLS AND UNITS OF MEASUREMENTS

υ	Poisson ratio
β_h	Hub constant [mm]
β_s	Shell constant [mm]
ε	Strain [%]
σ_l	Longitudinal Stress [MPa]
$\sigma_{h,l,i}^n$	Longitudinal stress in the inside hub surface [MPa]
$\sigma_{h,l,o}^n$	Longitudinal stress in the outside hub surface [MPa]
$\sigma_{h,t,i}^n$	Tangential stress in the inside hub surface [MPa]
$\sigma_{h,t,o}^n$	Tangential stress in the outside hub surface [MPa]
$\sigma_{s,l,i}^n$	Longitudinal stress in the inside shell surface [MPa]
$\sigma_{s,l,o}^n$	Longitudinal stress in the outside shell surface [MPa]
$\sigma_{s,t,i}^n$	Tangential stress in the inside shell surface [MPa]
$\sigma_{s,t,o}^n$	Tangential stress in the outside shell surface [MPa]
σ_r	Radial stress [MPa]
σ_t	Tangential stress [MPa]
σ_t^r	Tensile stress [MPa]
σ_c^r	Compressive yield strength [MPa]
σ_{xy}	Stress in the xy direction [MPa]
ρ	Density [kg/m^3]
θ	Flange rotation [rad]
ψ_p^n	Rotation of the plate [rad]
ψ_h^n	Rotation of the hub [rad

ψ_s^n	Rotation of the shell [rad]
a	Constant according to the gasket [MPa]
A_b	Bolt area [mm^2]
A_g	Full gasket contact area [mm^2]
A_p	Pressure area [mm^2]
$A_{h,n}$	In-plane laminate modulus for the hub [MPA.mm]
$A_{p,n}$	In-plane laminate modulus for the ring [MPA.mm]
$A_{s,n}$	In-plane laminate modulus for the shell [MPA.mm]
A_s	Section cut area of the shell [mm^2]
b	Effective gasket seating width [mm]
$B_{h,n}$	Coupling laminate modulus for the hub [MPA.mm^2]
$B_{p,n}$	Coupling laminate modulus for the ring [MPA.mm^2]
$B_{s,n}$	Coupling laminate modulus for the shell [MPA.mm^2]
$D_{h,n}$	Flexural laminate modulus for the hub [MPA.mm^3]
$D_{p,n}$	Flexural laminate modulus for the ring [MPA.mm^3]
$D_{s,n}$	Flexural laminate modulus for the shell [MPA.mm^3]
d_b	Diameter of the bolt [mm]
E	Young Modulus [MPa]
F_B^n	Bolt force [N]
F_G^n	Gasket force [N]
G	Effective gasket diameter [mm]
G_b	Loading intercept on a tightness curve [MPa]
G_s	Unloading intercept on a tightness curve [MPa]

K_b	Bolt uniaxial stiffness [N/m]
K_g	Gasket uniaxial stiffness [N/m]
m	Gasket factor [/]
M_i^n	Discontinuity moment in the initial phase [N]
M_h^n	Discontinuity moment in the hub [N]
M_s^n	Discontinuity moment in the shell [N]
M_r	Moment resulting from r [N.mm]
M_Θ	Moment resulting from Θ [N.mm]
N	Number of bolts [/]
N_r	Stress resultant in the radial direction [N]
N_Θ	Stress resultant in direction Θ [N]
$N_{h,l}^n$	Hub longitudinal force [N]
$N_{h,t}^n$	Hub Tangential force [N]
$N_{s,l}^n$	Shell longitudinal force [N]
$N_{s,t}^n$	Shell tangential force [N]
Q_h^n	Shear force in the hub [N]
Q_s^n	Shear force in the shell [N]
Q_{rx}	Shear force in the plane rx [N]
P_w	Longitudinal stress on the wall [MPa]
p_o	Internal pressure [MPa]
P_1	Hub to cylinder discontinuity force [N/m]
P_2	Flange to hub discontinuity force [N/m]

r	Radius considered [mm]
r_b	Bolt circle [mm]
r_i	Inside radius of the flange [mm]
r_o	Outside radius of the ring [mm]
S_b	Allowable bolt stress at design temperature [MPa]
S_{ya}	Theoretical gasket seating stress [MPa]
S_{m0}	Minimum operating gasket stress [MPa]
S_{m1}	Gasket operating stress [MPa]
S_{m2}	Gasket seating stress [MPa]
T_f	Melting temperature [°C]
t_h	Hub thickness [mm]
t_f	Ring thickness [mm]
t_s	Shell thickness [mm]
T_{pmin}	Minimum tightness [/]
U	Strain energy [J]
u^f	Ring radial displacement [mm]
u_i^n	Radial displacement in the initial phase [mm]
u_h^n	Hub radial displacement [mm]
u_s^n	Shell radial displacement [mm]
V	Work done by force [J]
w	Axial displacement [mm]
w^f	Flange axial displacement [mm]
W_m	Design bolt load [N]

W_{m1}	Operating design bolt load [N]
W_{m2}	Seating design bolt load [N]
y	Gasket design seating stress [MPa]

Superscript

i	Refers to an initial tightening of the bolt condition
f	Refers to final condition (pressurization)
n	Refers to the time n

Mass

mg	Milligram
kg	Kilogram

Angel

Deg	Degree
Rad	Radian

Length/Displacement

m	Meter
mm	Millimeters
cm	Centimeter
µs	Micro strain
in	Inches

Temperature

C	Centigrade
F	Fahrenheit

Time

S   Second

H   Hours

Pressure/stress

MPa   Mega Pascal

GPa   Giga Pascal

Psi   Pounds per Square Inches

INTRODUCTION

Fiber reinforced plastic composites have recently experienced a spectacular development in the areas of pressure vessels and piping. They are used in applications ranging from water and gas services to aeronautical and petrochemical industries. Their special properties have let these composites to take precedence over traditional materials in terms of weight, chemical resistance, resistance to fatigue, low maintenance cost, and even aesthetics. Because of the ability to resist in a corrosive environment, they are extensively used in chemical and petrochemical process plants. Only some type of metallic alloys such as nickel (Ni) molybdenum (Mo) chromium (Cr) alloys can successfully survive in these conditions.

Fluid handling and transportation require safe bolted flange assemblies and pressurized equipment. Indeed, the main purpose of a bolted flange joint is to ensure the containment fluid and thus protect the immediate environment against contamination from leakage of harmful fluids or fluid escapes that are nauseating, toxic, and dangerous. In the first case, the loss of such a harmless fluid primarily results in a reduction in the efficiency of the installation, although such joint failure may present hazards such as leakage of steam under pressure. In the second case, the leak does not only represent a decline in the performance of the pressure vessel but also it is dangerous for the environment and humans (Bouzid et al. 2007). Therefore, a proper choice of materials in bolted flange joints for a particular process is an important responsibility of the user and the designer, in terms of compliance with laws, regulations, and standards of calculation. In addition, it is important to note that the performance of bolted flange joints depends on the interaction of the various components of the system and satisfactory performance of joints can only be expected if all the system components work together in harmony.

Despite the increased use of FRP composites in pressurized tanks and piping plants, limited information is available on the mechanical analysis of certain components, especially in bolted flange joints. Even though the ASME BPV Code Section X (American Society of Mechanical

Engineers), ASME RTP-1 as well as other standards such as standard D4024, the British Standard BS 71 59 have developed rules for the design, manufacturing techniques and inspection of pressure vessels made of fiber-reinforced plastic, the theories that are used in the analysis of composite flanges are more or less modified versions of the theories used for metallic flanges. But the mechanical behavior of composite materials is different from metallic materials, because of their anisotropy and their inhomogeneity, so that the results obtained in using these design codes cannot explain the significant behavior of composite flanges.

To investigate the behavior of fiber reinforced plastic bolted flange joints, some research has already been done as shown in Sun's thesis (1995), which is focused on the behavior of FRP flanges by proposing an analytical and numerical study. But it turns out that the analytical results are not in good agreement with the results obtained from the numerical model because of some assumptions that make some errors in the analytical model. Blach et al. (1990) use the laminate theory to propose a method for a stress analysis of fiber reinforced plastic flanged connections with full face gaskets. They used a few assumptions to simplify their proposed method. Although they used rigorous mathematical analysis to describe all the complexity of the laminate materials, their method does not satisfy all the physical constraints associated with such composites. Kurz and Roos (2012), studied the mechanical behavior of floating type bolted flanged connections with glass reinforced plastic flanges, analytically and experimentally. In their study, they divided the flange into two small angular portions and considered as a beam clamped at one end subjected to bending. Thus, the design leads to virtual radial stress which only represents the usage level of the flange. The analytical model that Estrada and Parsons (1997) suggested in their study to describe the circumferential stresses and rotation shows good agreement with the results obtained from finite element simulation and experimentation. Campbell (1990) proposed a new technique to fabricate FRP flange that is the adoption of the one-piece integral flange. His design was based on the metal flange counterpart given by ASME B16.5. Black et al. (1995) suggested a simple design method for FRP flanges with full face gaskets but according to Bouzid (2011) bolts and gasket flexibility as well as the elastic interaction between them are neglected. It is worth noting that in designing

FRP flanges, the impact of temperature on the stress redistribution is not explained like with metal flanges (Nechache and Bouzid 2007).

An overview of all researches done on FRP bolted flanged joints, shows that most of the proposed analytical models are based on metallic flange design. While, to have an accurate stress analysis in all part of FRP flange joints, it is necessary to choose a reliable method of design which describes the anisotropic behavior of FRP materials. Moreover, according to Czerwinski J (2012), very few papers deal with leak rate measurements in FRP bolted flange joints.

The elements that influence the behavior of flanges and especially composite flanges in the operating conditions are countless, so it becomes necessary to study comprehensively FRP bolted flange joints to address specific issues related to these elements. This work aims both to study the actual behavior of FRP bolted flange joints and also to evaluate their performance compared with metal flanges in order to provide the possibility of using composite flanges as an alternative to metallic bolted joints with the same geometry. In order to study of FRP bolted flange joints comprehensively, a combination of analytical, experimental and numerical investigation techniques is used.

The content of this thesis is organized into five chapters. All chapters have been written and presented in a constructive manner for ease of understanding of the reader. The first chapter is dedicated to the literature review and extensive and qualitative reviews of different types of bolted flange joints with particular focus on FRP bolted flange joints. This chapter also presents the properties and the anisotropic character of composite materials and exposes the peculiarity of the study of composite vessels in the domain of bolted flange joints.

Chapter 2 outlines the analytical approaches of FRP bolted flange joints. In this chapter, two analytical models were developed to treat FRP bolted joint structural integrity and leak tightness based on anisotropic behavior and taking into account the flexibility analysis of all joint elements including the gasket, bolts, and flanges. Since the analytical study is the essence

of this research, a detailed explanation of the theories and equations for each part of the flange with the highest accuracy is vital. In the analytical models (one for the flange with the hub and one for the flange without the hub), the composite flanges are subdivided into three major categories, namely: ring flange, hub and shell, and the procedure for each part of the flange is described in detail.

The numerical study of FRP bolted flange joints is elaborated in the third chapter. The presented numerical models of FRP bolted flange joints in this chapter are an attempt to develop and validate the analytical model. The finite element analysis makes it possible to obtain an approximate solution of a physical problem by providing algebraic stiffness equations to solve the problem. This chapter describes the procedure of three different finite element models; a flange with the hub and without the hub and a multilayer shell model using ANSYS Composite PrepPost. Fiber reinforced plastic bolted flange joints of two sizes; NPS 3 class 150 and NPS 12 class 150 flanges are treated. To create and analyzed the finite element models, the program ANSYS® Mechanical 16.02 and the ANSYS Composite PrepPost (ACP) 16.2 were used. The geometry of flanges as well as laminate properties and the stacking sequence of the laminate used in the composite flange are presented in this chapter.

It was considered necessary to set up a test rig to investigate the real behavior of FRP bolted flange joints and use experimental results to verify and characterize the presented analytical and numerical models in the second and third chapter. Thus, the fourth chapter is dedicated to describe the operational mechanisms of the Hot Blow Out Test Bench (HOBT) and the experimental procedure involved in this characterization study. FRP flange and test rig in this study were developed for the purpose of measuring the parameters related to the analytical and numerical models of this research work.

Chapter five is devoted to present the results obtained from the analytical, numerical and experimental analysis of FRP bolted flange joints. In this chapter, discussion and comparison of the results shown in graphs and tables are performed.

Finally, this thesis concludes with a broad conclusion highlighting the main results of the work conducted on FRP bolted flange joints. Furthermore, a few recommendations are suggested for the future works in this research area.

CHAPTER 1

LITERATURE REVIEW

1.1   Introduction

Most of the research conducted on composite bolted flanged joints, especially fiber reinforced plastic flanges, focuses on transferring the knowledge from metallic flange designs to composite flange designs. Since FRP flanges do not behave like isotropic materials (Estrada, 1997), (Hoa, 1991) designers have to rely on criteria based primarily on anisotropic designs and also other methods of analysis. In this chapter, some of the recent research work is reviewed which is one of the sources of instigation of this study objective. To present an extensive review of existing scientific articles and dissertations, this chapter is divided into four subsections:

1- FRP flanges, standards and design codes,
2- Analytical studies,
3- Numerical (Finite Element) studies and,
4- Experimental studies.

The next part presents a general introduction of FRP bolted flange joints as well as composite materials and the codes and standards of these materials. But before going deeper into these rules, especially those of ASME BPV Code Section X it is necessary to understand the different aspects of FRP bolted flange joints. Then, the existing analytical studies of FRP bolted flange joints are elaborated. The third part of this chapter presents the numerical finite element models used to simulate the behavior of FRP flanges. The fourth part discusses the experimental investigations and test procedures as well as the experimental results.

1.2   Fiber reinforced plastic (FRP)

Fiber reinforced plastics are composites made by reinforcing a resin with fibers. Using the Fiber reinforced plastic composite in the pressure vessels need special attention to the

fabrication techniques, design and testing of these structures. Pressure vessels which are made from metallic materials that are normally isotropic and ductile. These vessels are designed by using well-established allowable stresses based on measured tensile and ductility properties (ASME BPV Code Section X). In the form of composite like fiber reinforced plastic, a designer can take advantage of the propitious properties of these materials. In FRP, the strength and stiffness of the composite are provided by the fibers and the resin used as a binder to provide other favorable properties such as corrosion resistance, impact resistance and compressive strength. The anisotropic behavior of FRP material makes this composite separate from isotropic materials like metals. In an anisotropic material, the mechanical properties in each direction are different and it depends on the direction of the fibers. Higher-strength and stiffness to weight ratios is another advantage of FRP composites that make them dominant compared to other materials such as steel. (Blach et al. 1987).

Composites have replaced many traditional materials and provided users with longer-lasting equipment. These products created a history of successful field experience of long-term use of composites under specific conditions. Fiber reinforced plastics laminates may have a modulus of elasticity as low as 6894.76 MPa (1.0×10^6 psi), compared with that of ferrous materials which may be of the order of 20,6842.71 MPa (30×10^6 psi) (ASME BPV Code Section X). This low modulus characteristic requires careful consideration of vessel profile in order to minimize bending and avoid buckling.

1.2.1 Material Systems (fibers and resins)

Thermoplastic resins are capable of being repeatedly softened and hardened by an increase and decrease of temperature. This change upon heating is mainly a physical rather than a chemical feature (Gendre, L. 2011).

Because of the lower creep resistance and thermal stability, thermoplastic resins are not used as composite flanges. In general, thermoplastic polymers have higher strains to failure than

thermoset polymers, which may provide better resistance to matrix micro-cracking in a composite laminate. Popular types of thermoplastic resins include:

- Polyvinyl chloride (PVC);
- Chlorinated polyvinyl chloride (CPVC);
- Polybutylene (PB);
- Polyethylene (PE);
- Polyvinylidene chloride (PVDC);
- Polyvinylidene fluoride (PVDF);

Thermoset plastics, do not flow under the application of heat and pressure. However, when exposed to heat or chemical environments, change into practically infusible and insoluble materials. Thermoset resins are more commonly used with FRP products and exhibit less creep and stress relaxation than thermoplastic polymers. They show superior thermal stability. In the ASME BPV Code, Section X, thermoset resins include:

- Polyesters;
- Epoxies;
- Vinyl esters;
- Phenolics;
- Furan;

In the (ASME BPV Code, Section X), reinforcements embedded in a resin matrix are a combination of fibers such as:

- Glass (Type A, E, S, C);
- Carbon;
- Graphite;
- Aramid;

Glass fibers are used in most composite materials as reinforcement in many fields such as constructions, transport, optics, and sports. The reasons for these diverse applications are the

excellent properties they offer such as tensile strength that is twice as strong as steel, thermal insulation, dimensional stability, and low moisture absorption. Polyester and vinyl ester are corrosion resistance resins that are used in a wide range of pressure vessels such as tanks, pipes, ducting, chemical plant equipment because of these properties. In addition, a relatively low cost of glass fibers, making it competitive with other fibers.

1.2.2 General Fabrication Techniques

There are several methods or manufacturing process for FRP flange production such as contact molding or hand lay-up, injection molding, filament winding, compression molding, resin transfer molding and centrifugal casting (Rosato et al. 1964). The following methods are mostly used in FRP flange production:
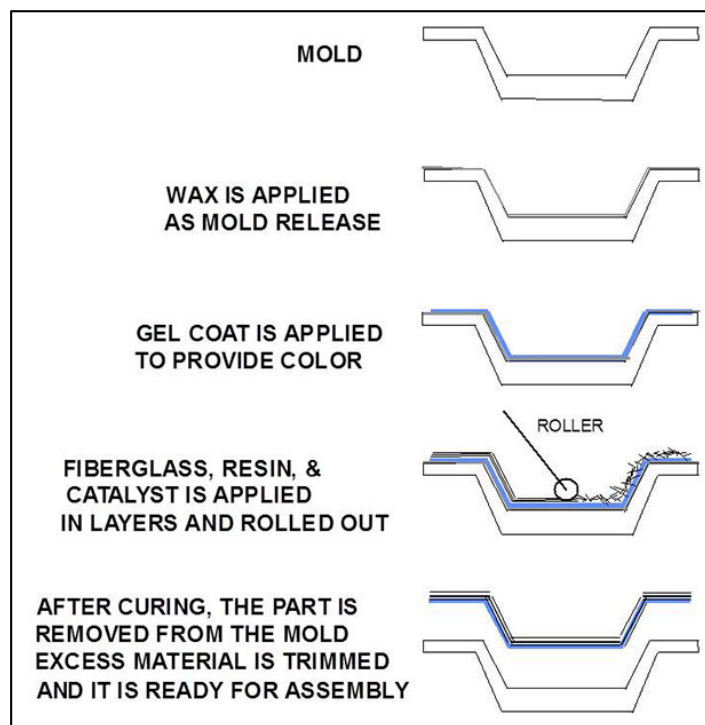
Figure 1-1 Contact molding process (Black et al. 1995)

1- *Contact Molding:*

In this method, cylindrical sections, heads, and attachments are fabricated by applying reinforcement fibers and resin to a mandrel or mold. System cure is either at room temperature or elevated temperature using a catalyst-promoter system. The contact molding process is depicted in figure 1.1. As shown in the figure each ply is applied one by one, paying attention to ensuring that the recommended orientation is respected and that no air bubbles seep into the resin. The resin is applied with a brush or a gun between each ply.
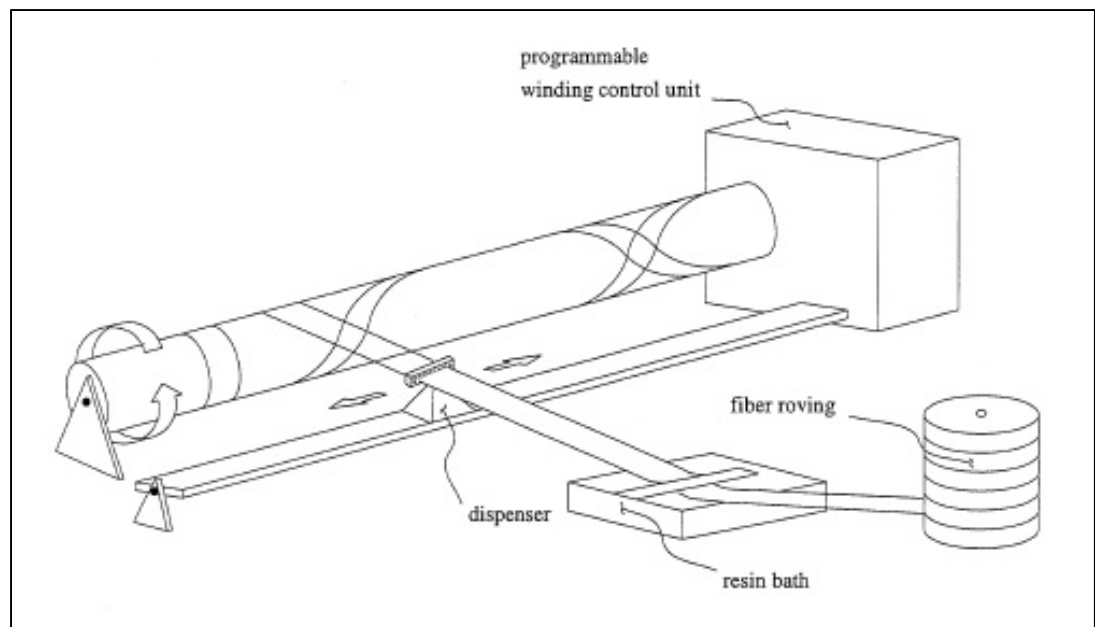
Figure 1-2 Filament winding process (Estrada 1997)

1- *Filament Winding*

In this process, continuous filaments of fiber wetted with the specified resin are wound in a systematic manner under controlled tension and cured on a mandrel or other supporting structure. The filament winding process is shown in figure 1.2. Heads and fittings fabricated by contact-molding methods may be attached with suitable adhesive resins and secondary reinforcement with the cutting of filaments as required. Heads are

integrally wound and the only openings allowed are those centered on the axis of rotation and are wound into the vessel during fabrication.

1.3   Bolted Flanged Joints

In order to connect piping systems and pressure vessels containing fluids or gas under pressure, the most reliable way is to use bolted flanged joints. Flanges are used as an alternative to welding or threading different pipelines components and pressure vessels. In addition, bolted flange joints that are the alternative to welding because they can be easily assembled, disassembled, then reassembled when needed for shipping, inspection, maintenance, and replacement (Derenne et al. 2000).
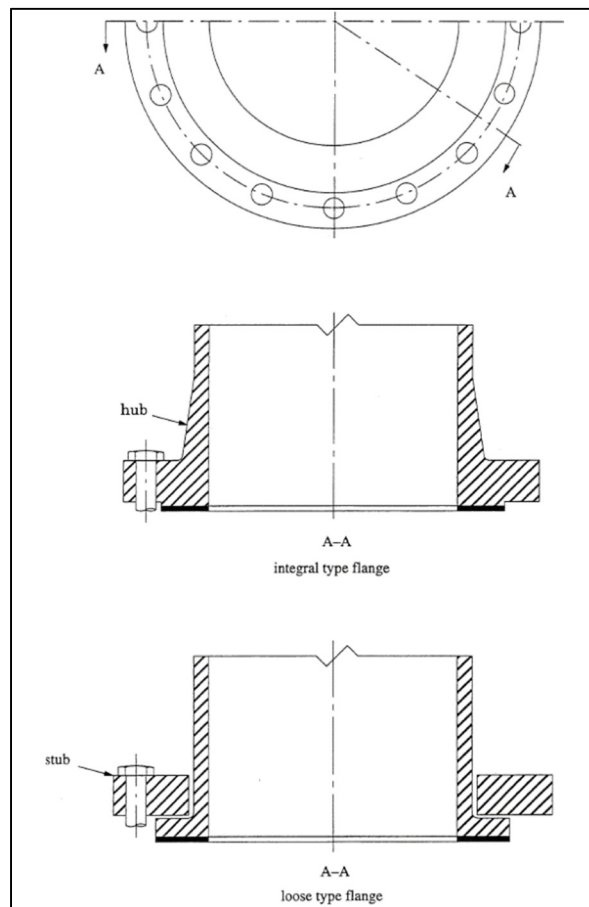
Figure 1-3 FRP Flanged Joints (Estrada 1997)

Due to the leakage in the large-bore threaded pipe and also threading pipe is not reliable and economical, flanged connections are favored over threaded connections. For these reasons, flanges are important components of any piping system. There are two types of the metallic bolted flanged joint shown in Figure. 1.3; integral flange and loose flange.

Figure. 1.4 depicts two varieties of the integral flange geometry. As shown in this figure, raised face flanges are used for the applications at high pressure while flat face flanges are used for low pressures applications. Flat-faced flanges are typically used with full face gaskets and ring gaskets for the flanges with and without the hub respectively.
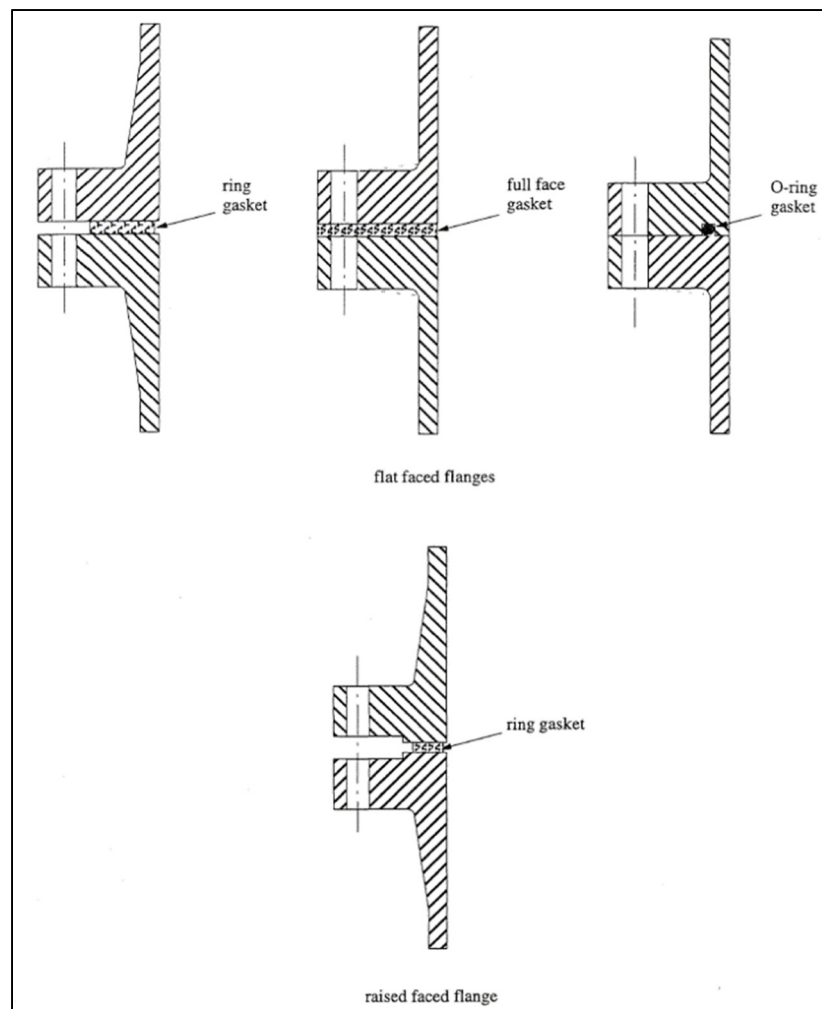
Figure 1-4 Conventional Metallic Flanged Joints (Estrada 1997)

Due to the greater contact area in the flanges with full face gaskets, they need greater load applied by the bolts to make them sealed. Therefore, to maintain the flanges sealed the gasket should deform plastically to close all the porosities on the flange face. The flange contact occurs inside the bolt circle of the raised face flanges and flat face flanges with ring gaskets. As a result, relatively higher flange rotation occurs when the joint is bolted leading to high bending stresses at the hub-to-cylinder junction.

1.3.1   Fiber reinforced plastic bolted flange joints

There are commonly two types of flange known as FRP bolted joints:

1- Stub flanges;

2- Flat face flanges with full face gaskets;

There are two general fabrication procedures used in the production of contact molded fiber reinforced plastic flanges; the first method is two-piece construction that the flange is laid-up directly onto a piece of pipe or a cylindrical pressure vessel shell. The second one is one-piece construction that the continuous axial glass fibers wetted with resin, made a continuous form of the shell and hub into layers of the flange. It is necessary to mention that the one-piece integral flange eliminates all the problems associated with the bond of the two-piece construction and this method has been used successfully in industry application for almost two decades [Sun et al. 1995].

FRP bolted joints present more difficulties in design and operation than their metallic counterparts. This is because their material properties are more complex and the bolting requirements are different. Although the bolt holes in metallic flanges make a slight material discontinuity problem, drilling the bolt holes in FRP composite flanges can be significant, particularly in filament wound joints. In the composite flanges that are made with the hand lay-up manufacturing technique, this problem is solved by incorporating the holes in the flange during the manufacturing process. The field of application of these vessels varies since they are used in most industrial domains, in particular in the

petrochemical and nuclear industries. It is worth noting that because of their anisotropic behavior, the study of composite flanges is much more complex than for metal flanges.

1.3.2 Design codes and standards for FRP bolted flange joints

There are two standards for fiber reinforced plastic flange joints**:**

1.3.2.1 PS 15-69

The first FRP flange standard from the national bureau of standards voluntary product standard, PS 15-69, appeared in 1969. This standard presents the minimum values of the flange thickness as well as the specifications for bolting system of FRP flanges including all metal washers, nut and bolt heads. In general, PS 15-69 covers some type of FRP flanges such as contact molded flanges and gives guidelines to keep their use in the safe zone with the butt-strap joint recommended as the standard pressure vessel connections. In addition to this standard, ASTM added the specifications for the fabrication techniques (Filament winding and contact molding) of FRP flanges. However, this standard doesn't cover flange design and only covers the specifications that are based on FRP flange performance. Technically, this standard becomes an updated version of the PS 15-69 standard. But there is a difference between these two standards in being proof tested and is listed in table 1.1. The performance requires to the leakage test for sealing of FRP flange with the 1.5 times higher pressure of the design pressure and test with four times higher pressure of the design pressure period of the one-minute period for rupture strength. On the other hand, the composite material of contact molded flange should be able to resist about two times of recommended bolt torque by the manufacturer, and other flange construction should be able to resist 1.5 times bolt torque without visible signs of damage.

This standard gives no specification for the gasket and bolting system, instead, it suggests to follow the manufacturer's recommendation. It also mentions that flanges fabricated with different techniques and different manufacturers with identical classification can not be interchangeable because the pressure vessels and piping systems need to get standardized.

Table 1-1 FRP joint standard, PS 15-69

Nominal Pipe Size (I.D.)	Wall Thickness	Flange Diameter (O.D.)	Flange Thickness	Bolt Circle Diameter[3]	Bolt Hole Diameter	Number of Bolts
2	1/8	63/8	1/4	5	7/16	4
3	1/8	73/8	1/4	6	7/16	4
4	1/8	83/8	1/4	7	7/16	4
6	1/8	103/8	1/4	9	7/16	8
8	1/8	123/8	1/4	11	7/16	8
10	1/8	143/8	3/8	13	7/16	12
12	1/8	163/8	3/8	15	7/16	12
14	1/8	183/8	3/8	17	7/16	12
16	1/8	203/8	1/2	19	7/16	16
18	1/8	223/8	1/2	21	7/16	16
20	1/8	243/8	1/2	23	7/16	20
24	3/16	283/8	1/2	27	7/16	20
30	3/16	343/8	1/2	33	7/16	28
36	3/16	403/8	1/2	39	7/16	32
42	1/4	463/8	5/8	45	7/16	36
48	1/4	543/8	5/8	52	9/16	44
54	1/4	603/8	5/8	58	9/16	44
60	1/4	663/8	5/8	64	9/16	52

1.3.2.2   ASME Boiler and Pressure Vessel Code Section X

ASME code section X covers the design rules for FRP pressure vessels and piping systems. In this standard, the pressure vessels are qualified by two class designs:

1. Class I design – this method qualifies the design through the destructive test of a prototype.
2. Class II design – this method qualifies the design through acceptance testing by non-destructive methods and mandatory design rules.

Class II flange design rules are based on the same mandatory rules as their metallic counterparts. These rules are standard rated flanges and flange design calculations. Standard rated flange design is based on ANSI flanges as the PS 15-69 standard. Not only, the ASME Section X code design calcu1ation of FRP flanges is similar to that of metallic flanges known as Taylor Forge method but it assumes FRP materials to be isotropic as in steel. The only

difference in design is the allowable stresses which incorporate a higher safety factor. According to the code, the flange design stresses vary depending on the type of stress. Therefore, designing the flange based on hoop strength against internal pressure, the range of design stress may vary from 11.03 MPa (1,600 psi) to 21.37 MPa (3,100 psi). In addition, the design stress for inter-plies shear strength may be as low as 0.69 MPa and also the intermittent loads' design stress may reach as high as 24.13 MPa (100 psi). Nevertheless, flange design stresses over 24.13 MPa (3,500 psi) are rare. In order to design FRP flanges using these methods, an additional stress check namely the radial stress at the bolt circle is used. Class II design recommended that the maximum pressure for vessels are limited to 0.52 MPa (75 psi) and the maximum inside diameter is limited to 243.84 cm (96 inches).

The relevant ASME BPV code section X comprises the design rules for fiber reinforced bolted flange joints. The flange and nozzle dimensions in ASME BPV code section X are listed in table 1.2. According to this standard, there are several modulus values in the mechanical properties of FRP material such as hoop tensile modulus, axial tensile modulus, and an axial compressive modulus. It is exceedingly important that the flange designer while designing the flanges in particular FRP flanges takes this into account the anisotropic properties of composite material. Hence, understand the anisotropic behavior of FRP materials would be a proper assumption for a designer. No additional calculations are required when a flange is selected from this standard.

In some applications of FRP vessels where special joints can be utilized such as downhole tubing, high pressures about hundreds of MPa can be attained. Design pressure is the permissible pressure in the vessel which is the maximum applicable pressure at the laminate of the vessel. In piping systems and pressure vessels of FRP materials, the temperature range is much smaller compared to metallic vessels and piping such as carbon and stainless steels and copper-nickel. Also, the design temperature is less than the interior laminate wall temperature expected under operating conditions for the part considered and is less than 10°C, or 1.667°C below the glass transition temperature of the resin, whichever is lower.

Table 1-2 Flange and nozzle dimensions, ASME Boiler and Pressure Vessel Code Section X
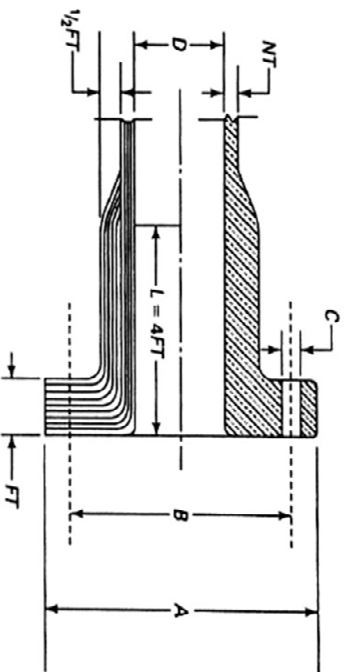
TABLE RD-620.1
FLANGE AND NOZZLE DIMENSIONS FOR HAND LAY-UP AND PRESSURE MOLDED FLANGES

U.S. Customary Units, in. and psi

Size, in.	Outside Dia., A	Bolt Circle, B	Bolt Hole Dia., C	Dia. Spot Facing	Bolts, Size Dia.	No. of Bolts	25 FT	25 NT	50 FT	50 NT	75 FT	75 NT	100 FT	100 NT	125 FT	125 NT	150 FT	150 NT	Gusset Spacing
1	4¼	3⅛	⅝	1⁹⁄₁₆	½	4	¼	¼	¼	¼	¼	¼	⁵⁄₁₆	¼	⅜	¼	¼	¼	10½
2	5	3⅞	⅝	1⁹⁄₁₆	½	4	¼	¼	¼	¼	¼	¼	⁹⁄₁₆	⅝	¹¹⁄₁₆	¾	¾	¹¹⁄₁₆	11
3	6	4½	¾	1¾	⅝	4	¼	¼	¼	¼	1¹⁄₁₆	¼	¾	⅝	1¹⁄₁₆	¾	¾	¼	12
4	7½	6	¾	1¾	⅝	4	¼	¼	½	¼	1¼	¼	⅞	⅝	1¼	⁵⁄₁₆	1	⁵⁄₁₆	13½
6	9	7½	⅞	2	¾	8	1¹³⁄₁₆	⁵⁄₁₆	1¹³⁄₁₆	⁵⁄₁₆	1¹³⁄₁₆	⁵⁄₁₆	1	⁵⁄₁₆	1	⅜	1⅛	⁷⁄₁₆	15
8	13½	11½	⅞	2	¾	8	⅜	½	¾	¾	1	⅜	1⅛	⁷⁄₁₆	1⅜	½	1⅝	½	17
10	16	14¼	1	2¼	⅞	12	¼	¼	1	1	1⅛	⅜	1¼	⁷⁄₁₆	1½	⁷⁄₁₆	1½	⁹⁄₁₆	19½
12	19	17	1	2¼	⅞	12	¹³⁄₁₆	¼	1	⁵⁄₁₆	1½	⁷⁄₁₆	1½	½	1¹¹⁄₁₆	⁹⁄₁₆	1¹¹⁄₁₆	1¹¹⁄₁₆	19½
14	21	18¾	1⅛	2½	1	12	⁵⁄₁₆	⁵⁄₁₆	1⅛	⅜	1⅜	⁷⁄₁₆	1⅞	⁹⁄₁₆	1⅞	¹¹⁄₁₆	1¹⁵⁄₁₆	(1)	19½
16	23½	21¼	1⅛	2½	1	16	⁵⁄₁₆	⁵⁄₁₆	1¼	⅜	1½	½	1¹¹⁄₁₆	⅝	2	¾	2½	(1)	19½
18	25	22¾	1⅛	2¾	1⅛	16	⁵⁄₁₆	⁵⁄₁₆	1⅛	⁹⁄₁₆	1⅞	⁹⁄₁₆	(1)	(1)	(1)	(1)	2⅛	(1)	19½
20	27½	25	1⅛	2¾	1⅛	20	1⅛	⁵⁄₁₆	1½	⁷⁄₁₆	1¹¹⁄₁₆	⁹⁄₁₆	(1)	(1)	(1)	(1)	(1)	(1)	19½
24	32	29½	1⅜	3	1¼	20	1¼	⅜	2	½	2	¾	(1)	(1)	(1)	(1)	(1)	(1)	19½
30	38¾	36	1⅜	3	1½	28	1½	¾	2⅜	¹³⁄₁₆	2⅜	¹³⁄₁₆	(1)	(1)	(1)	(1)	(1)	(1)	19½
36	46	42¾	1⅜	3½	1½	32	2	⁵⁄₁₆	2	¹¹⁄₁₆	(1)	(1)	(1)	(1)	(1)	(1)	(1)	(1)	19½
42	53	49½	1⅝	3½	1½	36	2⅛	⁷⁄₁₆	2⅝	⅞	(1)	(1)	(1)	(1)	(1)	(1)	(1)	(1)	19½
48	59½	56	1⅝	3½	1½	44	2¼	½	3	⅞	(1)	(1)	(1)	(1)	(1)	(1)	(1)	(1)	19½

1.4   Analytical studies

The analysis of FRP flanges is very complicated and the general solution always goes through a cumbersome computer program. Because of the anisotropic behavior of composite bolted flanges, there is a general use of simplifying assumptions that can sometimes affect the accuracy of the results obtained from the developed model.

Estrada (1997) proposed a model that includes four distinct axisymmetric structural components that are analyzed separately. The exact model and flange geometry and loading is depicted in figure 1.5. He modifies the model for the composite component to account for orthotropic material properties using classical lamination theory. Figure 1.6 illustrates the body diagram of the model, flange geometry and loading. This is the simplest way to analyze this structure because of the complication of the boundary conditions. He performed the analyses on a modified stub flanged joint which is shown in figure 1.7.

This GFRP (Glass Fiber Reinforced Plastic) joint is a modified version of a typical GFRP joint, the stub flanged joint developed by Estrada et al (1997) to address some problems particular to GFRP joint geometries currently in use. The pipe and the hub are filament wound and form an integral unit. The backing ring is metallic and is used to connect the joint to other members. He analyzed the flange in two parts: the stub and the pipe-hub. He modeled the stub as an isotropic annular plate with an inner ring stiffener and the pipe-hub as two separate orthotropic axisymmetric shells.

Stub:
The stub is analyzed as two distinct linear elastic isotropic components: a ring stiffener and an annular plate. The ring is modeled as a reinforcing ring subjected to an axial moment. In order to reduce the number of unknown parameters, they used the assumption that the ring stiffener thickness is half of the annular plate thickness.
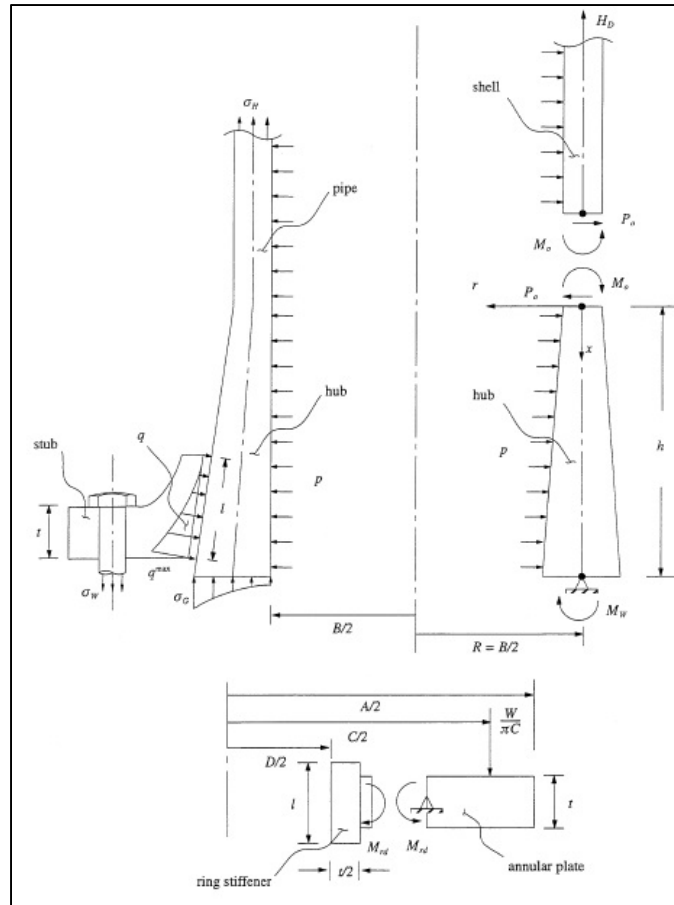
Figure 1-5 Exact model and flange geometry and
loading (Estrada, 1997)

Pipe-hub:

The pipe-hub is modeled analytically by dividing into two structural sections which were analyzed separately. These two sections are analyzed using shell theory and the shell with variable thickness theory. The solutions for the two sections were obtained from classical laminated shell theory in terms of parameters that depend on the end conditions for each section. They modeled the cylindrical shell as an axisymmetric laminated shell and the tapered hub as an axisymmetric laminated cylindrical shell of variable thickness. Also, they reduced the strain-displacement relations, kinematic assumptions, equilibrium equations and constitutive law to a single equation.
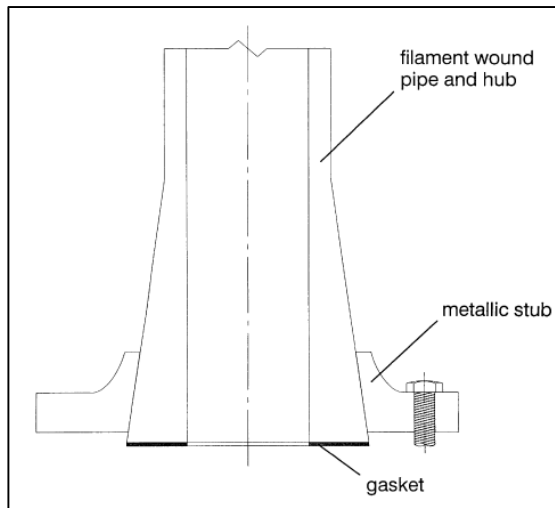
Figure 1-6 Modeling stub flange
(Estrada, 1997)
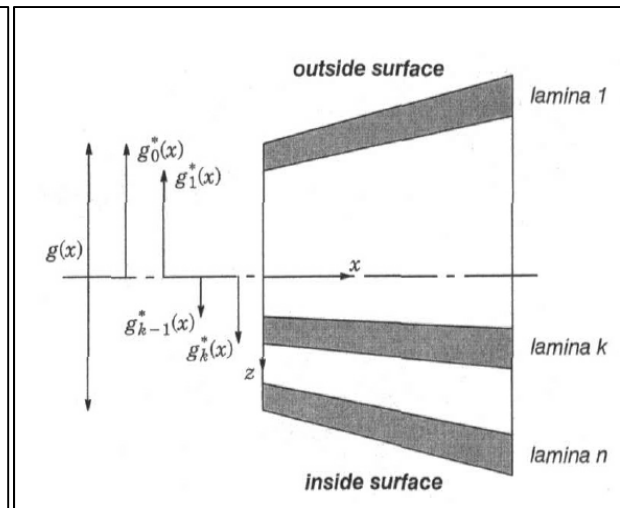
Figure 1-7 Laminate geometry for the tapered
laminated shell (Estrada, 1997)

1.4.1 Classical lamination theory

The theory of mechanics of composite materials is based on the lamination theory which is the main theory used for the composite materials. In the microscopic scale, a composite is defined as a complex system consisting of matrix and fibers combined to make a monolithic compound. But the definition of composite material in this theory is a material system with enhanced material properties that is made from a combination of chemically distinct materials on the macro-scale bonded together by a distinct interface. This theory mainly used to analyze the composite system which is made in layers and each layer consisting of parallel fibers embedded in a matrix. In order to fabricate a laminate, laminae are stacked in a specified sequence of orientation and this sequence of orientation can allow the designer to meet the demanding mechanical properties of the composite. Lamination theory can be summarized as the development of equations that relate generalized strains to generalized forces through the constitutive law. According to ASTM Standard Specification D5421, the material properties in composites are simplified by the assumption that the properties of fiber and matrix can be combined into an effective transversely isotropic material layer.

Some of the assumptions to simplify the calculations that are stated in this theory:

1. The laminas in a laminate are perfectly bonded together.
2. Each layer is of linear varying thickness. Each lamina has an equal thickness at the large end ($g_1 = nt_1$) and at the small end ($g_0 = nt_o$) and varies linearly along the axial direction.
3. Each lamina acts as a homogeneous transversely isotropic linear elastic system.
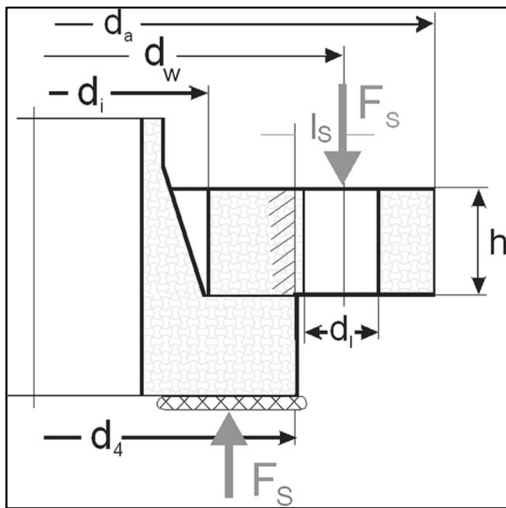
Figure 1-8 Loading situation defined in AD-Merkblatt N1 (Kurz et al. 2012)
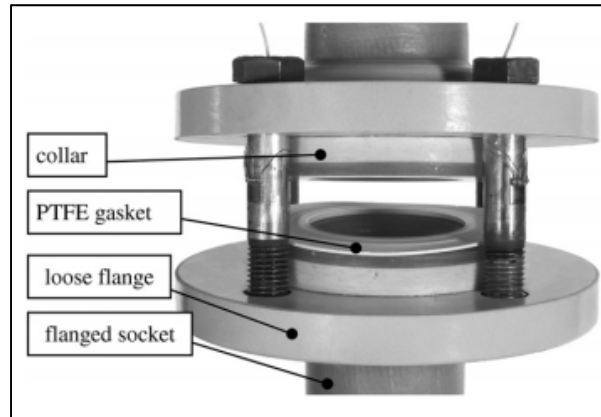
Figure 1-9 Floating type bolted flange connection with GRP flange (Kurz et al. 2012)

Kurz and Roos (2012), conducted an analytical and experimental evaluation of the mechanical behavior of floating type bolted flanged connections with glass reinforced plastic flanges that are depicted in figure 1.8. They modeled the bolted flange connection according to AD-Merkblatt N1, shown in figure 1.9. The design is based on bending of a beam clamped at one end. Thus, the design leads to virtual radial stress which only represents the usage level of the flange. Their model describes analytically the circumferential stresses and the rotation and shows a good agreement with the results of the FE simulation and the experimental investigations.

Blach and Hoa (1987), conducted a study on full-face FRP flanged joints. They proposed two design methods which can be used safely for these flanges. The first one is based on the Taylor Forge method (Anonymous, 1979). and the second one is based on the method of composite materials. They conducted a 3D finite element analysis on FRP flanges with full-faced gasket and tried to correlate data obtained from experimental tests. The results obtained from the metallic design methods and the FE modeling of FRP flanges seem to have a good agreement with the experimental results. In their study, some problems of FRP bolted flange joints are discussed, such as a certain amount of convex distortion (pullback) that can be caused in hand lay-up flanges due to uneven curing of the resin. If the distortion is straightened by bolt load alone, there would be excessive stress at the junction of the flange and cylinder.

Blach and Sun (1990), proposed a method for analyzing the stresses of fiber reinforced plastic flanged connections with full face gaskets based on classical laminates theory, shear deformation laminate theory and shell theory for the different components of the flange. This method is simplified by using a few assumptions and is based on rigorous mathematical analysis. Also, this method could not satisfy all of the physical constraints due to the complexity of the laminate problem. They claim that the analytical developed method is much more accurate than that obtained by using any of the greatly simplified customary design method based on metallic flanges. Unfortunately, the proposed method is not suitable for flange designers because the solution requires the use of infinite series expansion.

Sun, L. (1995) proposed two methods of stress analysis based on shear deformation laminated theory and classical lamination theory for the full-faced FRP bolted flange joints. In the first method which is based on the classical lamination theory, the transverse shear deformation is neglected. In the second method, the classical lamination theory is applied to the shell but the ring is modeled by using a formulation that accounts for transverse shear deformation. The method appears to represent an improvement over the approach that Waters et al. (1937) used in the derivation of the Taylor forge method, accounting for FRP material properties. As shown in figure 1. 10, in his analytical model, the flange is separated into two parts. The final solution is obtained by applying the boundary conditions and continuity conditions. Due to the poor

mesh elements used in the numerical finite element model, the results obtained from the finite element model and analytical model are not in good agreement.
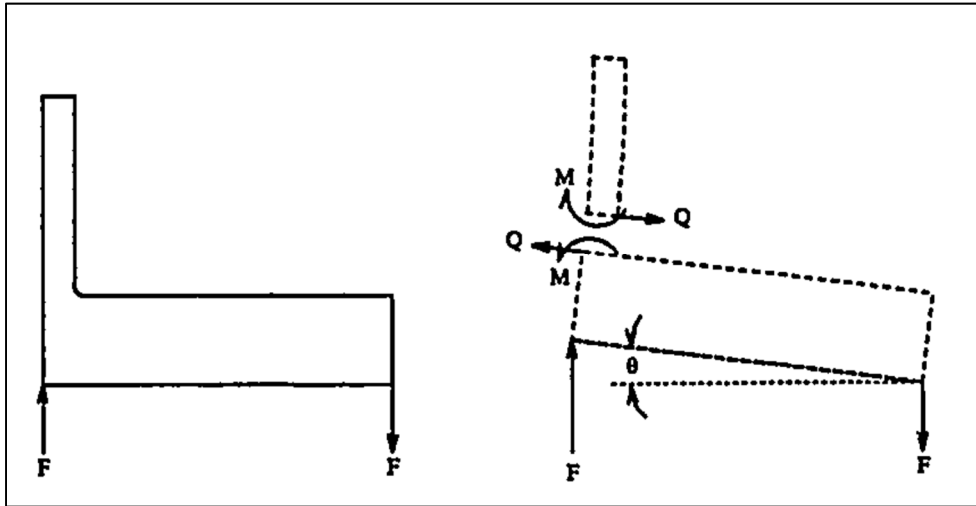
Figure 1-10 Pipe and ring used in analytical model (Sun, L. 1995)

1.5   Numerical Finite Element studies

Estrada et al. (1997) used a finite element method to validate analytical developed models. Also, it is used to study the leakage behavior and to validate the ASME code formulation for other gasket materials and joint configurations. The analysis was carried out using two and three-dimension axisymmetric finite elements with an orthotropic material model. To perform the analysis, they used a commercial finite element package (ABAQUS). In their analyses, they showed that axisymmetric modeling can be used to analyze critical designs however the analysis did not capture the stress concentration. Figures 1.10 and 1.11 show the three-dimensional and axisymmetric finite element models that were developed in this study.
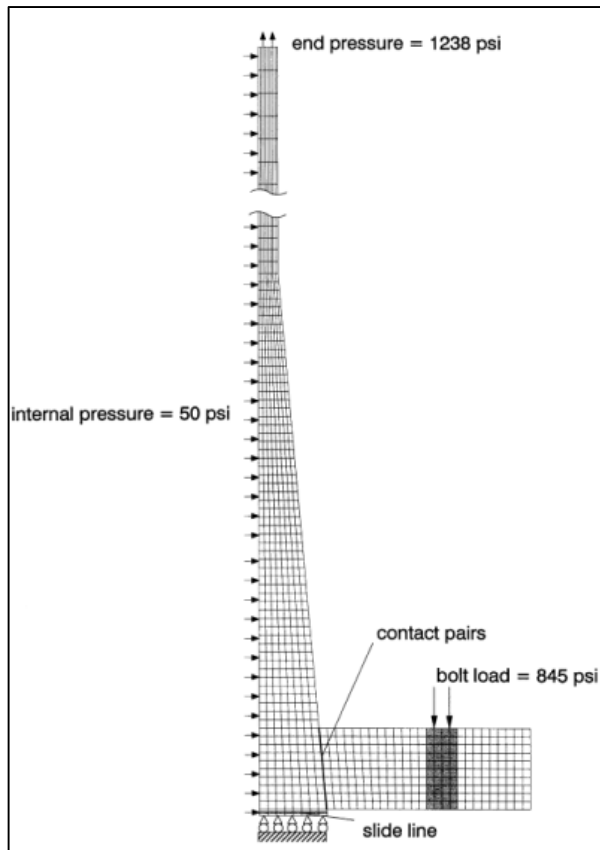
Figure 1-11 Axisymmetric finite element model (Estrada 1997)
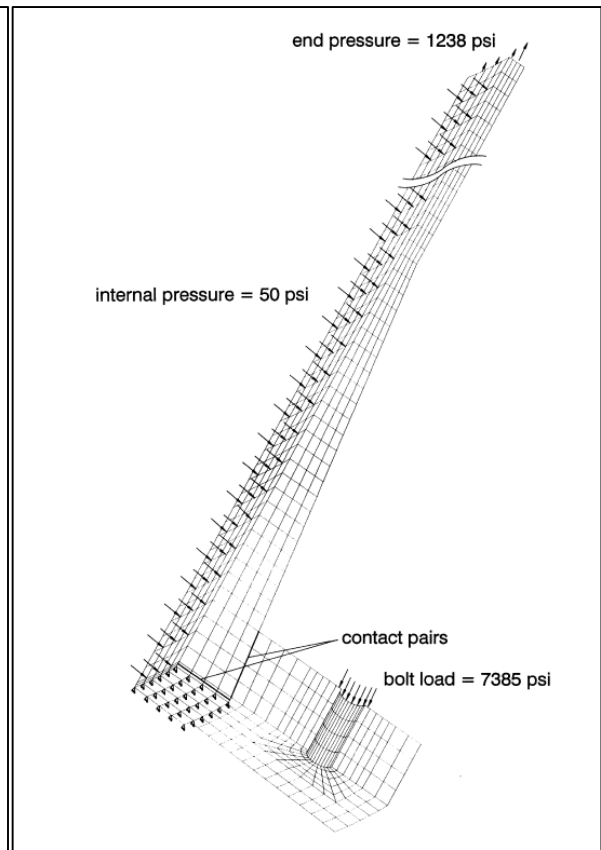
Figure 1-12 Three-dimensional finite element model (Estrada 1997)

Because of using the option that allowed pressure to penetrate the space where contact was lost, it was possible to measure more accurately the leakage in the axisymmetric case than in the three-dimensional case. Finally, they claimed that the results from finite element analysis were in an excellent agreement with the analytical results as shown in figure 1.13 and 1.14.
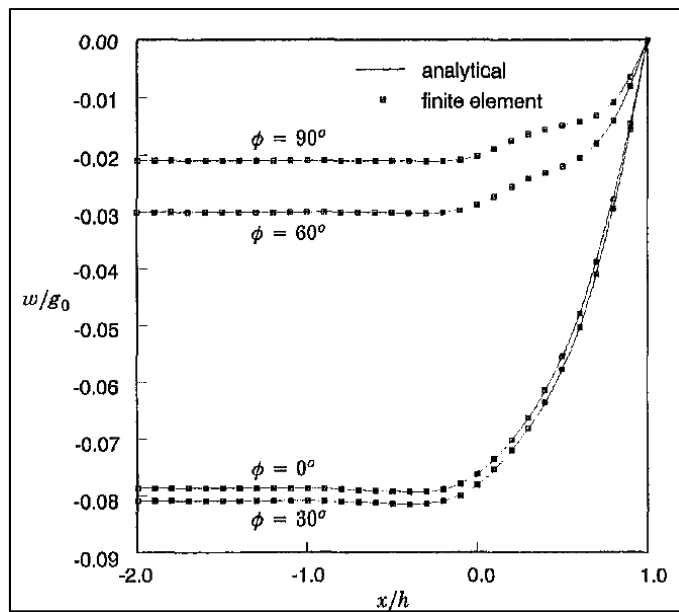
Figure 1-13 Distribution of radial displacement
(Estrada 1997)
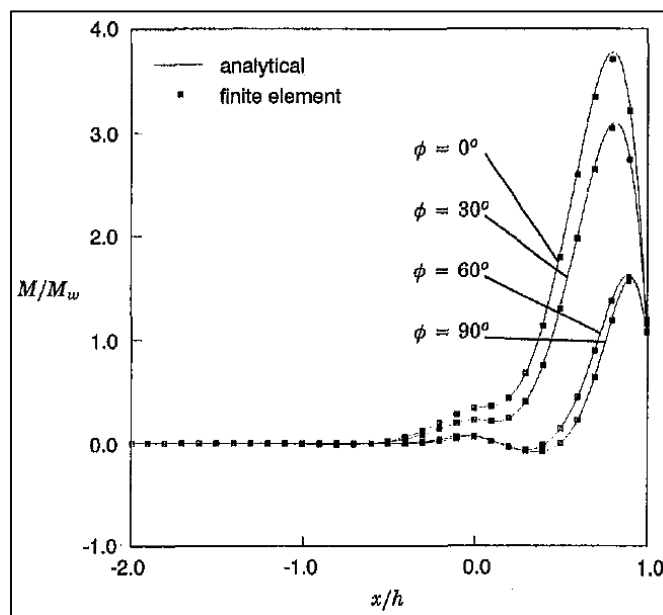
Figure 1-14 Distribution of axial moments (Estrada
1997)

Kurz and Roos (2012) conducted a simulation using the finite element method to investigate the stresses and strains of an FRP flange. They developed a linear-elastic finite element model for FRP bolted flange joints. In this study, the material behavior was assumed to be linear elastic with an isotropic Young's modulus of 11 GPa. According to this numerical study, the elastic equivalent stresses were shown for the initial tightening in a segment of the loose flange and the collar (figure 1.14). Under the washer, the material was compressed, resulting in a complex, multi-axial stress state. The FE model of a bolted flange connection with loose flanges and collars are depicted in figure 1.15.
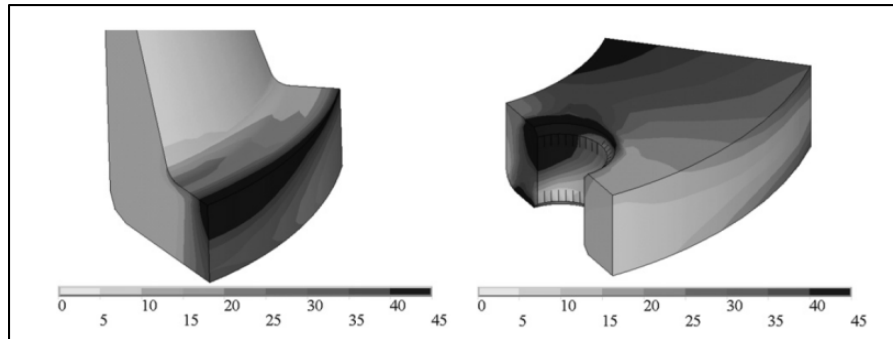
Figure 1-15 Results of the FE simulation (elastic equivalent stress) with highly loaded areas (dark) in the loose flange (left) and collar (right) (Kurz and Roos 2012)
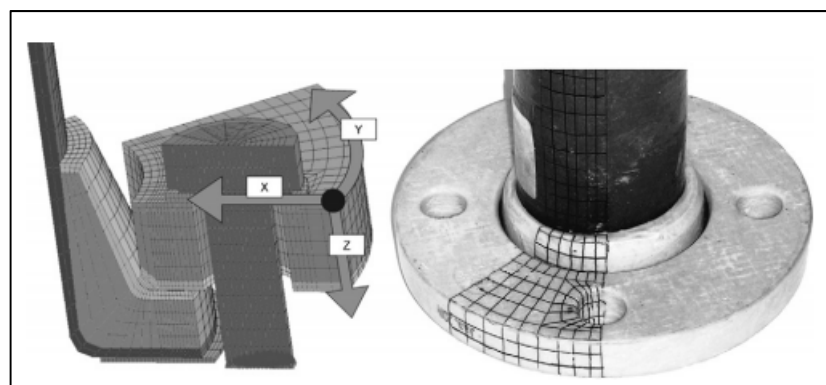
Figure 1-16 FE model of a bolted flange connection with loose flanges and collars (Kurz and Roos 2012)

Blach and Sun (1995) compared the analytical results, with the finite element results of an FRP flanged connection, using 3-D anisotropic layered solid elements. Figure 1.17 depicts 15-degree section of the flange in the FE model. With the ANSYS software, they modeled the composite flange as layered elements. In the FE model, axial symmetry is used to model a 15-degree section of the flange (Figure 1.16). They observed that the results from the finite element method are very close to those of an analytical method. However, issues were reused with many assumptions made in each calculation. They concluded that the two proposed methods are not reliable due to the lack of sufficient experimental verification.
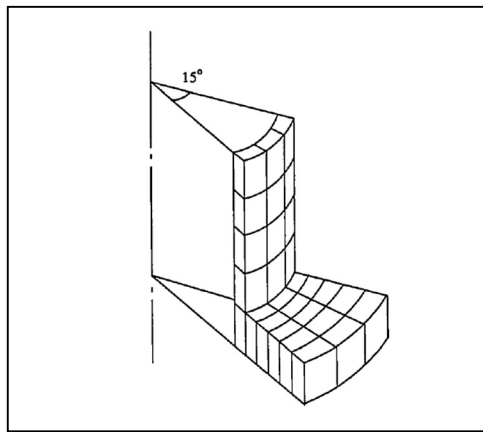
Figure 1-17 15-degree section of the
flange in FE model (Sun 1995)
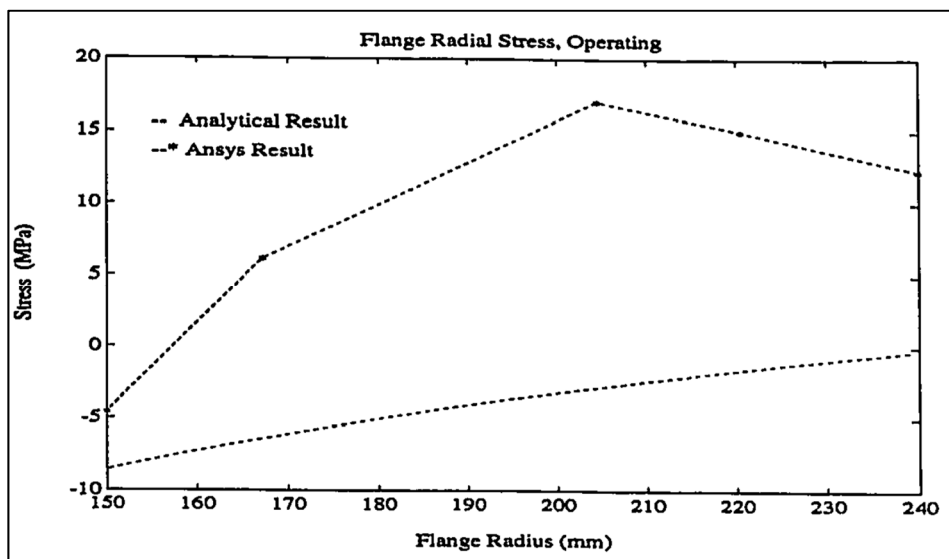
Figure 1-18 Flange front face radial stress, Operating (Sun 1995)
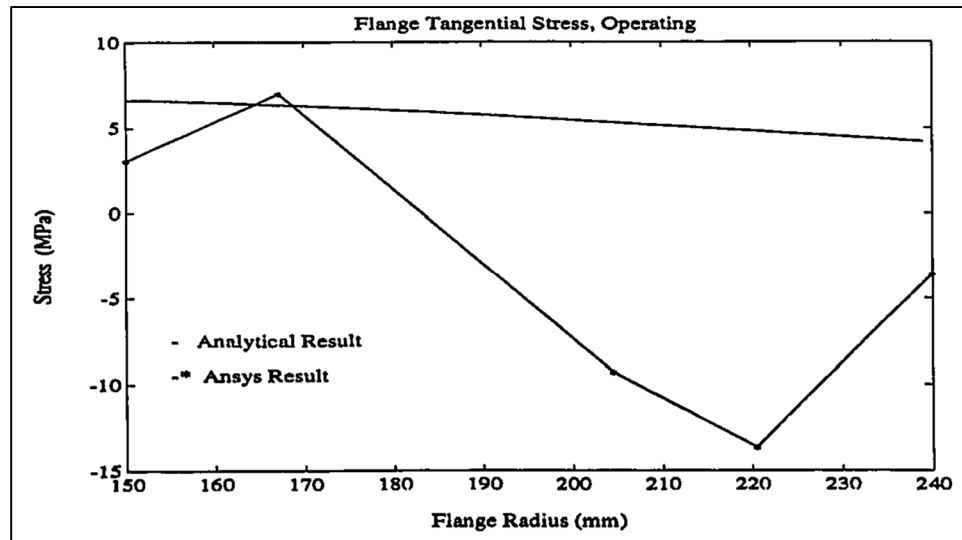
Figure 1-19 Flange back face tangential stress, Operating (Sun 1995)

1.6   Experimental studies

Kurz and Roos (2012) conducted an analytical and experimental evaluation of the mechanical behavior of floating type bolted flanged connections with glass reinforced plastic flanges. In order to analyze the deformation behavior due to creep-relaxation, they developed an instrumented test rig (Figure 1.19) which enabled the reproducing of the real behavior of an FRP bolted flanged joints. During the experimental investigation, the bolt force, the flange rotation, the strains at selected locations of the flange surface, the internal pressure and the temperature were monitored continuously. The test rig was completely vacuum-sealed to measure the leakage tightness of the bolted flange connection using helium mass spectrometry.

They also tested various gaskets made of rubber (EPDM) and PTFE of the bolted flange connection that was made of glass-fiber reinforced plastic flanges in compliance with DIN EN 13555. The results of an analytical design concept showed good agreement with the experiment results and the finite element simulation.
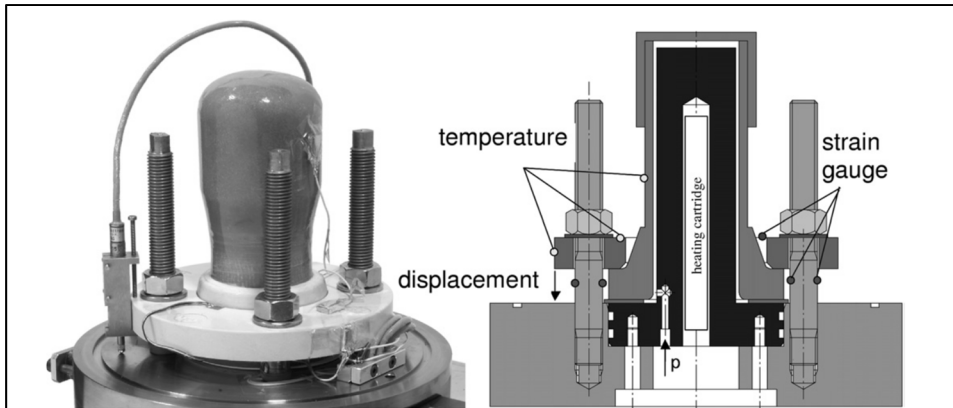
Figure 1-20 Test rig for experimental investigations on bolted flange
connections DN50 (without displacement transducers)
(Kurz and Roos 2012)

Following the design concept, the material reduction factors that lead to higher allowable
bolt forces, can be neglected and therefore that accompanied by increased tightness and
operational reliability of the plants.

Finally, they compared the displacements due to the rotation of the loose flange as
illustrated in figure 1.20 and showed an excellent agreement between all methods
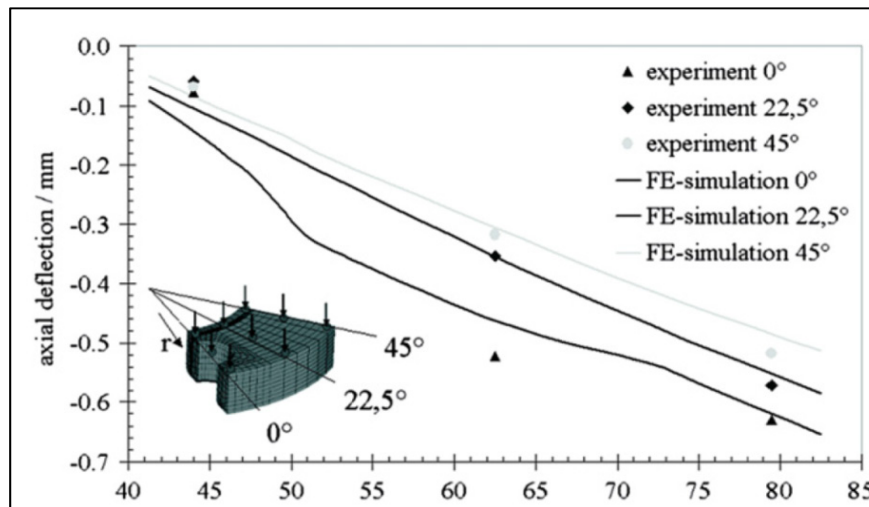
Figure 1-21 The displacements due to rotation of the loose flange
(Kurz and Roos 2012)
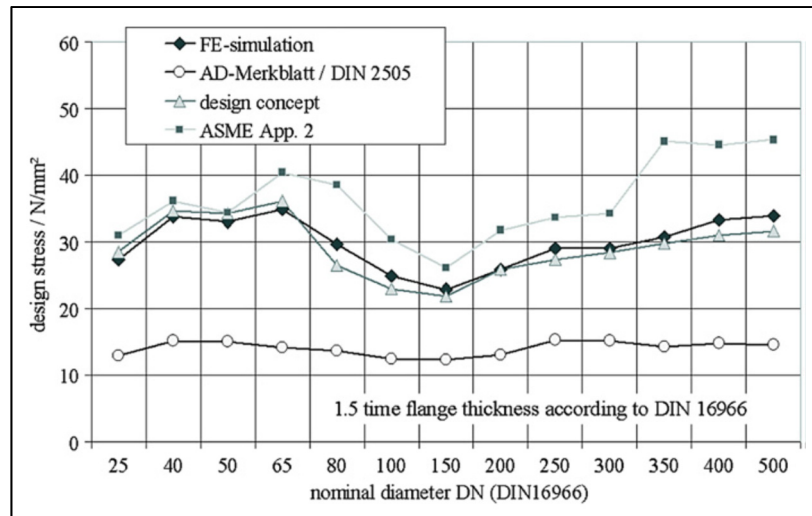
Figure 1-22 Comparison of nominal stresses from FE
simulation, AD-Merkblatt N1 (Kurz and Roos 2012)

Sun and Blach (1995) conducted an experimental investigation on FRP bolted flange joints with full-faced gasket. They attempted to demonstrate the effect of flange thickness on the mechanical properties of FRP flanges. Having different thicknesses at its ends, FRP flange was made of glass material and woven roving and was impregnated with the same resin. The polymer matrix is a vinyl ester. The vessel had a veil liner as a corrosive barrier. They used two kinds of 3 mm thick full-faced gasket. One was made of compressed asbestos and the other was made of synthetic rubber. The test parameters were:

Pressure (kPa) = 0, 138, 276, 414;

Bolt load (MPa) = 50, 100, 150;

Temperature = Room temperature.

They conducted several tests at both the bolt-up and operating conditions on a FRP flange joint.
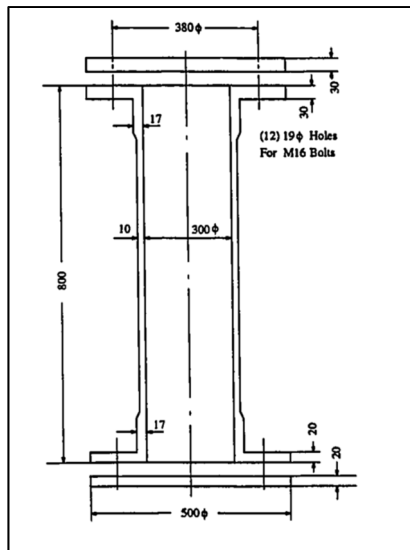
Figure 1-23 Dimensions of test
vessel (Sun 1995)
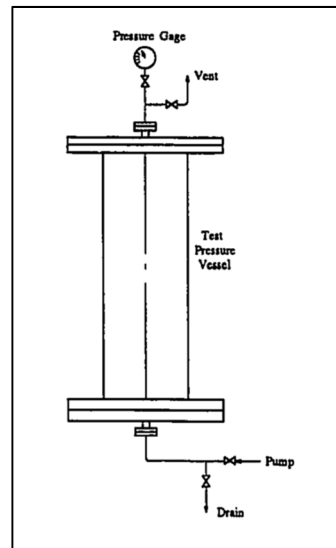
Figure 1-24 Test Set-Up
(Sun 1995)

In order to obtain a smaller flange width, they machined the flange after each test to reduce its outside diameter. They also discussed two analytical models for FRP flange based on Taylor Forge method but no quantitative comparisons were made. In addition, the authors proposed the use of finite element analysis for FRP flanges.

1.7   Conclusion

Over the last decades, a substantial research effort has been dedicated to the study of FRP bolted flange joints and characterization of composite flange behavior in different conditions. In general, a bolted flange joint is designed to connect pressure vessels and equipment without leakage (Nechache and Bouzid 2007). Sealing problems are encountered during operation of process equipment containing fluids when flanges are the convenient method of connection for reasons of fabrication, transportation, assembly, inspection, production and so on. In general, acceptable FRP bolted flange joint design must ensure that:

1   The stress levels in the flange joint are below the strength of the composite material.
2   The residual gasket load is sufficient to maintain the joint leak-tight.

The goals in bolted flanged joints are to keep a certain level of tightness and maintain reliability over a long period of time, especially at severe operating conditions such as elevated temperature and fluctuating pressure or when containing corrosive fluids.
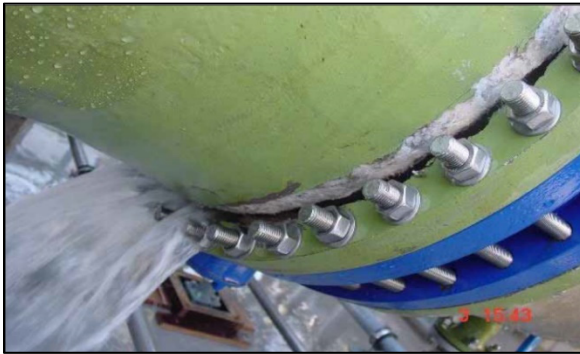
Figure 1-26 Crack at hub neck of the flange (Dynaflow 2011)

Figure 1-25 Crack in the flange face between the bolts and inside the bolt hole (Dynaflow 2011)

FRP materials are increasingly used by the industry because they provide strong resistance to chemical attack and have interesting mechanical properties. They have relatively long-life expectancy; cause less environmental concerns and offer low installation and maintenance costs. These qualities make FRP an attractive material for pressure vessels and piping components. The proper flange geometry should be designed to safely transfer the bolt loads to the gasket without overstressing the flange material. This problem should adequately be addressed to composite joints because of anisotropy behavior of composite materials which is depending on the materials from which FRP bolted flange joint is fabricated.

Although the analysis of metal flanges has made enormous progress, the analysis of composite bolted flange joints remains uncomplete and its progress has been slow especially in the analytical domain. It is intuitively recognized that there is a problem of standardization in the manufacturing progress of FRP flanges so that an analytical tool can help improve structural integrity and pressure rating. In addition, the complex behavior of composites requires more efforts made by the authors on the analysis of composite flanges.

Although a lot of emphases is put towards studying the material parameters and geometric involved, a complete comprehensive model is not in sight. For example, Sun's thesis (1995), which is focused on the behavior of FRP flanges by proposing an analytical and numerical study, but the results of the analytical part are not reliable due to some errors in his analytical model. In addition, the numerical part can be much better developed and accurate, since the available software allows handling of the problem better than two decades ago. According to the presented literature on FRP bolted flanged joints, it appears that most of the proposed analytical models are based on the metallic design. Any reliable flange design should encompass the anisotropic behavior of FRP materials to determine the load distribution in any part of the flange accurately.

1.8   Research project objectives

The state of the art presented shows that the amount of research and articles on FRP bolted flange joints based on the anisotropic behavior of the composite flange is rare. Particularly, the number of studies FRP bolted flange joint analytically, numerically and experimentally is very limited. Moreover, the design calculations of composite bolted flanged joints are not adequately covered in the literature. As mentioned earlier, the material properties used in the FRP flange design calculations in ASME BPV Code Section X are those used for steel and the calculations are totally based on those for metallic joints (Taylor Forge method). In their current form, the design calculation procedures based on metallic methodology are not adequate. Some adjustments are required to account for anisotropy, flexibility, rotational limits, bearing stresses of FRP flanges and etc. This study aims to investigate these issues and propose an integrated methodology to analyze theoretically, numerically and experimentally the stresses of FRP bolted flange joints subjected to the real operating condition of initial tightening and pressurization. Therefore, the main objective of this research work is:

- To develop an analytical solution to evaluate stresses and strains in FRP bolted flanged joints considering anisotropic material behavior for FRP flange without the hub.
    - o   Incorporate the hub in a new proposed analytical model to evaluate stresses and strains of FRP hubbed flanges.

- o Implement a flexibility analysis in the model to account for the elastic interaction between the different bolted joint components. The current design method considers the flange to be rigid and therefore the force in the bolt do not change with the application of pressure.
- o Develop different finite element models using the program ANSYS® Mechanical and ANSYS Composite PrepPost (ACP), for comparison with the analytical results and conduct validation of separate components (flange ring, hub, shell)
- o Conduct experimental testing to validate the analytical and numerical models and compare the parameters such as bolt load, flange rotation, stresses and strains at different locations.

CHAPTER 2

ANALYTICAL MODELING OF FRP BOLTED FLANGE JOINT

2.1   Introduction

In spite of the increased use of FRP composites in bolted flange joints and the good knowledge of these structures and their material behavior, the procedure used for their design is based on that of metallic flanges without any consideration of anisotropy. There is a major concern to appropriately address the anisotropic behavior of composite materials in a flange design. As indicated previously, it is necessary to make a precise evaluation of the load redistribution in order to be able to predict the structural integrity and leak tightness of FRP bolted flange joints.

This chapter concentrates mainly on the development of an analytical model for the fiber reinforced plastic bolted flanged joints derived from lamination theory for composite materials, taking into account the anisotropic behavior of FRP bolted flanged joints. In order to use the lamination theory in the analysis of FRP flanges especially flanges with the hub, it is necessary to derive some equations from the basic principles.

In general, composite flanges are subdivided into three major categories, namely: ring flange, hub, and cylinder. This chapter presents an analytical model to treat FRP bolted joints integrity and tightness based on anisotropy and flexibility analysis of all joint elements including the gasket, bolts and flanges and we describe the procedure for each part of the flange in detail.

The objective of this analytical study is to obtain the equations of the radial displacements and the rotations of the flange as well as the equations giving the radial, longitudinal and hoop stresses at the inside and outside surface of the flange.

2.2   Analytical model

FRP full-faced flanges with gasket having a prolonged surface from the inner edge up to the outer side of the flange, are usually characterized by rigid behavior. The wide surface of the joint requires high stress on the bolts so that this type of flange is mostly used in low pressure applications. In addition, in the full-faced flange joints soft gaskets which do not require a large clamping pressure to ensure tightness are used.

In developing the analytical model of FRP bolted flange joints, one of the objectives was that the model follows the ASME code design philosophy, bearing always in mind two important factors that are leakage tightness and structural integrity.

This part presents a theoretical approach based on a model that takes into account the flexibility of the gasket, bolts, and flanges as well as the elastic interaction between the different components of the assembly.

The analytical model of the bolted joint consists of two phases related to the operating conditions:

- Initial phase or phase i: in this first stage, the bolt-up of the flange is conducted resulting in the initial tightening of the flange. The tightening force compresses the two parts of the flange as well as the gasket and is characterized by a presumably uniform distribution of the contact pressure. Figure 2.1 (a) shows the flange in the initial phase.

- Final phase or phase f: As illustrated in figure 2.1 (b), a pressure is applied on the inside of the vessel or pipe and consequently the flange; The inside pressure also creates a hydrostatic end effect which is represented by an axial stress acting on the flat surfaces at the end of the cylindrical shell.

To simplify the analytical model of FRP bolted flange joint the following assumptions are made:

- The tightening torque during phase i is applied to the N bolts of the flange equally and simultaneously.

- The tightening force resulting from the force on the N bolts is considered to act on a circle of constant radius of the flange known as the bolt circle radius. This assumption makes it possible to consider the flange as an axisymmetric case that simplifies the analysis.

- A plane of symmetry is considered at the median plane of the joint as shown in figure 2.1 this simplifies the model to study one flange rather than the pair of flanges.
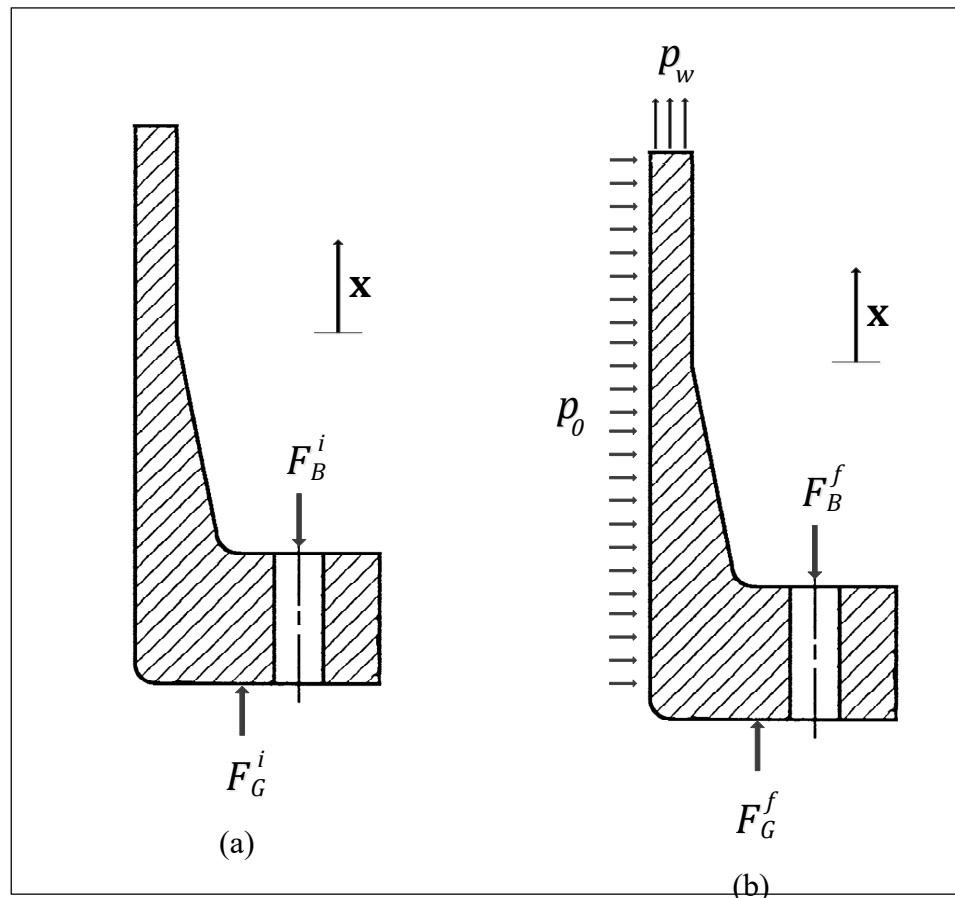
Figure 2-1 Cross-section of FRP flange in (a) initial tightening phase, (b) pressurization phase

2.3   Theoretical analysis for FRP bolted flange joints without the hub

In order to study FRP bolted flange joints analytically, first, we started to model FRP flange without the hub. FRP bolted flange joint is provided with a gasket that spreads on all its entire flat faces. For this type of flange with a full-face gasket, the centroid of a circular sector of unit width is considered to be the equilibrium pivot of the bolted joint. The model is thus considered symmetrical. The applied loads on each flange depend on the initial load on the bolts, the internal pressure and the reaction of the gasket.

Due to the pre-tightening of the bolts, the gasket is considered to be compressed uniformly in the circumferential direction and the flanges rotate slightly around the gasket reaction diameter. When applying pressure from inside, the two flanges tend to separate from each other and results in the unloading of the gasket as well as an additional increase in the rotation of the flanges. However, in reality, the rotation may appear in both radial and tangential directions depending on the bolt spacing and the applied pressure. It is worth noting that the behavior of such assembly under the operating conditions, depends on many parameters (Bouzid 1994).

This model consists of three essential mechanical elements, flange, bolts, and gasket. Each element is represented by simple elastic spring of linear stiffness kg, linear stiffness kb, and rotational stiffness kf for the gasket, bolts, and flange respectively. The solution of the flange is obtained from classical lamination theory. Basic knowledge of lamination theory for composite materials can be found in Ashton (1969) and R.M. Jones (1980).

In order to study FRP bolted flange joint analytically, a flange without the hub is divided into two distinct parts which are linked together through the edge loads to satisfy equilibrium. Figure 2.2 (a) shows the flange in phase i or bolt-up and figure 2.2 (b) shows the flange in phase f or pressurization. Point 1 in the figure is considered as the junction point between the ring and shell.
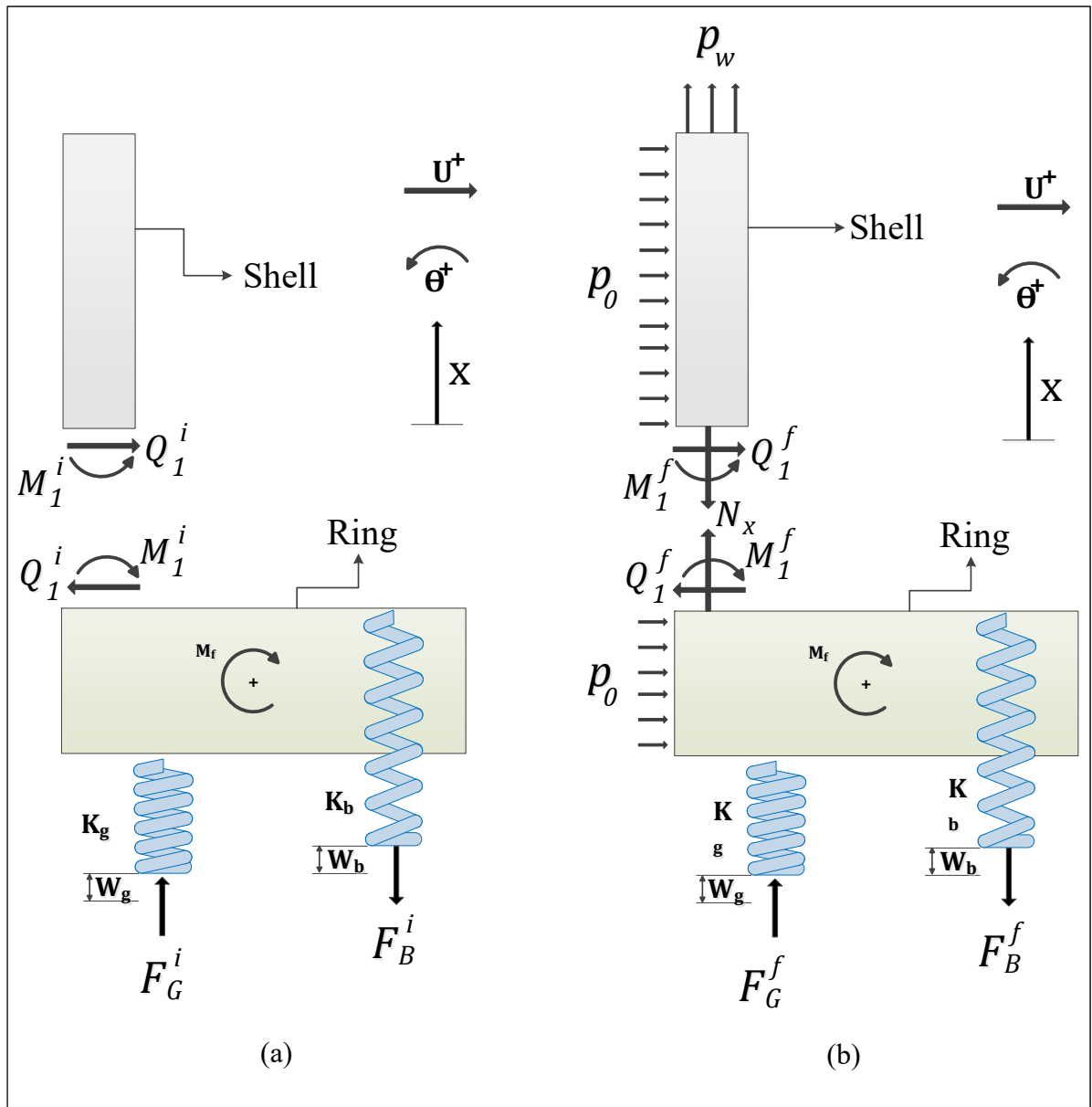
Figure 2-2 Analytical model of the FRP flange without the hub (a) bolt-up (b) pressurization

2.3.1   Analytical model of the shell (Cylinder theory)

The cylinder part of the FRP flange is modeled as an axisymmetric laminated shell which is subjected to internal pressure p_o and edge loads p_w. The shell is considered as a long cylinder of semi-infinite length i.e. the length is greater than π/b. The thin shell theory will apply for cases with a thickness-to-radius ratio less than or equal to 0.1. At the finite end, the shell is

subjected to the discontinuity shear force Q and edge moment M. The long thin cylinder equations for the displacements, rotation, bending moments, and shearing forces in terms of conditions at any locations x are given by the theory of beams on elastic foundation. The analytical models of the shell in two phases of bolt-up and pressurization are shown in figure 2.3.
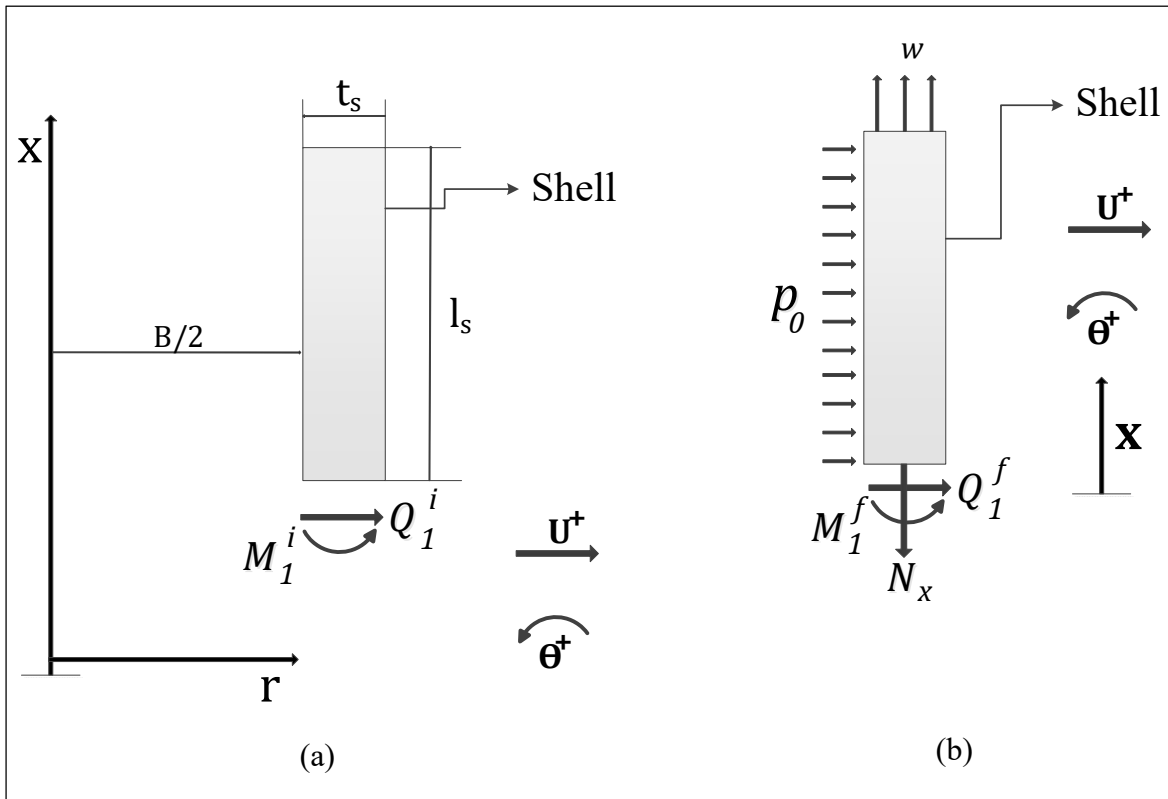
Figure 2-3 Aanalytical model of the shell (a) bolt-up and (b) pressurization

As illustrated in figure 2.3:

Q_1^i and Q_1^f are the shear forces at the junction of the ring and the shell;

M_1^i and M_1^f are the bending moment at the junction of the ring and the shell;

p_o is a pressure on the inside surface of the shell;

p_w is the effect of hydrostatic end pressure on the top surface of the shell;

N_x is the hydrostatic end force;

Due to the axial symmetry that applies to the shell and its loading forces, none of the variables depends on the angle θ. Consequently, all the partial derivatives with respect to θ in the equilibrium equations are equal to zero.

As shown in figure 2.4 the equilibrium equations for the shell in $x\theta$ coordinate system can be derived as:

$$N_x = cste \tag{2.1}$$

$$\frac{dN_{x\theta}}{dx} + \frac{1}{r}\frac{dM_{x\theta}}{dx} = 0 \tag{2.2}$$

$$\frac{d^2 M_x}{dx^2} - \frac{N_\theta}{r} = -p_o \tag{2.3}$$
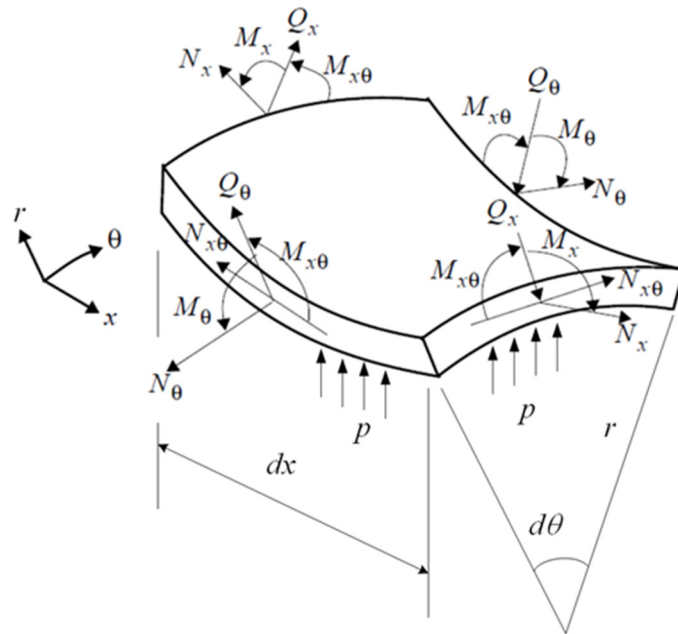
Figure 2-4 Shell element model

The relation between the forces and moments resultant and the strains in a thin laminate in xy coordinate system is:

$$\begin{Bmatrix} N_x \\ N_y \\ N_{xy} \\ M_x \\ M_y \\ M_{xy} \end{Bmatrix} = \begin{bmatrix} A_{s,11} & A_{s,12} & A_{s,16} & B_{s,11} & B_{s,12} & B_{s,16} \\ A_{s,12} & A_{s,22} & A_{s,26} & B_{s,12} & B_{s,22} & B_{s,26} \\ A_{s,16} & A_{s,26} & A_{s,66} & B_{s,16} & B_{s,26} & B_{s,66} \\ B_{s,11} & B_{s,12} & B_{s,16} & D_{s,11} & D_{s,12} & D_{s,16} \\ B_{s,12} & B_{s,22} & B_{s,26} & D_{s,12} & D_{s,22} & D_{s,26} \\ B_{s,16} & B_{s,26} & B_{s,66} & D_{s,16} & D_{s,26} & D_{s,66} \end{bmatrix} \begin{Bmatrix} \varepsilon_x^0 \\ \varepsilon_y^0 \\ \gamma_{xy}^0 \\ \kappa_x \\ \kappa_y \\ \kappa_{xy} \end{Bmatrix} \tag{2.4}$$

where: A_{ij}, B_i and D_{ij} are the stiffness coefficients and can be defined as follows:

$$A_{s,ij} = \sum_{k=1}^{N} (Q_{ij})_k (z_k - z_{k-1}) \tag{2.5}$$

$$B_{s,ij} = \frac{1}{2} \sum_{k=1}^{N} (Q_{ij})_k (z_k^2 - z_{k-1}^2) \tag{2.6}$$

$$D_{s,ij} = \frac{1}{3} \sum_{k=1}^{N} (Q_{ij})_k (z_k^3 - z_{k-1}^3) \tag{2.7}$$

According to the symmetrical laminate shell:

$A_{p,16} = A_{p,26} = 0$

$A_{s,16} = 0$

$A_{s,26} = 0$

$[B] = 0,$

The stress resultants are further related to shell displacement:

$$N_x = cste = A_{s,11} \frac{dw^0}{dx} - A_{s,12} \frac{u}{r} \tag{2.8}$$

$$N_\theta = A_{s,12} \frac{dw^0}{dx} - A_{s,22} \frac{u}{r} \tag{2.9}$$

$$M_x = -D_{s,11} \frac{d^2u}{dx^2} \tag{2.10}$$

$$M_\theta = -D_{s,12} \frac{d^2u}{dx^2} = -\frac{D_{s,12}}{D_{s,11}} M_r \tag{2.11}$$

$$M_{x\theta} = -\frac{D_{s,16}}{D_{s,11}} M_r \tag{2.12}$$

Combining Eqs. (2.8) and (2.9), it is possible to express N_θ as a function of:

$$N_\theta = \frac{u}{r}\left(A_{s,22} - \frac{A_{s,12}^2}{A_{s,11}}\right) + \frac{A_{s,12}}{A_{s,11}} N_x \tag{2.13}$$

From Eqs. (2.10) and (2.13) the following is obtained :

$$D_{s,11} \frac{d^4u}{dx^4} + \frac{u}{r^2}\left(A_{s,22} - \frac{A_{s,12}^2}{A_{s,11}}\right) + \frac{A_{s,12}}{A_{s,11}} \frac{N_x}{r} = p_o \tag{2.14}$$

The radial displacement of the shell after integration is given by:

$$u = C_1 e^{\beta_s x} \cos(\beta_s x) + C_2 e^{\beta_s x} \sin(\beta_s x) + C_3 e^{-\beta_s x} \cos(\beta_s x) + C_4 e^{-\beta_s x} \sin(\beta_s x) \tag{2.15}$$

where

$$\beta_s = \left[\frac{A_{s,22}A_{s,11} - A_{s,12}^2}{4r_s^2 D_{s,11}A_{s,11}}\right]^{1/4} \tag{2.16}$$

The general solution after simplification of Eq. (2.15) is:

$$u = e^{\beta_s x}[C_1 \cos(\beta_s x) + C_2 \sin(\beta_s x)] + e^{-\beta_s x}[C_3 \cos(\beta_s x) + C_4 \sin(\beta_s x)] \qquad (2.17)$$

The integral constants C_1, C_2, C_3 and C_4 will be determined from the boundary conditions. Since the cylinder is considered as a long and infinite shell, the displacement of the shell is zero when x tends to infinity.

$$\lim_{x \to +\infty} u = 0 \qquad (2.18)$$

And therefore:

$$\lim_{x \to +\infty} \frac{du}{dx} = \lim_{x \to +\infty} \theta = 0 \qquad (2.19)$$

This will result in:

$C_1 = 0$ and $C_2 = 0$.

Substituting C_1 and C_2 in the Eq. (2.17), we get:

$$u = e^{-\beta_s x}[C_3 \cos(\beta_s x) + C_4 \sin(\beta_s x)] \qquad (2.20)$$

The constants C_3 and C_4 are determined from the compatibility and boundary conditions:
At $x = 0$, then, $M = M_j^n$ and $Q = Q_j^n$.

Therefore, the displacement including the effect of pressure and rotation is given by:

$$u = \frac{1}{2\beta_s^3 D_{s,11}} e^{-\beta_s x}[Q_1^n \cos(\beta_s x) + \beta_s M_1^n (\cos(\beta_s x) - \sin(\beta_s x))] + \frac{A_{s,11} - \frac{1}{2} A_{s,12}}{4\beta_s^4 A_{s,11} D_{s,11}} p_o \qquad (2.21)$$

$$\psi = \frac{du}{dx} = \frac{1}{2\beta_s^2 D_{s,11}} e^{-\beta_s x} \left[Q_1^n \left(\cos(\beta_s x) - \sin(\beta_s x) \right) + 2\beta_s M_1^n \left(\cos(\beta_s x) \right) \right] \tag{2.22}$$

2.3.2 Analytical model of the flange ring (ring theory)

For the analytical analysis of FRP flanges, a number of theories were developed by Black (1994) and Sun (1995) but the theory based on the Kirchhoff-Love hypothesis can better characterize their behavior. In this theory, the transverse shear deformation is neglected and after deformation, the straight lines normal to the middle surface remain straight and undergo no thickness stretching.
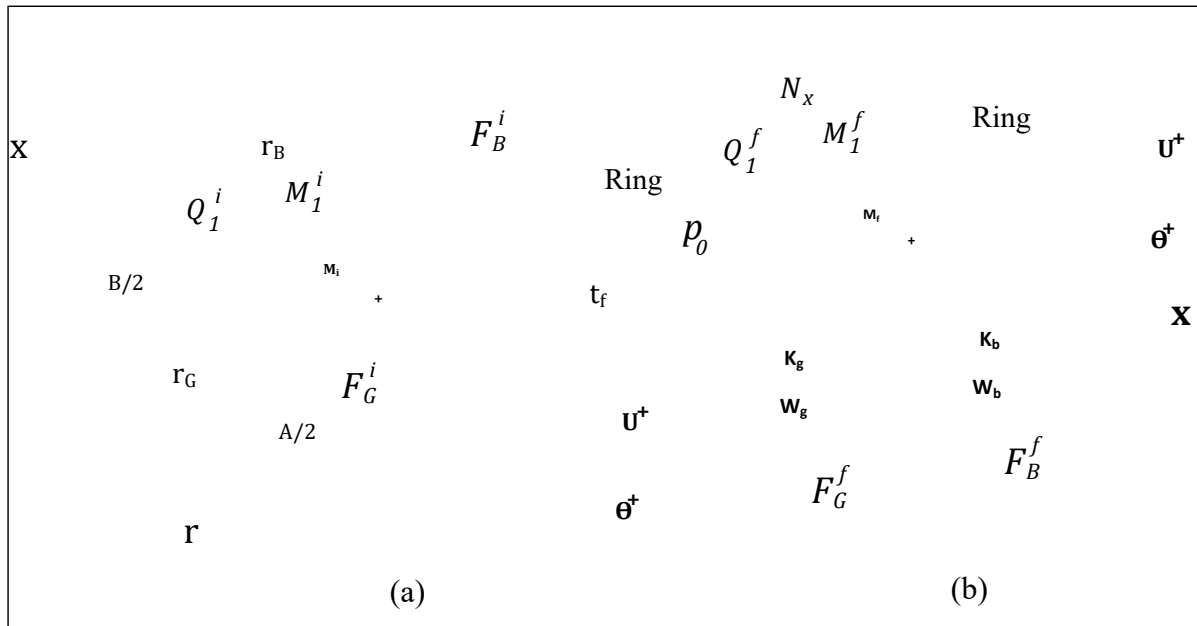
Figure 2-5 Analytical model of the ring (a) bolt-up and (b) pressurization

As shown in this figure:

F_B^i and F_B^f are the tightening force that applied through the bolts;

F_G^i and F_G^f are the forces resulting from compressing the gasket;

Q_1^i and Q_1^f are the shear forces at the junction of the ring and the shell;

M_1^i and M_1^f are the bending moment at the junction of the ring and the shell;

p_o is a pressure on the inside surface of the ring;

N_x is the membrane force due to hydrostatic end effect;

The ring part of the composite flange is considered to be a circular ring subjected to a moment in the tangential direction and ring loads in the radial and axial directions on its free inner edge and balanced by simple support on its outer edge. The analytical model of the ring subjected to bolt-up and pressurization is shown in Figure 2.5. The ring part of the composite flange is considered to be a circular ring subjected to a moment in the tangential direction and ring loads in the radial and axial directions on its free inner edge and balanced by simple support on its outer edge. Therefore, the theory of a thick-walled cylinder must be used to obtain the radial displacement of the ring.

According to the theory of thin plates, the transverse displacement w of the ring in the x-direction subjected to a concentrated force can be expressed as follows:

$$w(r) = \frac{Fr^2}{8\pi D_{p,11}}\left(\ln\left(\frac{r}{r_o}\right) - 1\right) - C_2 \ln\left(\frac{r}{r_o}\right) - \frac{C_1 r^2}{4} + C_3 \tag{2.23}$$

The rotation about a tangential axis of the ring is obtained from the derivation with respect to r of w:

$$\psi(r) = \frac{dw}{dr} = \frac{Fr}{8\pi D_{p,11}}\left(2\ln\left(\frac{r}{r_o}\right) - 1\right) - \frac{C_2}{r} - \frac{C_1 r}{2} \tag{2.24}$$

where F is the force applied to the ring. The constants C_1, C_2 and C_3 are determined from the following boundary conditions:

$$\text{at } r = r_i, \quad w = 0 \tag{2.25}$$

$$\text{at } r = r_i, \qquad M_r = M_1^n - \frac{t_f}{2} Q_1^n \qquad (2.26)$$

$$\text{at } r = r_o, \qquad M_r = 0 \qquad (2.27)$$

where n is equal to i for the bolt-up and f for the pressurization.

$$M_r = D_{p,11} \frac{d^2 w}{dr^2} + \frac{D_{p,12}}{r} \frac{dw}{dr} \qquad (2.28)$$

Then the constants are obtained as follows:

$$C_1 = -\frac{1}{4\pi D_{p,11}(r_o^2 - r_i^2)(D_{p,11} + D_{p,12})} \left[(D_{p,12} - D_{p,11})(r_o^2 - r_i^2)F + 2(D_{p,12} + \right.$$

$$\left. D_{p,11})r_i^2 \log\left(\frac{r_i}{r_o}\right) - 8\pi r_i^2 D_{p,11}\left(M_1^n - \frac{t_f}{2}Q_1^n\right) \right] \qquad (2.29)$$

$$C_2 = \frac{r_o^2 r_i^2}{4\pi D_{p,11}(r_o^2 - r_i^2)(D_{p,11} - D_{p,12})} \left[4\pi D_{p,11}\left(M_1^n - \frac{t_f}{2}Q_1^n\right) - (D_{p,12} + D_{p,11})\log\left(\frac{r_i}{r_o}\right)F \right] \qquad (2.30)$$

$$C_3 = \frac{-r_i^2}{16\pi D_{p,11}(r_o^2 - r_i^2)(D_{p,11}^2 - D_{p,12}^2)} \left[(D_{p,12}^2 - 3D_{p,11}^2 + 2D_{p,12}D_{p,11})(r_o^2 - r_i^2)F - 8\pi r_i^2(D_{p,11}^2 - \right.$$

$$D_{p,12}D_{p,11})\left(M_1^n - \frac{t_f}{2}Q_1^n\right) - 2r_o^2(D_{p,12}^2 - D_{p,11}^2)\log\left(\frac{r_i}{r_o}\right)F - 4r_o^2(D_{p,12}^2 + D_{p,11}^2 + $$

$$\left. 2D_{p,12}D_{p,11})\log^2\left(\frac{r_i}{r_o}\right)F - 16\pi r_o^2(D_{p,11}^2 - D_{p,12}D_{p,11})\log\left(\frac{r_i}{r_o}\right)\left(M_1^n - \frac{t_f}{2}Q_1^n\right) \right] \qquad (2.31)$$

Therefore, substituting for the constant C's Eq. (2.24) becomes:

$$\psi(r) = \frac{dw}{dr} = \frac{rF}{8\pi D_{p,11}}\left(2\log\left(\frac{r}{r_o}\right) - 1\right) + \frac{r}{8\pi D_{p,11}(r_o^2 - r_i^2)(D_{p,11} + D_{p,12})}\left((r_o^2 - r_i^2)(D_{p,12} - \right.$$

$$\left. D_{p,11})F + 2r_i^2(D_{p,12} + D_{p,11})\log\left(\frac{r_i}{r_o}\right)F - 8\pi r_i^2 D_{p,11}\left(M_1^n - \frac{t_f}{2}Q_1^n\right)\right) +$$

$$\frac{r_o^2 r_i^2}{4\pi r D_{p,11}(r_o^2 - r_i^2)(D_{p,11} - D_{p,12})}\left((D_{p,12} + D_{p,11})\log\left(\frac{r_i}{r_o}\right)F - 4\pi D_{p,11}\left(M_1^n - \frac{t_f}{2}Q_1^n\right)\right) \qquad (2.32)$$

In order to obtain the displacement of the flange ring u in the radial direction, the theory of thick-walled cylinder subjected to radial pressure is used. The displacement of the ring in different directions (r, Θ, and x) according to the classical theory of axisymmetric bending plate are given as follows:

$$u^f(r,x) = u_0^f(r) + x\psi(r) \tag{2.33}$$

$$v^f(r,x) = 0 \tag{2.34}$$

$$w^f(r,x) = w_0^f(r) \tag{2.35}$$

where u^f, v^f and w^f are the ring displacement in the r, θ and x respectively. The subscript 0 refers to the midplane displacement of the ring.

The strain-displacement relationships in a cylindrical coordinate are as follows:

$$\varepsilon_r = \frac{\partial u}{\partial r} \tag{2.36}$$

$$\varepsilon_\theta = \frac{1}{r}\frac{\partial v}{\partial \theta} + \frac{u}{r} \tag{2.37}$$

$$\varepsilon_x = \frac{\partial w}{\partial x} \tag{2.38}$$

$$\varepsilon_{rx} = \frac{1}{2}\left(\frac{\partial u}{\partial x} + \frac{\partial w}{\partial r}\right) \tag{2.39}$$

$$\varepsilon_{\theta x} = \frac{1}{2}\left(\frac{\partial v}{\partial x} + \frac{1}{r}\frac{\partial w}{\partial \theta}\right) \tag{2.40}$$

$$\varepsilon_{r\theta} = \frac{1}{2}\left(\frac{1}{r}\frac{\partial u}{\partial \theta} + \frac{\partial v}{\partial r} - \frac{v}{r}\right) \tag{2.41}$$

The definition of the linear strain tensor is:

$$\varepsilon_{ij} = \frac{1}{2}\left(u_{i,j} + u_{j,i}\right) \tag{2.42}$$

According to the strain-displacement relation in a cylindrical coordinate system, the strains for these deformations are:

$$\varepsilon_r = \frac{du_0^f}{dr} + x\frac{d\psi}{dr} \tag{2.43}$$

$$\varepsilon_\theta = \frac{u_0^f}{r} + x\frac{\psi}{r} \tag{2.44}$$

$$\varepsilon_x = 0 \tag{2.45}$$

$$\varepsilon_{rx} = \frac{1}{2}\left(\psi + \frac{dw_0^f}{dr}\right) \tag{2.46}$$

$$\varepsilon_{\theta x} = 0 \tag{2.47}$$

$$\varepsilon_{r\theta} = 0 \tag{2.48}$$

The principle of minimum total energy is used, in order to derive the governing equilibrium equations of the classic laminate plate theory. The strain energy for the circular plate is obtained from:

$$U = \frac{1}{2}\int_0^{2\pi}\int_{r_i}^{r_0}\int_{-\frac{t}{2}}^{\frac{t}{2}}(\sigma_r\varepsilon_r + \sigma_\theta\varepsilon_\theta + \sigma_x\varepsilon_x + 2\sigma_{r\theta}\varepsilon_{r\theta} + 2\sigma_{rx}\varepsilon_{rx} + 2\sigma_{\theta x}\varepsilon_{\theta x})dx\,rdr\,d\theta \tag{2.49}$$

By integrating the above equation in respect to θ and considering only non-zero terms of this equation, the strain energy within the plate becomes:

$$U = \pi\int_{r_i}^{r_0}\left[\frac{du_0^f}{dr}\int_{-\frac{t}{2}}^{\frac{t}{2}}\sigma_r dx + \frac{d\psi}{dr}\int_{-\frac{t}{2}}^{\frac{t}{2}}\sigma_x x dx + \frac{u_0^f}{r}\int_{-\frac{t}{2}}^{\frac{t}{2}}\sigma_\theta dx + \frac{\psi}{r}\int_{-\frac{t}{2}}^{\frac{t}{2}}\sigma_\theta x dx + \psi\int_{-\frac{t}{2}}^{\frac{t}{2}}\sigma_{rx} dx + \right.$$
$$\left.\frac{dw_0^f}{dr}\int_{-\frac{t}{2}}^{\frac{t}{2}}\sigma_{rx} dx\right]rdr \tag{2.50}$$

Then, the in-plane force resultants are obtained:

$$N_r = \int_{-\frac{t}{2}}^{\frac{t}{2}} \sigma_r \, dx \tag{2.51}$$

$$N_\theta = \int_{-\frac{t}{2}}^{\frac{t}{2}} \sigma_\theta \, dx \tag{2.52}$$

The shear forces are:

$$Q_{rx} = \int_{-\frac{t}{2}}^{\frac{t}{2}} \sigma_{rx} \, dx \tag{2.53}$$

And the moments are:

$$M_r = \int_{-\frac{t}{2}}^{\frac{t}{2}} \sigma_r x \, dx \tag{2.54}$$

$$M_\theta = \int_{-\frac{t}{2}}^{\frac{t}{2}} \sigma_\theta x \, dx \tag{2.55}$$

By substituting for the stresses in Eq. (2.50), the strain energy in terms of loads is obtained:

$$U = \pi \int_{r_i}^{r_0} u_0^f \left(\frac{d}{dr} N_r r + N_\theta \right) dr + \pi \int_{r_i}^{r_0} \psi \left(\frac{d}{dr} M_r r + M_\theta \right) dr + \pi \int_{r_i}^{r_0} \psi Q_{rx} r dr +$$

$$\pi \int_{r_i}^{r_0} \frac{d}{dr} w_0^f Q_{rx} r dr \tag{2.56}$$

The work done on the ring by the different loads is given as:

$$V = (p_o t 2\pi r_i) u_A^f + (F_G 2\pi r_G) w_G^f + (-F_B 2\pi r_B) w_B^f + (-M_A 2\pi r_i) \psi_A^f \tag{2.57}$$

The work-energy theorem states that the net work done by the forces is equal to the change in its kinetic energy or the energy stored in the form of deformation in the system. Therefore:

$$U = V \tag{2.58}$$

This may be written as:

$$\pi \int_{r_i}^{r_0} u_0^f \left(\frac{d}{dr}N_r r + N_\theta\right) dr + \pi \int_{r_i}^{r_0} \psi \left(\frac{d}{dr}M_r r + M_\theta\right) dr + \pi \int_{r_i}^{r_0} \psi Q_{rx} r dr +$$

$$\pi \int_{r_i}^{r_0} \frac{d}{dr} w_0^f Q_{rx} r dr = (p_o t \pi r_i) \times u_A^f + (F_G 2\pi r_G) \times w_G^f + (-F_B 2\pi r_B) \times w_B^f + (-M_A \pi r_i) \times$$

$$\psi_A^f \tag{2.59}$$

The equations of equilibrium are then obtained:

$$\delta u_0^f \; : \; N_\theta - \frac{d(rN_r)}{dr} = 0 \tag{2.60}$$

$$\delta \psi \; : \; M_\theta + rQ_{rx} - \frac{d}{dr}(rM_r) = 0 \tag{2.61}$$

$$\delta w_0^f \; : \; \frac{d}{dr}(rQ_{rx}) = 0 \tag{2.62}$$

With the following boundary conditions:

At $r = r_i$:

$$rN_r = r_i(-p_o t + Q) \tag{2.63}$$

$$rM_r = r_i\left(M + \frac{Qt}{2}\right) \tag{2.64}$$

$$rQ_{rx} = -r_i F \tag{2.65}$$

At $r = r_0$:

$$N_r = 0 \tag{2.66}$$

$$M_r = 0 \tag{2.67}$$

$$w_0^f = 0 \tag{2.68}$$

By considering Hooke's law, we get:

$$\varepsilon_r = \frac{1}{E_r}(\sigma_r - \upsilon_r\sigma_\theta) \tag{2.69}$$

$$\varepsilon_\theta = \frac{1}{E_\theta}(\sigma_\theta - \upsilon_\theta\sigma_r) \tag{2.70}$$

$$\varepsilon_{rx} = \frac{1}{2G_{rx}}\sigma_{rx} \tag{2.71}$$

where E_r and E_θ are Young's modulus in the radial and tangential directions; υ_r and υ_θ are the Poisson coefficients $(E_r\upsilon_\theta = E_\theta\upsilon_r)$; G_{rx} is the shear modulus in the plane r-x.

There as the stresses are obtained by:

$$\sigma_r = Q_{rr}\varepsilon_r + Q_{r\theta}\varepsilon_\theta \tag{2.72}$$

$$\sigma_\theta = Q_{r\theta}\varepsilon_r + Q_{\theta\theta}\varepsilon_\theta \tag{2.73}$$

$$\sigma_{rx} = Q_{rx}\varepsilon_{rx} \tag{2.74}$$

where the elastic coefficients Q's are:

$$Q_{rr} = \frac{E_r}{1-\upsilon_r\upsilon_\theta} \tag{2.75}$$

$$Q_{r\theta} = \frac{E_r\upsilon_\theta}{1-\upsilon_r\upsilon_\theta} \tag{2.76}$$

$$Q_{\theta\theta} = \frac{E_\theta}{1-\upsilon_r\upsilon_\theta} \tag{2.77}$$

$$Q_{rx} = 2G_{rx} \tag{2.78}$$

Therefore, the plate forces and moments of Eqs. (2.51) to (2.55) can be expressed in terms of displacement and rotation:

$$N_r = \int_{-\frac{t}{2}}^{\frac{t}{2}} \left[Q_{rr} \left(\frac{du_0^f}{dr} + x \frac{d\psi}{dr} \right) + Q_{r\theta} \left(\frac{u_0^f}{r} + x \frac{\psi}{r} \right) \right] dx \tag{2.79}$$

$$N_\theta = \int_{-\frac{t}{2}}^{\frac{t}{2}} \left[Q_{r\theta} \left(\frac{du_0^f}{dr} + x \frac{d\psi}{dr} \right) + Q_{\theta\theta} \left(\frac{u_0^f}{r} + x \frac{\psi}{r} \right) \right] dx \tag{2.80}$$

$$M_r = \int_{-\frac{t}{2}}^{\frac{t}{2}} \left[Q_{rr} \left(\frac{du_0^f}{dr} + x \frac{d\psi}{dr} \right) + Q_{r\theta} \left(\frac{u_0^f}{r} + x \frac{\psi}{r} \right) \right] x\, dx \tag{2.81}$$

$$M_\theta = \int_{-\frac{t}{2}}^{\frac{t}{2}} \left[Q_{r\theta} \left(\frac{du_0^f}{dr} + x \frac{d\psi}{dr} \right) + Q_{\theta\theta} \left(\frac{u_0^f}{r} + x \frac{\psi}{r} \right) \right] x\, dx \tag{2.82}$$

$$Q_{rx} = \int_{-\frac{t}{2}}^{\frac{t}{2}} \left[\frac{Q_{rx}}{2} \left(\psi + \frac{dw_0^f}{dr} \right) \right] dx \tag{2.83}$$

Then, these equations can be simplified to:

$$N_r = \frac{du_0^f}{dr} A_{p,11} + \frac{d\psi}{dr} B_{p,11} + \frac{u_0^f}{r} A_{p,12} + \frac{\psi}{r} B_{p,12} \tag{2.84}$$

$$N_\theta = \frac{du_0^f}{dr} A_{p,12} + \frac{d\psi}{dr} B_{p,12} + \frac{u_0^f}{r} A_{p,22} + \frac{\psi}{r} B_{p,22} \tag{2.85}$$

$$M_r = \frac{du_0^f}{dr} B_{p,11} + \frac{d\psi}{dr} D_{p,11} + \frac{u_0^f}{r} B_{p,12} + \frac{\psi}{r} D_{p,12} \tag{2.86}$$

$$M_\theta = \frac{du_0^f}{dr} B_{p,12} + \frac{d\psi}{dr} D_{p,12} + \frac{u_0^f}{r} B_{p,22} + \frac{\psi}{r} D_{p,22} \tag{2.87}$$

$$Q_{rx} = \frac{1}{2} \left(\psi + \frac{dw_0^f}{dr} \right) A_{p,16} \tag{2.88}$$

where the stiffness coefficients for the ring are:

$$\left(A_{p,11}, A_{p,12}, A_{p,22} \right) = \int_{-\frac{t}{2}}^{\frac{t}{2}} (Q_{rr}, Q_{r\theta}, Q_{\theta\theta}) dx \tag{2.89}$$

$$\left(B_{p,11}, B_{p,12}, B_{p,22} \right) = \int_{-\frac{t}{2}}^{\frac{t}{2}} (Q_{rr}, Q_{r\theta}, Q_{\theta\theta}) x\, dx \tag{2.90}$$

$$\left(D_{p,11}, D_{p,12}, D_{p,22}\right) = \int_{-\frac{t}{2}}^{\frac{t}{2}} (Q_{rr}, Q_{r\theta}, Q_{\theta\theta})x^2 dx \tag{2.91}$$

$$A_{p,16} = \int_{-\frac{t}{2}}^{\frac{t}{2}} (Q_{rx}) dx \tag{2.92}$$

When the material properties are symmetrical with respect to the plate mid-plane then:

$$B_{p,11} = B_{p,12} = B_{p,22} = 0 \tag{2.93}$$

The forces and moments (2.84) to (2.88) can be simplified to:

$$N_r = \frac{du_0^f}{dr} A_{rr} + \frac{u_0^f}{r} A_{r\theta} \tag{2.94}$$

$$N_\theta = \frac{du_0^f}{dr} A_{p,11} + \frac{u_0^f}{r} A_{p,12} \tag{2.95}$$

$$M_r = \frac{d\psi}{dr} D_{p,12} + \frac{\psi}{r} D_{p,12} \tag{2.96}$$

$$M_\theta = \frac{d\psi}{dr} D_{p,12} + \frac{\psi}{r} D_{p,11} \tag{2.97}$$

$$Q_{rx} = \frac{1}{2}\left(\psi + \frac{dw_0^f}{dr}\right) A_{p,16} \tag{2.98}$$

Now, the equilibrium Eqs. (2.60), (2.61) and (2.62) can be rearranged as follows:

$$\delta u_0^f : \quad r^2 \frac{d^2 u_0^f}{dr^2} + r \frac{du_0^f}{dr} - \frac{A_{p,22}}{A_{p,11}} u_0^f = 0 \tag{2.99}$$

With the following boundary condition:

$$\text{At } r = r_i, \quad rQ_{rx} = -r_i F \tag{2.100}$$

Then

$$r\frac{d^2\Psi}{dr^2} + \frac{d\Psi}{dr} - \frac{D_{p,22}\Psi}{D_{p,11}r} = -\frac{r_iF}{D_{p,11}} \tag{2.101}$$

Hence, equation (2.99) becomes:

$$u_0^f = \frac{(p_ot-Q)(r_0)^{m_2-1}}{4(A_{p,12}+\sqrt{A_{p,22}A_{p,11}})\Delta}r^{m_1} + \frac{(-p_ot+Q)(r_0)^{m_1-1}}{4(A_{p,12}-\sqrt{A_{p,22}A_{p,11}})\Delta}r^{m_2} \tag{2.102}$$

where:

$$m_1 = \sqrt{\frac{A_{p,22}}{A_{p,11}}}$$

$$m_2 = -m_1$$

$$\Delta = (2r_o)^{m_1-1}(2r_i)^{m_2-1} - (2r_o)^{m_2-1}(2r_i)^{m_1-1} \tag{2.103}$$

In the case of equivalent elastic properties of the ring in the radial and tangential directions, we get:

$$A_{p,22} = A_{p,11}$$

$$m_1 = -m_2 = 1$$

$$\Delta = \frac{r_o^2 - r_i^2}{2r_o^2 \, r_i^2}$$

Therefore, the radial displacement of the ring is given by:

$$u_0^f(r) = \frac{(p_ot-Q)r_i^2}{(A_{p,12}+A_{p,11})(r_o^2-r_i^2)} \times r + \frac{(-p_ot+Q)r_o^2r_i^2}{4(A_{p,12}-A_{p,11})(r_o^2-r_i^2)} \times \frac{1}{r} \tag{2.104}$$

2.4   Theoretical analysis of FRP bolted flange joints with the hub

The analytical model of FRP bolted flange joint with the hub is illustrated in figure 2.6. In order to study FRP flange bolted flange joint analytically, a flange with the hub is divided into three distinct parts which are connected to one another. Figure 2.6 (a) shows the flange in phase n=i or bolt-up and figure 2.6 (b) shows the flange in phase n=f or pressurization. Point 1 in the figure is considered as the junction point between the ring and the shell and point 2 is considered as the junction point between hub and shell. It is important to note that the analytical approach for the ring and the shell of the FRP flange with the hub is the same as the model elaborated in section 2.3. Therefore, in this part, the analytical model of only the hub is developed and elaborated in detail based on the beam on elastic foundation theory applied to short thin cylinders. Nevertheless, for reiteration, the theories used for the shell and ring are the theory of the beams on an elastic foundation for long cylinders and the theory of thin plate under bending respectively.

As mentioned earlier, For FRP flanges with a full-face gasket the centroid of a circular sector of the unit width is considered to in equilibrium in all directions. To simplify the analysis considerably, the thickness of the hub is assumed to be small compared to the radius, then the mid-surface line of the hub remains almost parallel to that for the shell. It is also fair to assume that the model is considered symmetrical. It is intuitively recognized that the applied loads on each flange depend on the initial load on the bolts, the internal pressure and the reaction of the gasket.

2.4.1   Analytical model of the hub

The analytical model of the hub can be simplified by a thin cylinder subjected to an axisymmetric loading. Figure 2.7 depicts the analytical model of the hub at bolt-up and pressurization.
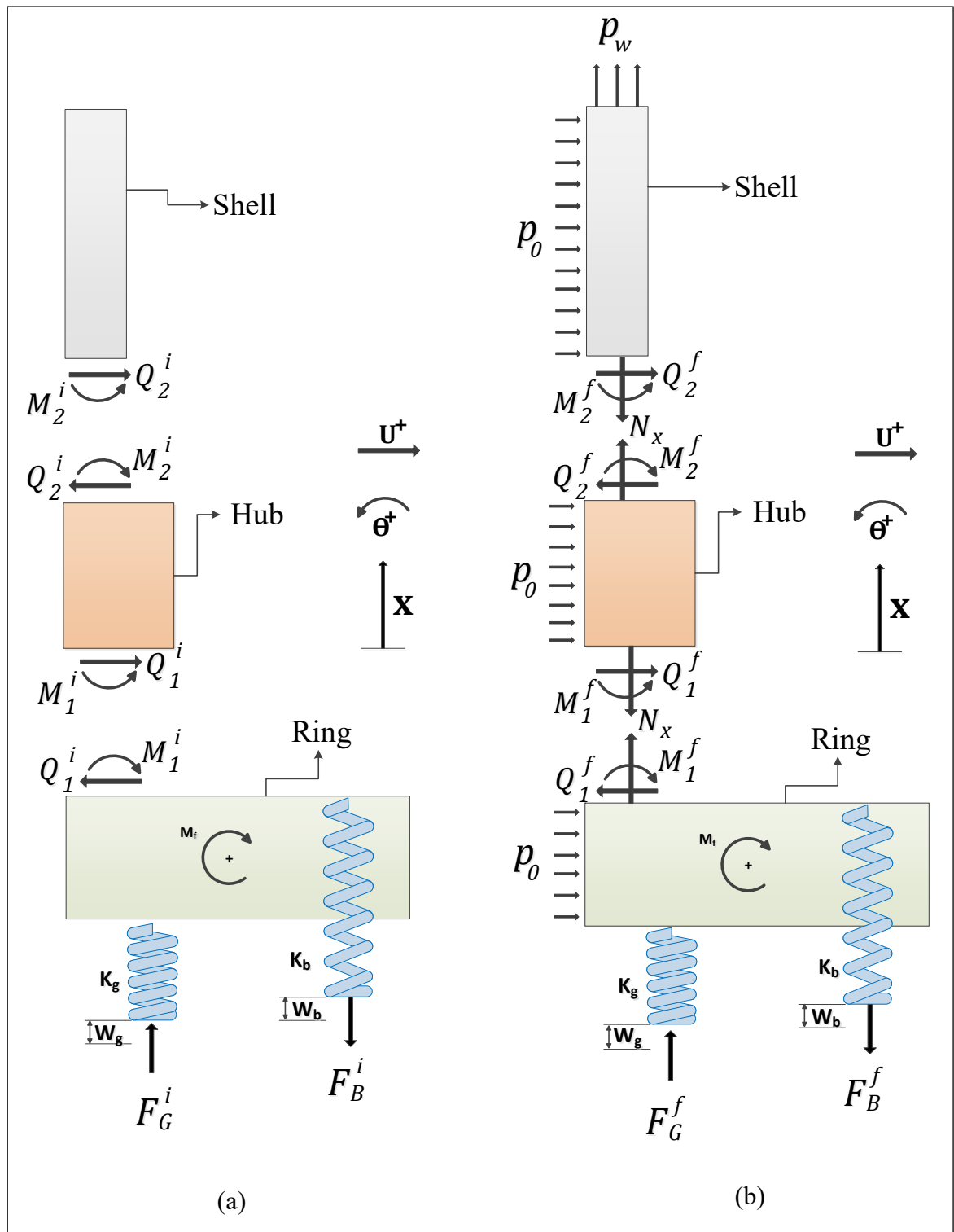
Figure 2-6 Analytical model for the FRP flange with the hub (a) bolt-up (b) pressurization
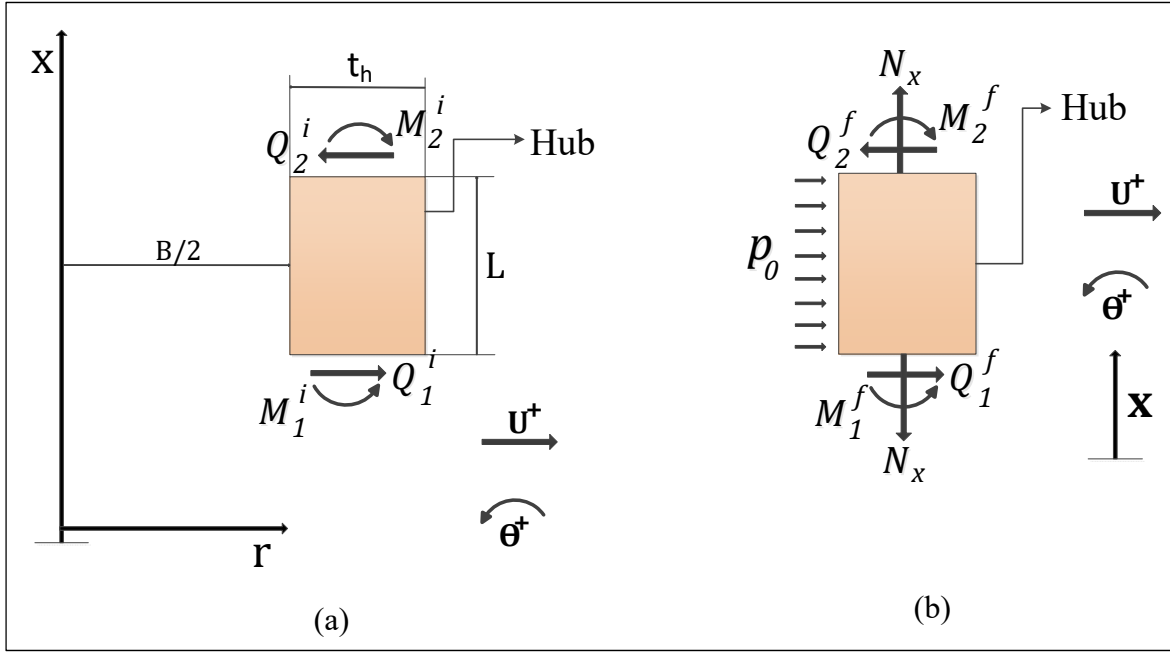
Figure 2-7 Analytical model of the hub (a) bolt-up and (b) pressurization

In this model, the length of the hub is considered short less than π/β and the thickness of the hub to its radius is less than 0.1 such that thin cylinder theory can be used. At the top and bottom surface of the hub, it is subjected to the discontinuity shear force Q and moment M in addition to the hydrostatic end force N_x.

As shown in figure 2.6:

Q_1^i and Q_1^f are the shear forces at the junction of the ring and the shell;

M_1^i and M_1^f are the bending moment at the junction of the ring and the shell;

p_o is a pressure on the inside surface of the shell;

N_x is the membrane force produced by the hydrostatic end force;

Similar to the shell analysis, due to the axial symmetry of the hub, none of the variables depends on the angle θ and consequently, all the partial derivatives with respect to θ are equal to zero.

The equilibrium equations of the hub can be derived as:

$$N_x = cste \tag{2.105}$$

$$\frac{dN_{x\theta}}{dx} + \frac{1}{r}\frac{dM_{x\theta}}{dx} = 0 \tag{2.106}$$

$$\frac{d^2 M_x}{dx^2} - \frac{N_\theta}{r} = -p_o \tag{2.107}$$

The relation between the stress resultants and strains are:

$$\begin{Bmatrix} N_x \\ N_y \\ N_{xy} \\ M_x \\ M_y \\ M_{xy} \end{Bmatrix} = \begin{bmatrix} A_{h,11} & A_{h,12} & A_{h,16} & B_{h,11} & B_{h,12} & B_{h,16} \\ A_{h,12} & A_{h,22} & A_{h,26} & B_{h,12} & B_{h,22} & B_{h,26} \\ A_{h,16} & A_{h,26} & A_{h,66} & B_{h,16} & B_{h,26} & B_{h,66} \\ B_{h,11} & B_{h,12} & B_{h,16} & D_{h,11} & D_{h,12} & D_{h,16} \\ B_{h,12} & B_{h,22} & B_{h,26} & D_{h,12} & D_{h,22} & D_{h,26} \\ B_{h,16} & B_{h,26} & B_{h,66} & D_{h,16} & D_{h,26} & D_{h,66} \end{bmatrix} \begin{Bmatrix} \varepsilon_x^0 \\ \varepsilon_y^0 \\ \gamma_{xy}^0 \\ \kappa_x \\ \kappa_y \\ \kappa_{xy} \end{Bmatrix} \tag{2.108}$$

where:

A_{ij}, B_i and D_{ij} are the stiffness coefficients and can be defined as follows:

$$A_{h,ij} = \sum_{k=1}^{N}(Q_{ij})_k (z_k - z_{k-1}) \tag{2.109}$$

$$B_{h,ij} = \frac{1}{2}\sum_{k=1}^{N}(Q_{ij})_k (z_k^2 - z_{k-1}^2) \tag{2.110}$$

$$D_{h,ij} = \frac{1}{3}\sum_{k=1}^{N}(Q_{ij})_k (z_k^3 - z_{k-1}^3) \tag{2.111}$$

According to the symmetrical laminate shell:

$A_{p,16} = A_{p,26} = 0$

$$A_{h,16} = 0$$

$$A_{h,26} = 0$$

$$[B] = 0,$$

The forces and moments resultant are further related to the shell displacement:

$$N_x = cste = A_{h,11} \frac{dw^0}{dx} - A_{h,12} \frac{u}{r} \tag{2.112}$$

$$N_\theta = A_{h,12} \frac{dw^0}{dx} - A_{h,22} \frac{u}{r} \tag{2.113}$$

$$M_x = -D_{h,11} \frac{d^2 u}{dx^2} \tag{2.114}$$

$$M_\theta = -D_{h,12} \frac{d^2 u}{dx^2} = -\frac{D_{h,12}}{D_{h,11}} M_r \tag{2.115}$$

$$M_{x\theta} = -\frac{D_{h,16}}{D_{h,11}} M_r \tag{2.116}$$

It is possible to obtain N_θ in term of N_x such that: as:

$$N_\theta = \frac{u}{r} \left(A_{h,22} - \frac{A_{h,12}^2}{A_{h,11}} \right) + \frac{A_{h,12}}{A_{h,11}} N_x \tag{2.117}$$

From equations (2.114) and (2.117) the following is obtained :

$$D_{h,11} \frac{d^4 u}{dx^4} + \frac{u}{r^2} \left(A_{h,22} - \frac{A_{h,12}^2}{A_{h,11}} \right) + \frac{A_{h,12}}{A_{h,11}} \frac{N_x}{r} = p_o \tag{2.118}$$

The radial displacement of the shell after integration is:

$$u = C_1 e^{\beta_h x} \cos(\beta_h x) + C_2 e^{\beta_h x} \sin(\beta_h x) + C_3 e^{-\beta_h x} \cos(\beta_h x) + C_4 e^{-\beta_h x} \sin(\beta_h x) \quad (2.119)$$

The general solution after simplification of the equation is:

$$u = e^{\beta_h x}[C_1 \cos(\beta_h x) + C_2 \sin(\beta_h x)] + e^{-\beta_h x}[C_3 \cos(\beta_h x) + C_4 \sin(\beta_h x)] \quad (2.120)$$

The rotation θ, Moment M and shear forces Q are given as follows:

$$\theta = \frac{du}{dx} \quad (2.121)$$

$$M_x = -D_{11} \frac{d^2 u}{dx^2} \quad (2.122)$$

$$Q = \frac{dM_x}{dx} = -D_{11} \frac{d^2 w}{dx^2} \quad (2.123)$$

The integral constants C_1, C_2, C_3 and C_4 will be determined from the boundary conditions.

At $x = 0$, then $M_x = M_I^n$ and $Q = Q_I^n$

At $x = l_h$, then $M_x = M_J^n$ and $Q = Q_J^n$

2.5 Axial compatibility:

The equations for compatibility requiring continuity of the rotation and radial displacement can be used with the equations of equilibrium to form a system of equations with nine unknowns for the pressurization state. The final bolt load F_B^f for the operating condition can be obtained from the geometric compatibility consideration in the axial direction that is the relation to the nut axial displacement that is equal during initial bolt-up and pressurization. Before applying the internal pressure, the bolt initial force F_B^i, which is the required bolt load to satisfy both the requirements of seating and operating conditions, should be previously

defined and therefore is known. Consequently, our system of equations will be reduced by one unknown.

Figure 2.8 illustrates the compatibility of displacement based on the axial distance traveled by the nut during the tightening process. It is to be noted that this distance is the sum of the displacement of the flange due to the rotation, the elongation of the bolt and the compression of the gasket all in the axial direction.
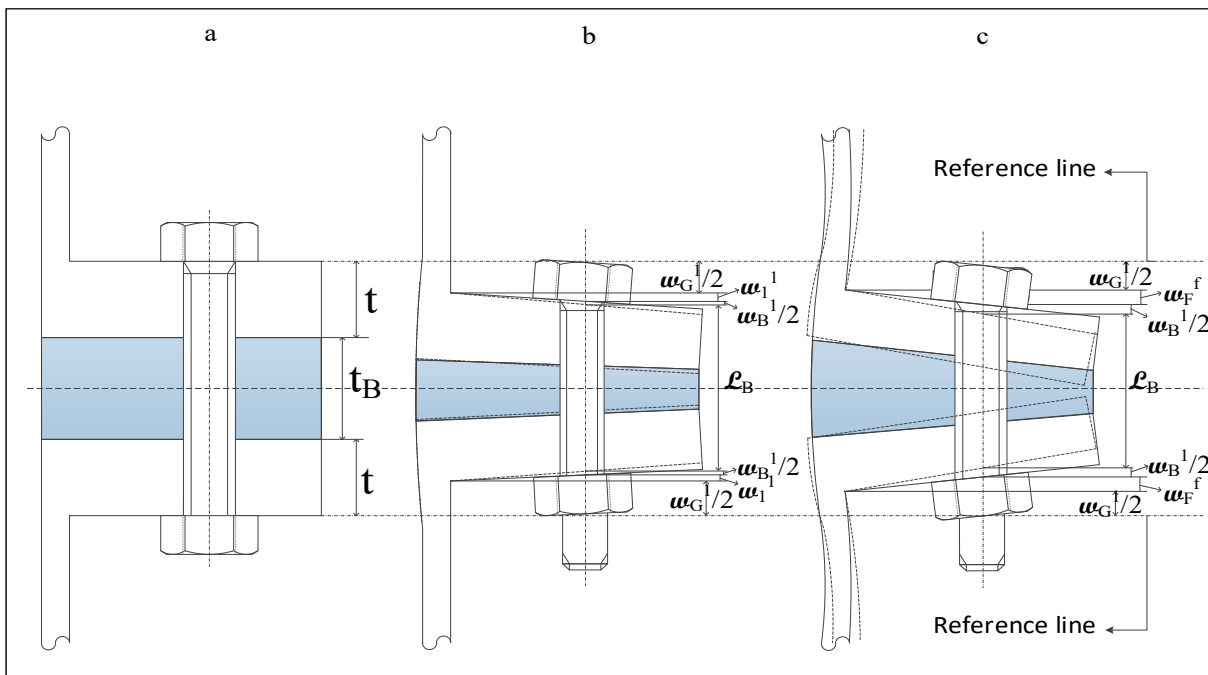
Figure 2-8 Axial compatibility of the joint a) hand tightening b) initial pre-tightening (Bolt-up), c) pressurization

The nut axial displacement corresponding to the actual number of turns necessary to achieve the required preload remains unchanged between the initial pre-tightening state (i) and during the final pressurization state (f). As a matter of fact, this axial displacement does not change from the initial state or bolt-up to any other state including pressure, temperature, bending and creep loading. As shown in figure 2.8 the sum of the axial displacement of all parts of the bolted flange joints is involved. At the junction of the three parts of the flange, the

displacements and rotations must be equal, based on the requirement of continuity. Therefore, the compatibility equations are as follows:

The radial displacements and rotations of the ring are equal to the radial displacements and rotations of the hub at point 1:

Initial pre-tightening state (i)

$$\psi_{1,p}^{i} = \psi_{1,h}^{i} \tag{2.124}$$

$$u_{1,p}^{i} = u_{1,h}^{i} \tag{2.125}$$

Final pressurization state (f)

$$\psi_{1,p}^{f} = \psi_{1,h}^{f} \tag{2.126}$$

$$u_{1,p}^{f} = u_{1,h}^{f} \tag{2.127}$$

The radial displacements and rotations of the hub are equal to the radial displacements and rotations of the shell at point 2.

Initial pre-tightening state (i)

$$\psi_{2,h}^{i} = \psi_{2,s}^{i} \tag{2.128}$$

$$u_{2,h}^{i} = u_{2,s}^{i} \tag{2.129}$$

Final pressurization state (f)

$$\psi_{2,h}^{f} = \psi_{2,s}^{f} \tag{2.130}$$

$$u_{2,h}^{f} = u_{2,s}^{f} \tag{2.131}$$

Considering the axial equilibrium

Initial pre-tightening state (i)

$$F_B^i = F_G^i \tag{2.132}$$

Final pressurization state (f)

$$F_B^f = F_G^f + p_o A_p \tag{2.133}$$

And according to the axial compatibility

$$\sum_{i=1}^{m} w_i^i = \sum_{i=1}^{m} w_i^f \tag{2.134}$$

or

$$w_B^i + w_G^i + w_P^i = w_b^f + w_g^f + w_p^f \tag{2.135}$$

Substituting the displacements and rotations into (2.135), the following is obtained:

$$\frac{F_B^i}{K_B} + \frac{F_G^i}{K_G} + 2(r_B - r_G)\psi_{1,p}^i = \frac{F_B^f}{K_B} + \frac{F_G^f}{K_G} + 2(r_B - r_G)\psi_{1,p}^f \tag{2.136}$$

Substituting equations (2.133) and (2.134) gives:

$$F_B^f \left(\frac{1}{K_B} + \frac{1}{K_G} \right) = \left(\frac{1}{K_B} + \frac{1}{K_G} \right) F_B^i + 2(r_B - r_G)({\psi_{1,p}}^i - {\psi_{1,p}}^i) + \frac{A_P}{K_G} p_o \tag{2.137}$$

After assembling the above equations, a system of 9 unknowns is obtained and it is possible to set these equations in a matrix form to solve for the unknowns.

$$[U] = [C]\backslash[V] \tag{2.138}$$

where $[C]$ is a square matrix and $[V]$ is a vector. The matrix $[U]$ is a vector the elements of which are the unknowns and are the edges forces and moments, the radial displacements and the rotations of each junction.

The coefficients matrixes are defined as follows:

$$[C] = \begin{bmatrix} \frac{-B11}{2\beta_h{}^3 D_{h,11}} & \frac{B12}{2\beta_h{}^2 D_{h,11}} & \frac{G11}{2\beta_h{}^3 D_{h,11}} & \frac{G12}{2\beta_h{}^2 D_{h,11}} & -1 & 0 & 0 & 0 & 0 \\[2mm] \frac{-B12}{2\beta_h{}^2 D_{h,11}} & \frac{B22}{2\beta_h D_{h,11}} & \frac{G12}{2\beta_h{}^2 D_{h,11}} & \frac{G22}{2\beta_h D_{h,11}} & 0 & -1 & 0 & 0 & 0 \\[2mm] \frac{-G11}{2\beta_h{}^3 D_{h,11}} & \frac{G12}{2\beta_h{}^2 D_{h,11}} & \frac{B11}{2\beta_h{}^3 D_{h,1}} & \frac{B12}{2\beta_h{}^2 D_{h,11}} & 0 & 0 & -1 & 0 & 0 \\[2mm] \frac{G12}{2\beta_h{}^2 D_{h,11}} & \frac{-G22}{2\beta_h D_{h,11}} & \frac{-B12}{2\beta_h{}^2 D_{h,11}} & \frac{-B22}{2\beta_h D_{h,11}} & 0 & 0 & 0 & -1 & 0 \\[2mm] \frac{1}{2\beta_s{}^3 D_{s,11}} & \frac{1}{2\beta_s{}^2 D_{s,11}} & 0 & 0 & -1 & 0 & 0 & 0 & 0 \\[2mm] \frac{-1}{2\beta_s{}^2 D_{s,11}} & \frac{-1}{\beta_s D_{s,11}} & 0 & 0 & 0 & -1 & 0 & 0 & 0 \\[2mm] 0 & 0 & -(L_{21} - L_{22}) & 0 & 0 & 0 & -1 & \frac{t_f}{2} & 0 \\[2mm] 0 & 0 & \frac{t_f}{2} L_{26} & -L_{26} & 0 & 0 & 0 & -1 & \frac{r_B - r_G}{2\pi r_m} L_{27} \\[2mm] 0 & 0 & 0 & 0 & 0 & 0 & 0 & 2(r_B - r_G) & \frac{1}{K_B} + \frac{1}{K_G} \end{bmatrix} \quad (2.139)$$

$$[V] = \begin{bmatrix} -\dfrac{A_{h,11} - \frac{1}{2}A_{h,12}}{4\beta_h{}^4 A_{h,1} D_{h,11}} p_o \\[3mm] 0 \\[2mm] -\dfrac{A_{h,11} - \frac{1}{2}A_{h,12}}{4\beta_h{}^4 A_{h,1} D_{h,11}} p_o \\[3mm] 0 \\[2mm] -\dfrac{A_{s,11} - \frac{1}{2}A_{s,12}}{4\beta_s{}^4 A_{s,11} D_{s,11}} p_o \\[3mm] 0 \\[2mm] -(L1 - L2)t_f p_o \\[2mm] -(r_G - r_i)(r_G{}^2 + r_i{}^2)\dfrac{p_o}{4 r_m} L_{27} \\[2mm] \left(\dfrac{1}{K_B} + \dfrac{1}{K_G}\right) F_B^i + 2(r_B - r_G)\psi_J{}^i + \dfrac{A_P}{K_G} p_o \end{bmatrix} \quad (2.140)$$

To simplify the derivations the following coefficients are defined:

$$L_{21} = \frac{-r_i{}^3}{(r_o{}^2 - r_i{}^2)(A_{p,12} + A_{p,11})} \tag{2.141}$$

$$L_{22} = \frac{-r_i r_o{}^2}{(r_o{}^2 - r_i{}^2)(A_{p,12} - A_{p,11})} \tag{2.142}$$

$$L_{23} = \frac{r_i - 2r_i \log\left(\frac{r_i}{r_o}\right)}{8\pi D_{p,11}} \tag{2.143}$$

$$L_{24} = -\frac{(r_o{}^2 r_i + r_i{}^3)(D_{p,12} - D_{p,11}) + 2r_i{}^3 \log\left(\frac{r_i}{r_o}\right)(D_{p,11} + D_{p,12})}{8\pi D_{p,11}(r_o{}^2 - r_i{}^2)(D_{p,11} + D_{p,12})} \tag{2.144}$$

$$L_{25} = \frac{-r_o{}^2 r_i \log\left(\frac{r_i}{r_o}\right)(D_{p,11} + D_{p,12})}{4D_{p,11}\pi(r_o{}^2 - r_i{}^2)(D_{p,11} - D_{p,12})} \tag{2.145}$$

$$L_{26} = L_{21} + L_{22} \tag{2.146}$$

$$L_{27} = L_{23} + L_{24} + L_{25} \tag{2.147}$$

To obtain the final bolt force $F_B{}^f$ which depends on the flange parameters as well as the inside pressure, first the unknown vector $[U^i]$ has to be solved for the initial bolt-up condition with a known initial bolt force $F_B{}^i$. The solution gives, in particular, the rotation of the flange in the initial tightening condition that used in the last row in $[U^f]$ of the final condition to solve for the bolt force $F_B{}^f$.

$$[U^i] = \begin{bmatrix} Q_2{}^i \\ M_2{}^i \\ Q_1{}^i \\ M_1{}^i \\ u_2{}^i \\ \psi_2{}^i \\ u_1{}^i \\ \psi_1{}^i \\ F_B{}^i \end{bmatrix} \qquad (2.148)$$

$$[U^f] = \begin{bmatrix} Q_2{}^f \\ M_2{}^f \\ Q_1{}^f \\ M_1{}^f \\ u_2{}^f \\ \psi_2{}^f \\ u_1{}^f \\ \psi_1{}^f \\ F_B{}^f \end{bmatrix} \qquad (2.149)$$

2.6 Stress calculation

To calculate the stresses and displacements for either the flange with the hub or without the hub, the solution of the two vectors $[U^i]$ and $[U^f]$ is conducted one after the other. The case of the flange without the hub could be treated as one with the hub having the same materials and thickness as the shell. In fact, these results make it possible to calculate the following parameters in the initial n=i and final n=f phases of the bolted flange joint:

$u^n(x)$ Radial displacement

$\Psi^n(x)$ Rotation

$M^n(x)$ Bending moment

$Q^n(x)$ Shearing force

$N_l{}^n(x)$ Longitudinal force

$N_t{}^n(x)$ Tangential force

$\sigma_{l,i}{}^{n}$	Longitudinal stress inside surface of the flange
$\sigma_{t,i}{}^{n}$	Tangential stress inside surface of the flange
$\sigma_{l,o}{}^{n}$	Longitudinal stress outside the surface of the flange
$\sigma_{t,o}{}^{n}$	Tangential stress outside the surface of the flange

2.6.1   Hub laminate:

Equations (2.150) to (2.153) below are used to calculate the displacement and stresses in the hub:

$$F_{11}(\beta_h x) = \frac{1}{2}[\cosh(\beta_h x)\sin(\beta_h x) - \sinh(\beta_h x)\cos(\beta_h x)] \qquad (2.150)$$

$$F_{12}(\beta_h x) = \sin(\beta_h x)\sinh(\beta_h x) \qquad (2.151)$$

$$F_{13}(\beta_h x) = \frac{1}{2}[\cosh(\beta_h x)\sin(\beta_h x) + \sinh(\beta_h x)\cos(\beta_h x)] \qquad (2.152)$$

$$F_{14}(\beta_h x) = \cosh(\beta_h x)\cos(\beta_h x) \qquad (2.153)$$

Substituting the above equations, the lamina displacement, rotation, moment and shear, and membranes forces in the hub can be determined from the following relations:

$$u_h{}^n(x) = \frac{Q_1{}^n}{2\beta_h{}^3 D_{h,11}} F_{11}(\beta_h x) + \frac{M_1{}^n}{2\beta_h{}^2 D_{h,11}} F_{12}(\beta_h x) + \frac{\psi_1{}^n}{\beta_h} F_{13}(\beta_h x) + u_1{}^n F_{14}(\beta_h x) \qquad (2.154)$$

$$\psi_h{}^n(x) = \beta_h \left[\frac{Q_1{}^n}{2\beta_h{}^3 D_{h,11}} F_{12}(\beta_h x) + \frac{M_1{}^n}{\beta_h{}^2 D_{h,11}} F_{13}(\beta_h x) + \frac{\psi_1{}^n}{\beta_h} F_{14}(\beta_h x) - 2u_1{}^n F_{11}(\beta_h x) \right]$$

$$(2.155)$$

$$M_h{}^n(x) = 2\beta_h{}^2 D_{h,11} \left[\frac{Q_1{}^n}{2\beta_h{}^3 D_{h,11}} F_{13}(\beta_h x) + \frac{M_1{}^n}{2\beta_h{}^2 D_{h,11}} F_{14}(\beta_h x) - \frac{\psi_1{}^n}{\beta_h} F_{11}(\beta_h x) - \right.$$

$$\left. u_1{}^n F_{12}(\beta_h x) \right] \qquad (2.156)$$

$$Q_h{}^n(x) = 2\beta_h{}^3 D_{h,11}\left[\frac{Q_1{}^n}{2\beta_h{}^3 D_{h,11}}F_{14}(\beta_h x) - \frac{M_1{}^n}{\beta_h{}^2 D_{h,11}}F_{11}(\beta_h x) - \frac{\psi_1{}^n}{\beta_h}F_{12}(\beta_h x) - \right.$$

$$\left. 2u_1{}^n F_{13}(\beta_h x)\right] \tag{2.157}$$

$$N_{h,l}{}^i(x) = 0 \quad and \quad N_{h,l}{}^f(x) = \frac{p_0 r_h}{2} \tag{2.158}$$

$$N_{h,t}{}^n(x) = \left[\frac{u_h{}^n(x)}{r_h} + \frac{\left(A_{h,11} - \frac{A_{h,12}}{2}\right)}{4\beta_h{}^4 A_{h,11} D_{h,11}}\frac{p_0}{r_h}\right]\left(A_{h,12} - \frac{A_{h,22}{}^2}{A_{h,11}}\right) + \frac{A_{h,12}}{A_{h,11}}N_{h,l}{}^n(x) \tag{2.159}$$

The longitudinal and tangential stresses at the inside and outside surface of the hub are given by:

$$\sigma_{h,l,i}{}^n(x) = \frac{N_{h,l}{}^n(x)}{t_h} + \frac{6M_h{}^n(x)}{t_h{}^2} \tag{2.160}$$

$$\sigma_{h,l,o}{}^n(x) = \frac{N_{h,l}{}^n(x)}{t_h} - \frac{6M_h{}^n(x)}{t_h{}^2} \tag{2.161}$$

$$\sigma_{h,t,i}{}^n(x) = \frac{N_{h,t}{}^n(x)}{t_h} + \frac{6D_{h,12}}{D_{h,11}}\frac{M_h{}^n(x)}{t_h{}^2} \tag{2.162}$$

$$\sigma_{h,t,o}{}^n = \frac{N_{h,t}{}^n(x)}{t_h} - \frac{6D_{h,12}}{D_{h,11}}\frac{M_h{}^n(x)}{t_h{}^2} \tag{2.163}$$

2.6.2   Shell laminate

Equations (2.164) to (2.167) must be used to calculate the displacement and stresses in the shell:

$$f_1(\beta_s x) = e^{-\beta_s x}[\cos(\beta_s x)] \tag{2.164}$$

$$f_2(\beta_s x) = e^{-\beta_s x}[\cos(\beta_s x) - \sin(\beta_s x)] \tag{2.165}$$

$$f_3(\beta_s x) = e^{-\beta_s x}[\cos(\beta_s x) + \sin(\beta_s x)] \tag{2.166}$$

$$f_4(\beta_s x) = e^{-\beta_s x}[\sin(\beta_s x)] \tag{2.167}$$

Substituting the above equations, the lamina displacement, rotation, moment and shear and membranes forces in the shell can be determined from the following relations:

$$u_s{}^n(x) = \frac{Q_2{}^n}{2\beta_s{}^3 D_{s,11}} f_1(\beta_s x) + \frac{M_2{}^n}{2\beta_s{}^2 D_{s,11}} f_2(\beta_s x) \tag{2.168}$$

$$\psi_s{}^n(x) = \beta_s \left[-\frac{Q_2{}^n}{2\beta_s{}^3 D_{s,11}} f_3(\beta_s x) - \frac{M_2{}^n}{\beta_s{}^2 D_{h,11}} f_1(\beta_s x) \right] \tag{2.169}$$

$$M_s{}^n(x) = 2\beta_s{}^2 D_{s,11} \left[\frac{Q_2{}^n}{2\beta_s{}^3 D_{s,11}} f_4(\beta_s x) + \frac{M_2{}^n}{2\beta_s{}^2 D_{s,11}} f_3(\beta_s x) \right] \tag{2.170}$$

$$Q_s{}^n(x) = 2\beta_s{}^3 D_{s,11} \left[\frac{Q_2{}^n}{2\beta_s{}^3 D_{s,11}} f_2(\beta_s x) - \frac{M_2{}^n}{\beta_s{}^2 D_{s,11}} f_4(\beta_s x) \right] \tag{2.171}$$

$$N_{s,l}{}^i(x) = 0 \quad and \quad N_{s,l}{}^f(x) = \frac{p_0 r_s}{2} \tag{2.172}$$

$$N_{s,t}{}^n(x) = \left[\frac{u_s{}^n(x)}{r_s} + \frac{\left(A_{s,11} - \frac{A_{s,12}}{2}\right)}{4\beta_s{}^4 A_{s,11} D_{s,11}} \frac{p_0}{r_s} \right] \left(A_{s,22} - \frac{A_{s,12}{}^2}{A_{s,11}} \right) + \frac{A_{s,12}}{A_{s,11}} N_{s,l}{}^n(x) \tag{2.173}$$

The longitudinal and tangential stresses at the inside and outside surface of the shell are given by:

$$\sigma_{s,l,i}{}^n(x) = \frac{N_{s,l}{}^n(x)}{t_s} + \frac{6M_s{}^n(x)}{t_s{}^2} \tag{2.174}$$

$$\sigma_{s,l,o}{}^n(x) = \frac{N_{s,l}{}^n(x)}{t_s} - \frac{6M_s{}^n(x)}{t_s{}^2} \tag{2.175}$$

$$\sigma_{s,t,i}{}^n(x) = \frac{N_{s,t}{}^n(x)}{t_s} + \frac{6D_{s,12}}{D_{s,11}} \frac{M_s{}^n(x)}{t_s{}^2}$$

(2.176)

$$\sigma_{s,t,o}{}^n(x) = \frac{N_{s,t}{}^n(x)}{t_s} - \frac{6D_{s,12}}{D_{s,11}} \frac{M_s{}^n(x)}{t_s{}^2}$$

(2.177)

CHAPTER 3

NUMERICAL (FINITE ELEMENT) MODELING

3.1   Introduction

To investigate the behavior of complicated structure like FRP flanges which is difficult to analyze all elements analytically one of the best techniques is the finite element model. FEM is a useful way to provide an acceptable prediction of the behavior of a complex structure. To get the highest accuracy, it requires creating a model with the fine meshing system by means of various elements, that reflects perfectly specifications of the system including the material properties, structures, and the assembly.

The presented numerical models for FRP bolted flange joints in this chapter are an attempt to validate the analytical model. Besides this, finite element analysis cannot duplicate experimental testing exactly, therefore, the experimental tests have been conducted on FRP bolted joints to validate the results obtained from experimental, analytical and numerical methods. In addition, to validate the analytical model, finite element analysis gives us an indication of the overall behavior and performance of FRP bolted joint.

This chapter describes the numerical procedure of the 3 different models of Fiber reinforced plastic flanges for two sizes of the flange with NPS 3 class 150 and NPS 12 class 150. To create and analyzed the finite element models, the program ANSYS® Mechanical 16.02 and ANSYS Composite PrepPost (ACP) 16.2 were used.

The three finite element models considered in this chapter are:
   1- Finite element model for the flange without the hub;
   2- Finite element model for the flange with the hub;
   3- Finite element model with ANSYS Composite PrepPost (ACP).

Each finite element model of the bolted joint consists of two phases:

- Initial tightening phase: the first stage is at the flange bolt-up following the initial tightening of the flange. The tightening force compresses the two parts of the flange as well as the gasket and it is represented by a uniform and horizontal distribution of the contact pressure.

- Pressurization phase: A pressure is applied on the inside surface of the flange; the inside pressure also creates a pressure on the flat surfaces at the end of the shell of the flange.

3.2   Applied loading

The loading consists of the hydrostatic end load, internal lateral pressure, and initial bolt forces. The initial gasket seating is provided by the pre-load in the bolts and is referred to as the seating condition. In this case, the gasket deforms filling the irregularities on the flange face in order to make a full contact over its entire surface. The bolt load change during pressurization can be obtained from the compatibility of displacement. In order to study the short-term behavior of FRP bolted joints, the bolt load is assumed to remain constant as in practice, by retightening the bolts, they maintain the required load to prevent leakage. It is worth noting that in the real case, creep and relaxation can happen in the flange and gasket. This issue of load relaxation is complex to consider because of the creep of the resin and woven roving of the composite material, the data of which are not available. In all models, the tightening forces are applied at the same time and they are identical. Therefore, this hypothesis allows us to consider the bolted flange joint model as axisymmetric, and just 1/4 and 1/12 can be modeled for the flange with NPS 3 and NPS 12 respectively.

3.2.1   Pretension load on bolts

In the FE model, the bolt force is applied as the pre-tension load and then the position is locked in the subsequent stage. The material properties of the bolts are given in table 3.1.

Table 3-1 Material properties of the bolts

Properties	Value	Unit
Young Modulus	210	GPa
Poisson's ratio	0.3	
Tensile yield strength	250	MPa
Tensile ultimate strength	460	MPa
Density	7,850	kg/m^3

To get the proper sealing in the bolted flange joints assembly the following conditions must be met:

- Sufficient compression force must be applied to fill the porosities on the face of the flanges.
- A minimum compression force must be maintained on the joint during the operating condition to ensure the proper sealing of the joint.

In order to determine the required compressive force to satisfy the above conditions, the following equations are used:

$$W_{m2} = \pi b G y \tag{3.1}$$

$$W_{m1} = \frac{\pi}{4} G^2 p_0 + 2 b \pi G m p_0 \tag{3.2}$$

where W_{m2} and W_{m1} are the initial tightening bolt force and the operating bolt force respectively.

The minimum bolt force required to seal the bolted flange joint (W_m) is the maximum force between W_{m2} and W_{m1}.

The pretension load on the bolts is determined from:

$$S_b = \frac{F_b}{A_b} \tag{3.3}$$

$$A_b = \pi r_v{}^2 \tag{3.4}$$

where S_b is the tightening stress of the bolt, F_b is the bolt force and A_b is the bolt stress area.

According to the ASME BPV Code, Sections X, it is possible to calculate the bolt stress area as follow:

$$A_b = \pi \left[\left(\frac{d_3}{2} + \frac{d_2}{2}\right)/2\right]^2 \tag{3.5}$$

$d_3 = d_v - 1.2268pt$
$d_2 = d_v - 0.6495pt$

Then

$$A_b = \pi \left[\frac{2d_v - 1.8763pt}{4}\right]^2 \tag{3.6}$$

Table 3-2 Bolt stress and bolt force for the NPS 3 and 12 FRP bolted flange joint

Flange size	A_b (mm^2)	F_b (N)
NPS 3	197.84	14580
NPS 12	388.15	10000

In ANSYS® Mechanical the torque load is applied through the pre-existing command called "bolt pretension". To apply the axial bolt load as shown in figure 3.1, a special coordinate system is created at the center of the bolt. Then the bolt load is applied in two steps. In the first step, the pre-tightening bolt force is applied then it is locked to maintain the torque load for the subsequent steps.
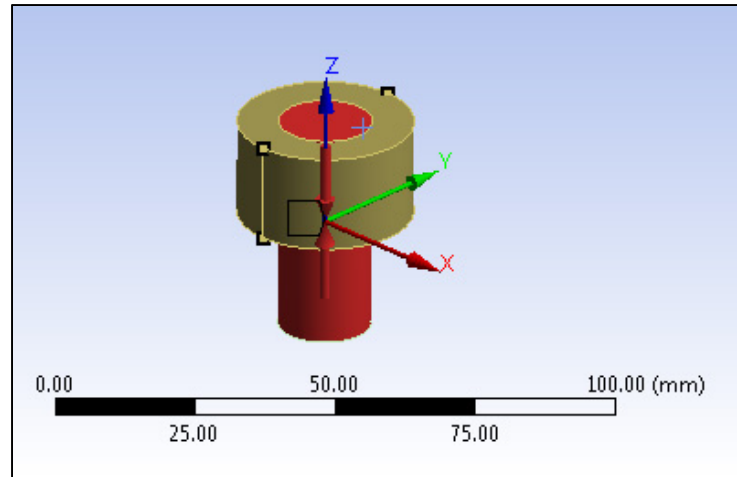
Figure 3-1 Axial bolt load with a special coordinate system

3.2.2   Internal pressure

When the pre-tightening bolt force is applied to each bolt on the flange, the pressurization phase has begun. The pressure that is applied on the internal surface of the flanges with NPS 3 and 12 is 1.034 MPa (150 Psi) and 0.345 MPa (50 Psi). As shown in figure 3.2 the inside pressure creates a pressure on the top surface of the shell in the flanges. This stress that applies to the end of the flange is equal for both flanges and given by:

$$p_w = \frac{p_o A_p}{A_S} \tag{3.7}$$

$$A_p = \pi r_i^2 \tag{3.8}$$

$$A_S = \pi(r_i + t_s)^2 - A_p \tag{3.9}$$

Then

$$p_w = \frac{p_o r_i^2}{(2r_i + t_s)t_s} \tag{3.10}$$

where p_o is the inside pressure, r_i is the flange inside radius, t_s is the thickness of the shell, A_p is the inside surface area of the flange and A_S is the cross-section area of the shell. The applied pressure in the flanges with NPS 3 and 12 are listed in table 3.3.
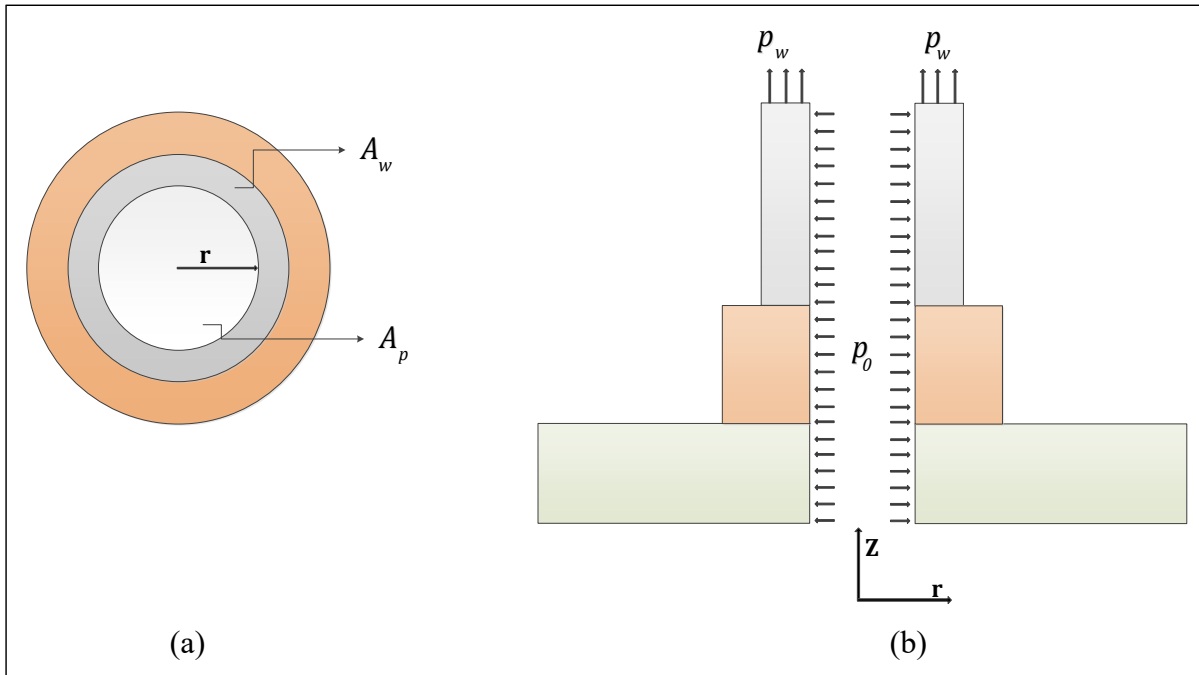
Figure 3-2 Inside pressure p_o and wall pressure p_w at pressurization phase

Table 3-3 Inside pressure and wall pressure for NPS 3 and 12 FRP flange

Flange size	p_o (MPa)	p_w (MPa)
NPS 3	1.034	2.86
NPS 12 with the hub	1.034	4.27
NPS 12 without the hub	0.345	1.5

3.3   Modeling of the gasket

One of the key factors in successful bolted joint simulation is the modeling of the gasket material. The gasket compression, especially in full-face flanges, has a strong influence on the flange rotation and leakage performance. In full-face flanges, the gasket is compressed

unevenly and in order to resist the fluid inside pressure, the bolts must be tight enough. In this model, the gasket deforms plastically under the flange surfaces, ensuring full contact over its entire area. The mechanical behavior of the gasket is represented by nonlinear loading and unloading curves obtained from load-displacement tests. Figure 3.3 depicted test data of a Teflon gasket that is used in this study. The geometry of the gasket for NPS 3 and 12 flanges are listed in table 3.4.
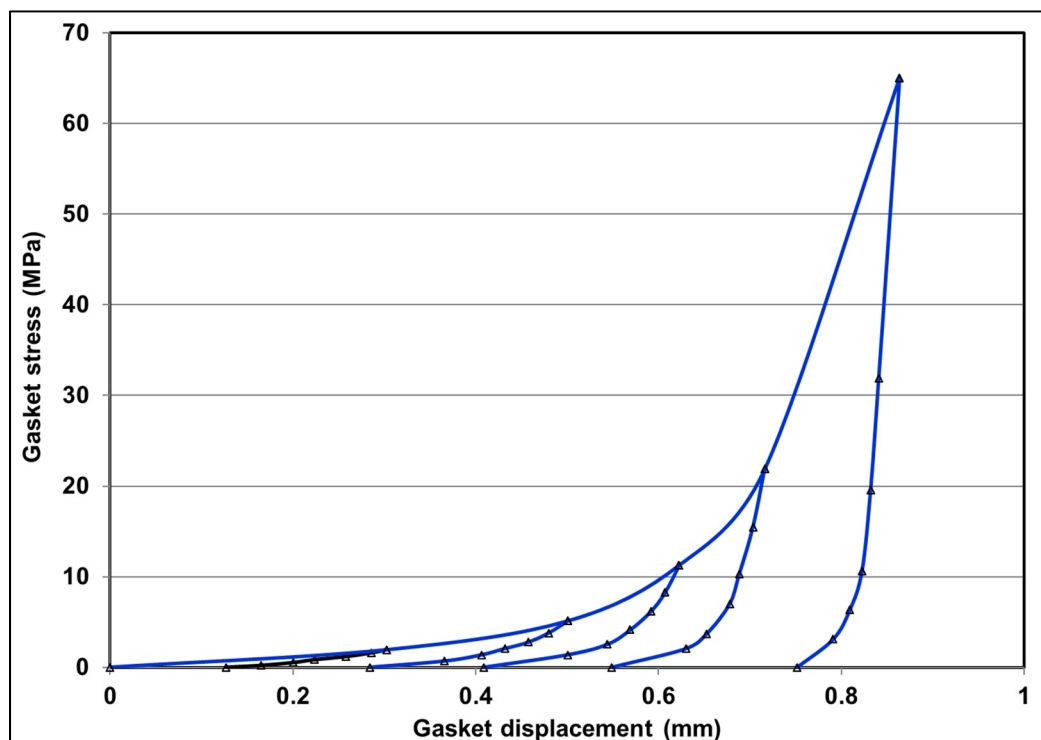
Figure 3-3 Gasket compression tests

Four critical steps are likely to occur during gasket compression from the initial tightening to pressurization. In composite flanges using the full-face width, the compression stresses of the joint are zero at the holes of bolts. As depicted in figure 2.8, flange bolt-up is conducted first by hand followed by tightening with a torque ranch where the gasket compression is achieved by a non-uniform distribution of the contact pressure. The flange joint is gradually pressurized and in general, a more pronounce trapezoidal distribution takes place. In this phase, the flange rotates while the inside region of the compressed gasket unloads. Therefore, the contact pressure follows a trapezoidal distribution with a minimum contact pressure at the inner radius

of the gasket and maximum contact pressure at the outer radius of the gasket. Usually, too much rotation will cause the loosing of the contact pressure at the bolt holes, in which case leakage will occur at this location.

Table 3-4 Geometry of the gasket for the flange with NPS 3 and 12

Flange size	Inside diameter	Outside diameter	Thickness	Number of holes	Hole diameter	Hole circle
NPS 12	304.8	482.6	3	12	25.4	431.8
NPS 3	76.2	190.5	1.59	4	19.05	152.4

In order to simplify the numerical model, the gasket contact pressure distributions are considered to be triangular.

3.4 Boundary conditions

Because of the axisymmetry, the boundary conditions applied to the finite element models are the symmetry conditions to the nodes that belong to both sides of the two axial planes of the flange triangular portion and to those that are in the plane that passes through the middle of the gasket thickness. As depicted in figure 3.4 the axial displacement in the middle of the gasket and the bolt is zero. The nodes of the flange symmetrical plane are free to move in the radial direction while their rotation about any radius is fixed.

Since the flange is symmetrical in nature, the cyclic symmetry is applied at two sides of the cut section as shown in figure 3.5. The axial displacement at the plane that passes through the gasket mid-thickness and cuts the bolts in two parts is constrained the flange face is expected to compress the gasket over the full face once the bolt load is applied. It is worth noting that the shell length should be long enough to eliminate the edge effects at top. This simplified

model limits the CPU requirements and makes the calculations faster. A standard friction model was used to control sliding at the bolt-flange and gasket-flange interfaces. The coefficient of static friction of 0.7 for rough surface and 0.15 for a smoother surface.
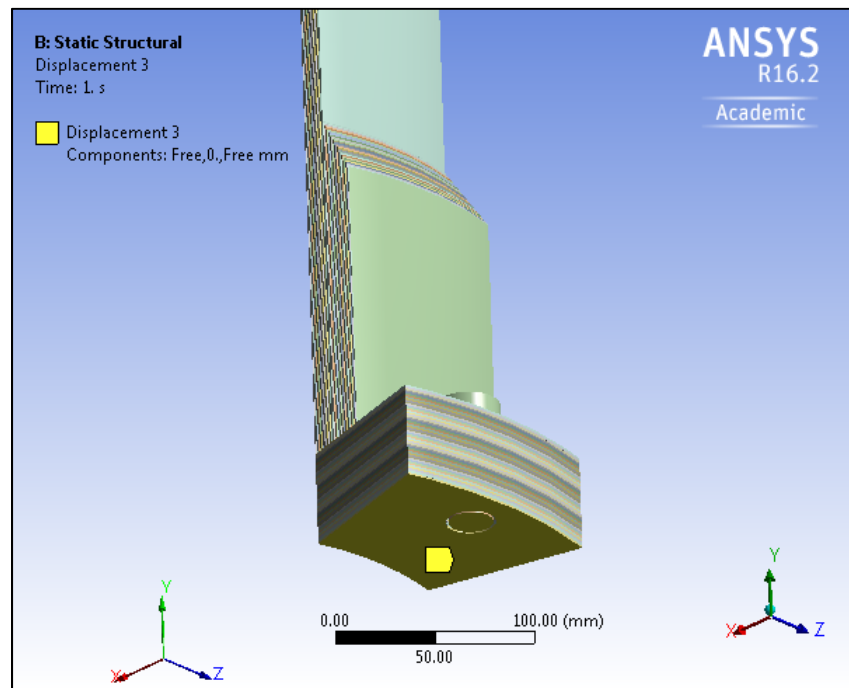
Figure 3-4 Boundary condition for the static model

3.5   3D solid finite element models

The numerical Finite element analysis was conducted on 3 different models to compare the results obtained with the developed analytical FRP bolted flange model. The axisymmetric model assembly is made of three parts; the flange, the gasket ring, and the bolt. In the case of an assembly with an identical flange pair, because of symmetry with respect to a plane that passes through the gasket thickness, only one flange including half of the gasket thickness is modeled. To model the flange and bolts, 3D 8-node brick solid element (Solid185) was used. These elements are defined by three degrees of freedom per nodes and support plasticity, large deflection and high strain capabilities. In addition, the contact pairs which consist of contact elements (CONTACT174) and target segment elements (TARGE170) were defined the

interface between the flange, gasket, and bolts. The volume elements were used to model the Existing space between the flange and the bolt. The flanged connection is assumed to be sufficiently far from the end enclosures of the vessel, such that the longitudinal and bending is limited only to its small adjacent portion of the vessel compared to the overall length. In order to conduct a direct comparison between the results obtained from the analytical model and numerical model, the two working conditions, initial pre-tightening (bolt-up) and pressurization, are analyzed.
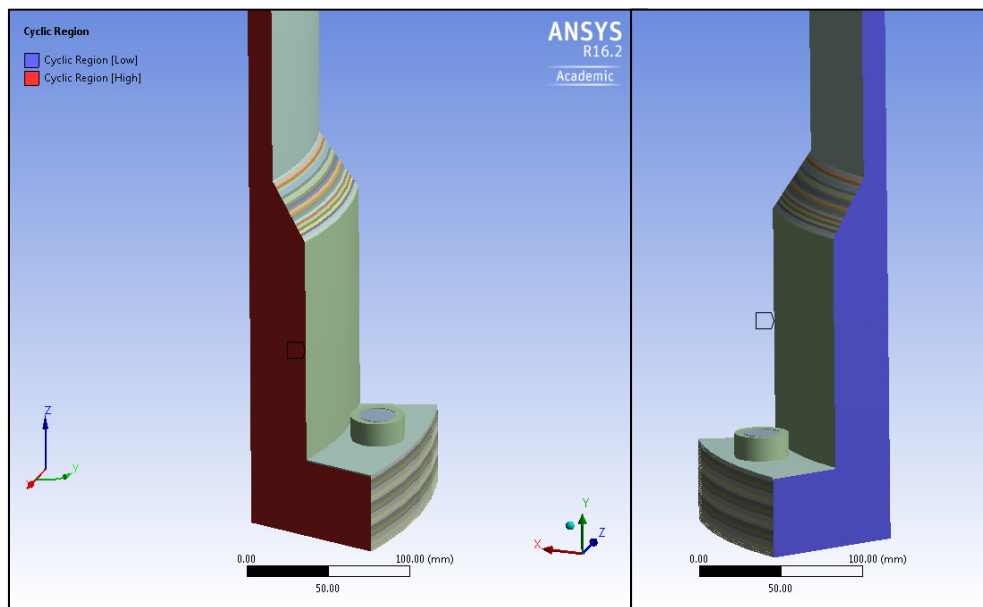
Figure 3-5 Symmetry surfaces of static model

3.5.1   Finite element model for the flange with NPS 12 class 150

Two different finite element models of the NPS 12 class 150 and 50 of FRP bolted flanged joint were developed under the software ANSYS® Mechanical 16.02. As shown in figures 3.6 and 3.7, the first model is the flange without the hub and the second one is the flange with the hub. A linear static finite element analysis was performed with these two models. The 3D model includes three parts; the flange, the gasket, and the bolt. In the case of an assembly with an identical flange pair, because of symmetry with respect to a plane that passes through the mid gasket thickness, only one flange including half of the gasket thickness is modeled.
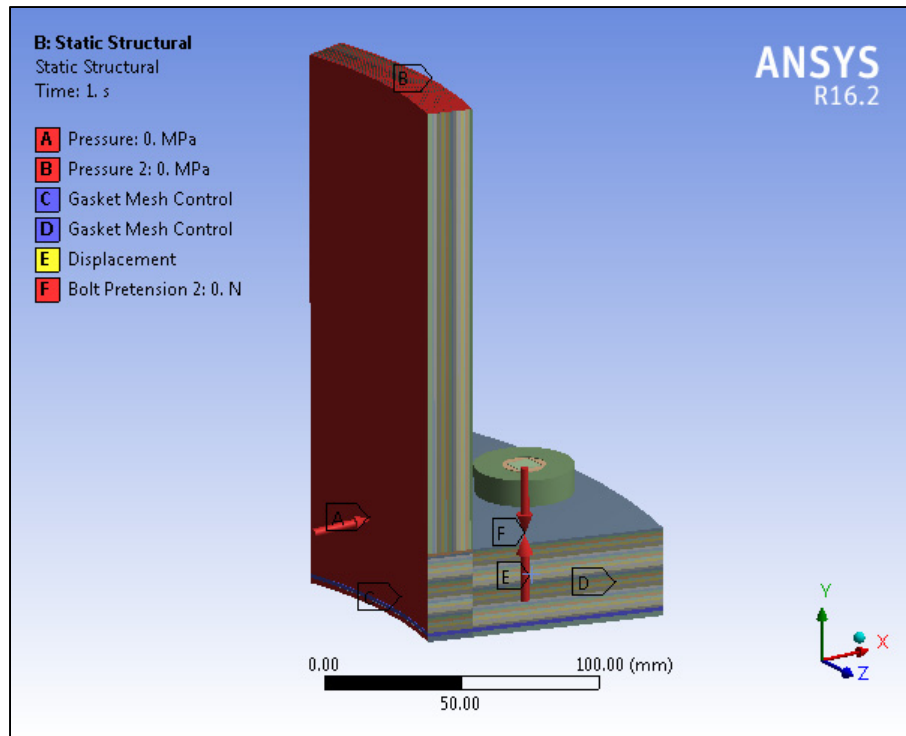
Figure 3-6 Finite element model for the NPS 12 FRP flange without the hub

3.5.1.1 Geometry of the flange

Figure 3.8 and 3.10 illustrate the geometric features of the NPS 12 flanges with the hub and without the hub, that are valid for the class 150 and 50 respectively. The flange dimensions (table 3.5) were obtained from the ASME code section X. The thicknesses of the ring, hub, and shell are not definitive in the finite element model, depending on the arrangement of the laminate in each part of the FRP bolted flange joint. The arrangement of the laminate in the flange is elaborated in 3.5.1.3.
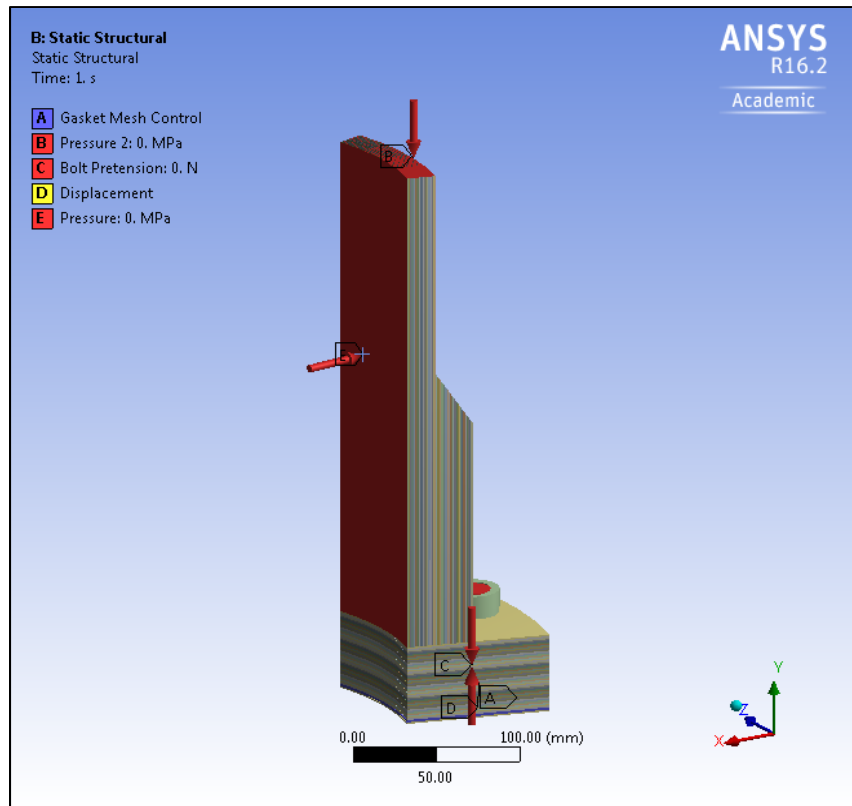
Figure 3-7 Finite element model for the NPS 12 FRP flange with
the hub

The flanged connection is assumed to be sufficiently far from the end enclosures of the vessel, such that the shear and bending loads are limited only to the small adjacent portion of the shell and do not influence the hub. FRP flanges with and without the hub are designed based on the geometry mentioned above and are drawn in Catia software. The generated models are then transferred directly to ANSYS. Figure 3.9 and 3.11 show the designed flanges with Catia for the NPS 12 FRP flanges.

According to the geometry of the flange (table 3.5 and 3.6), the thickness of the ring is equal to FT which is 47.62 mm and 30 mm for the NPS 12 flange with the hub class 150 and the NPS 12 flange without the hub respectively.
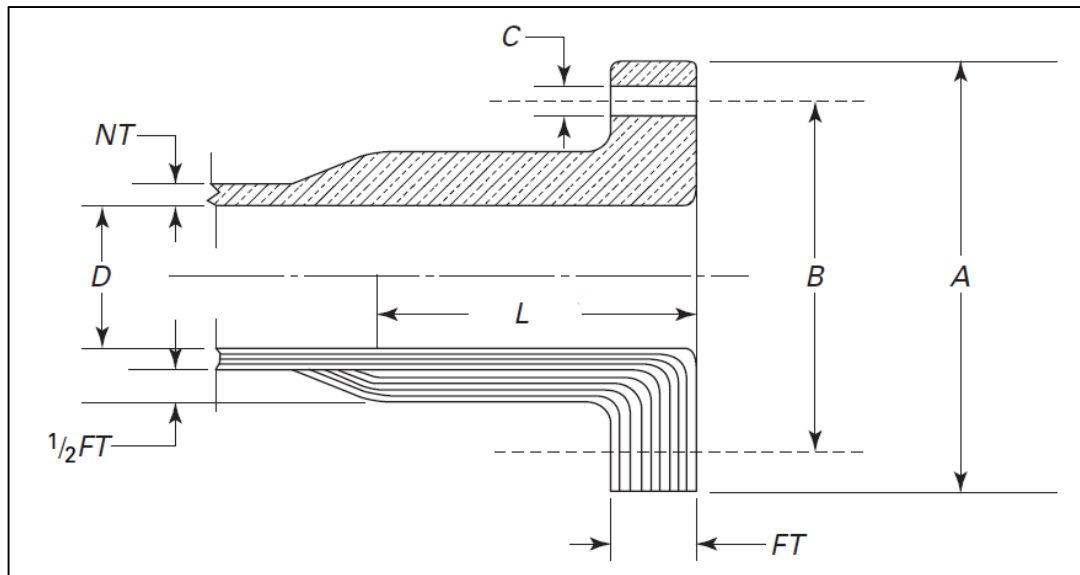
Figure 3-8 Geometry of the NPS 12 flange with the hub

Table 3-5 Dimensions of the NPS 12 flange with the hub

| | Flange NPS 12 with the hub | | | | | | | Flange and nozzle thickness, | |
| | | | | | | | | 1.034 MPa, 150 Psi | |
Unit	Inside dia., D	Outside dia., A	Bolt circle, B	Bolt hole dia., C	Dia. spot facing	Bolts size dia.	No. of bolts	FT	NT
mm	304.8	482.6	431.8	25.4	57.1	22.2	12	47.6	16.9
in	12	19	17	1	2 ¼	⅞	12	1 ⅞	⅔
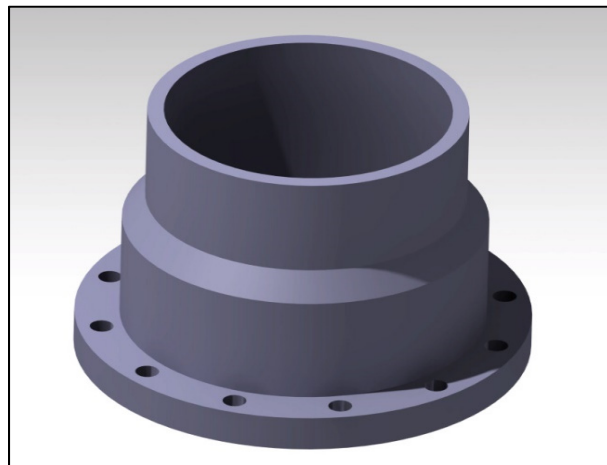
Figure 3-9 Geometry of FRP flange with the
hub modeled in Catia
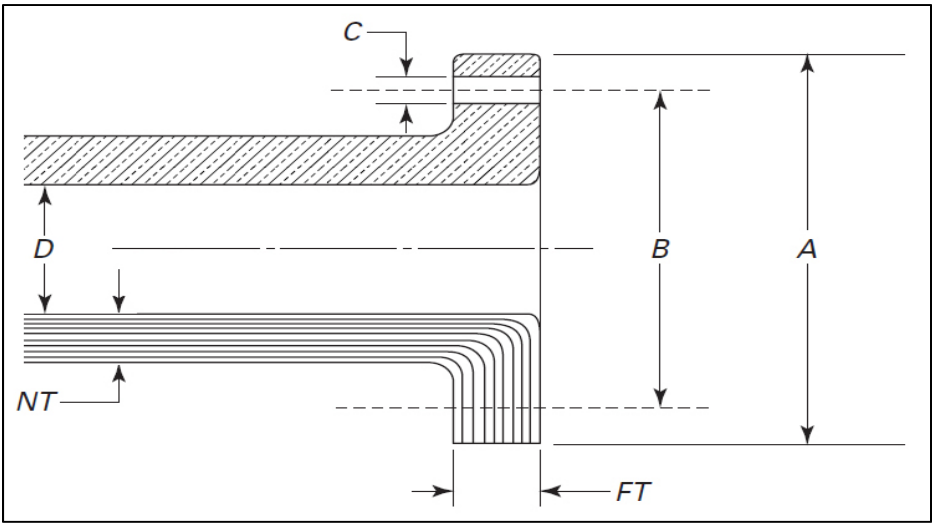
Figure 3-10 Geometry of the NPS 12 flange without the hub

Table 3-6 Dimensions of the NPS 12 flange without the hub

	Flange NPS 12 without the hub							Flange and nozzle thickness,	
								0.345 MPa, 50 Psi	
Unit	Inside dia., D	Outside dia., A	Bolt circle, B	Bolt hole dia., C	Dia. spot facing	Bolts size dia.	No. of bolts	FT	NT
mm	300	480	425	19	57.1	16	12	30	17
In	11.8	18.9	16.7	0.75	2.2	0.6	12	1.18	0.67
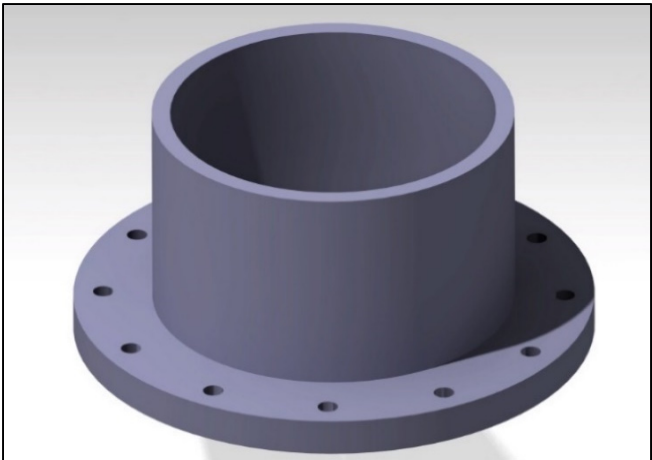
Figure 3-11 Geometry of FRP flange without the
hub modeled in Catia

3.5.1.2 Lamina properties

FRP flanges that are used in this study are made out of laminates of E-glass fibers as a reinforcement and vinyl-ester as a resin. There are two types of laminates for this composite:

1. Chopped strand mat: This laminate is fabricated by mixing the fibers randomly with the resin. The volume of the fiber in this laminate is 35% and the thickness of this ply is 1 mm.

2. Woven roving: Continuous filaments of fiber wetted with the specified resin applied are wound in a systematic manner under controlled tension and cured on a mandrel or other supporting structure This laminate is fabricated by interlacing the wetted fibers in a resin, passing in one direction with other fibers at a 90-degree angle to them. The volume of the fiber in this laminate is about 60% and the thickness of this ply is 0.9 mm.

The elastic, mechanical and physical properties of mat and woven roving plies are given by Hoa (1991) listed in Table 3.7.

In order to compare the analytical and numerical results of FRP bolted flange joints, the flange is divided into three major parts (ring, hub, and shell) and subsequently, each part has a different thickness and arrangement of plies but they are all composed of a mat and woven roving laminates. It is worth noting that in reality, FRP flange laminates are hand layered-up with midplane symmetry as shown in figure 3.12.

Table 3-7 Mechanical, physical and elastic properties of the laminates

Properties	M (Chopped strand Mat)	R (Woven roving)	C (C-Glass veil)	Unit
Fiber volume	30-35	50-60	10	%
Density	1.38	1.71	1.25	g/cm^3
Thickness	0.97	0.99	0.61	mm
Young's modulus (X direction)	7929	18791	4888	MPa
Young's modulus (Y direction)	7929	18791	4888	MPa
Shear modulus	2985	2654	1827	MPa
Poisson's ratio	0.34	0.15	0.34	
Tensile yield strength (X direction)	121	84	73	MPa
Tensile yield strength (Y direction)	121	84	73	MPa
Compressive yield strength (X direction)	95	66	42	MPa
Compressive yield strength (Y direction)	95	66	42	MPa
Shear strength	61	56	27	MPa

As mentioned previously, FRP flange is composed of three parts, ring, hub and shell, and due to different thickness, each part has a different arrangement of plies. There are two types of plies, mat and woven roving and the layer stacking sequence is symmetric for each part of the flange. The material and physical properties of the mat and the woven roving laminate are given in table 3.7. As mentioned before the thickness of the mat and woven roving layers is 0.9 mm and 1 mm respectively. In all FE models, the inner layer of the flange is installed against corrosion and because of its very small thickness, this layer is neglected in the numerical FE model.
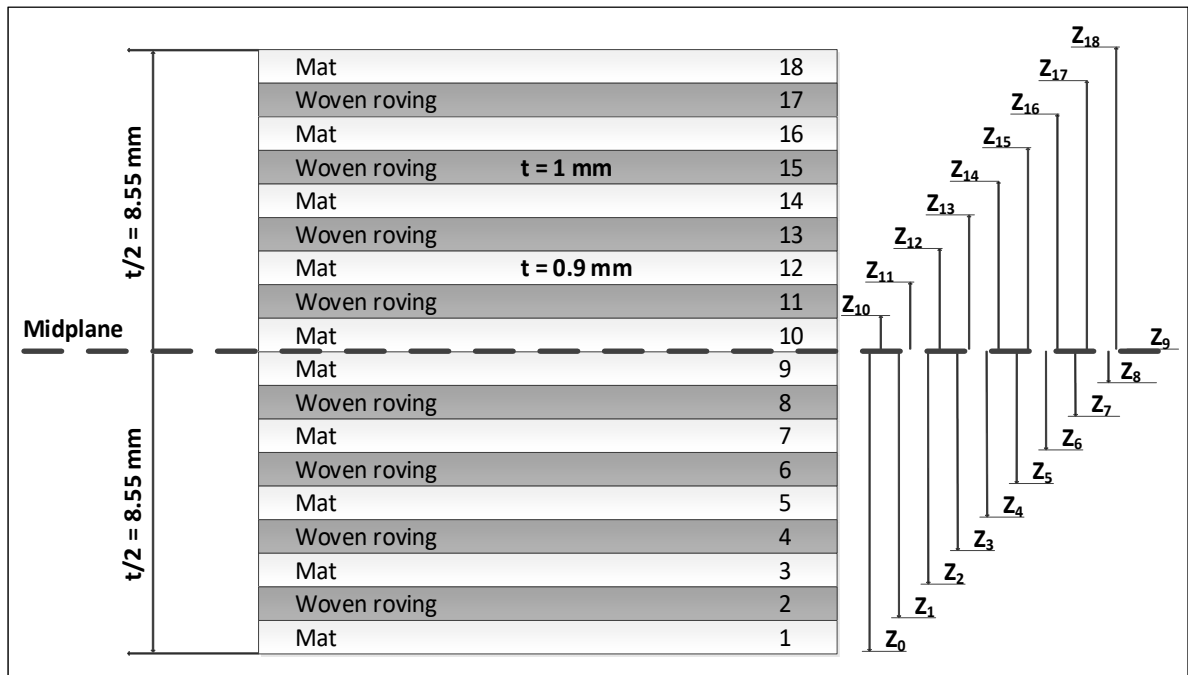
Figure 3-12 General laminate for the shell

Figure 3.12 illustrates the general laminates of the shell. The laminate of the shell consists of 18 layers and the thickness of the shell is 17.1 mm.

For FRP flanges modeled in this study, the following assumptions are made:

- Chopped strand mat and woven roving fabrics that are used in laminates are considered macroscopically homogeneous, elastically linear and orthotropic.

- In all interfaces and junctions, it is assumed that there is perfect adhesion and bonding between layers.
- The fibers are assumed to be evenly distributed and perfectly aligned in the woven roving layers with good adhesion in the fiber-matrix interface.

General laminate and the layer stacking sequence for the hub and ring of the NPS 12 flange with the hub are depicted in figures 3.14 and 3.15. The number of laminas in the hub is 44 and in the ring is 50 with a total thickness of the hub and the ring is 41.8 mm and 47.5 mm respectively.
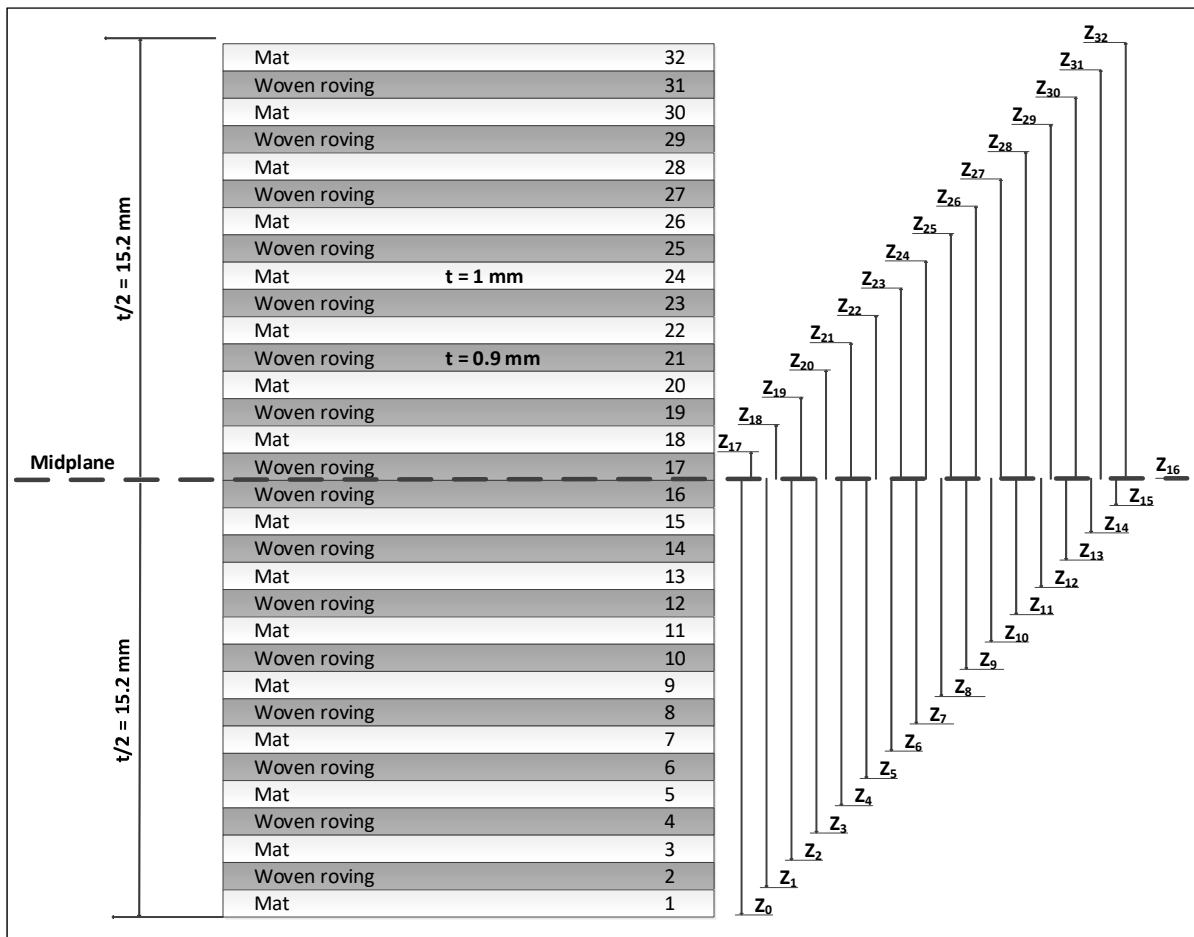
Figure 3-13 General laminate for the ring of the NPS 12 flange without the hub
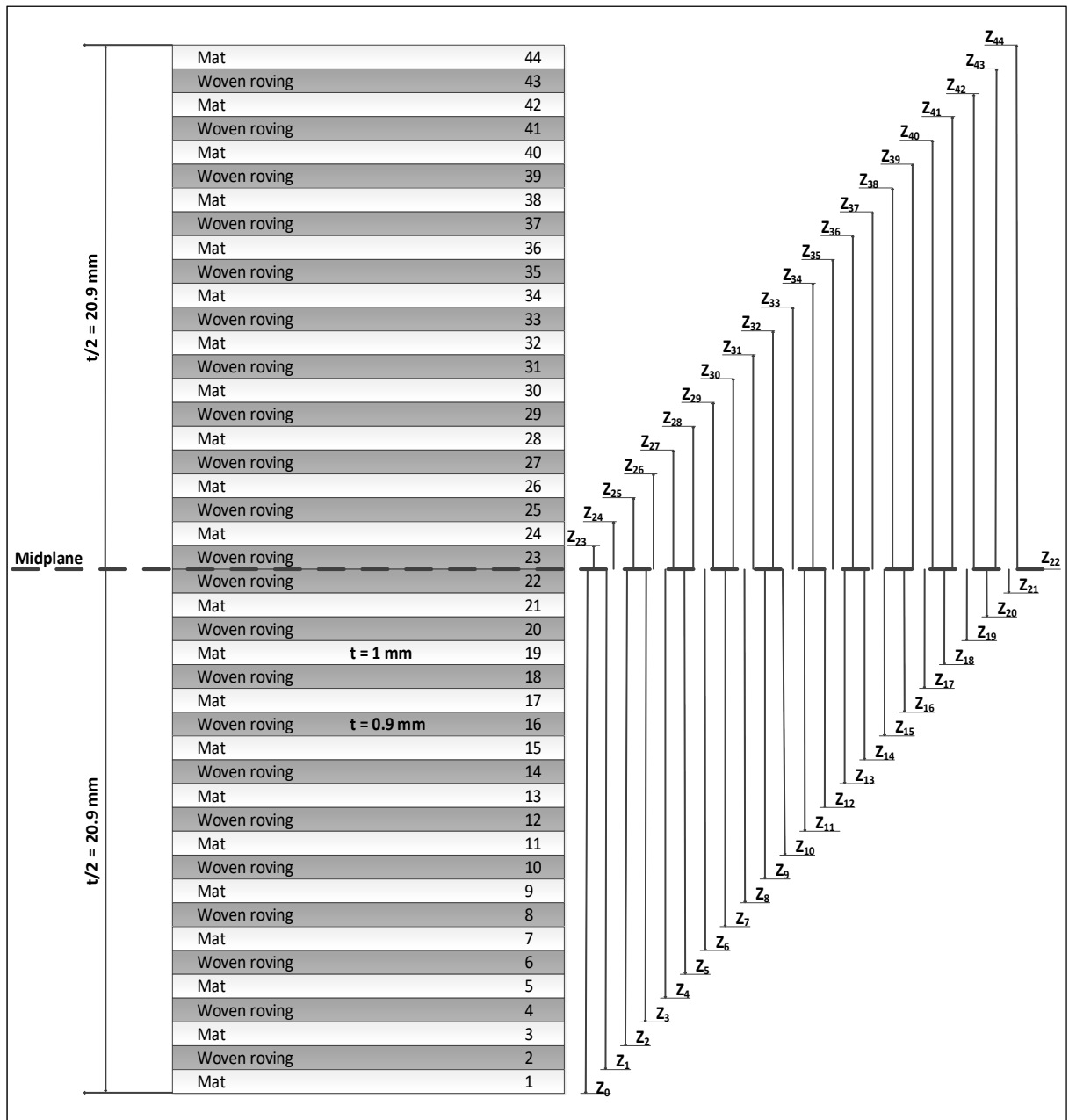
Figure 3-14 General laminate for the hub

Mat		50
Woven roving		49
Mat		48
Woven roving		47
Mat		46
Woven roving		45
Mat		44
Woven roving		43
Mat		42
Woven roving		41
Mat		40
Woven roving		39
Mat		38
Woven roving		37
Mat		36
Woven roving		35
Mat		34
Woven roving		33
Mat		32
Woven roving		31
Mat		30
Woven roving		29
Mat		28
Woven roving		27
Mat		26
Mat		25
Woven roving		24
Mat		23
Woven roving		22
Mat		21
Woven roving		20
Mat	t = 1 mm	19
Woven roving		18
Mat		17
Woven roving	t = 0.9 mm	16
Mat		15
Woven roving		14
Mat		13
Woven roving		12
Mat		11
Woven roving		10
Mat		9
Woven roving		8
Mat		7
Woven roving		6
Mat		5
Woven roving		4
Mat		3
Woven roving		2
Mat		1

$t/2 = 23.75$ mm

$t/2 = 23.75$ mm
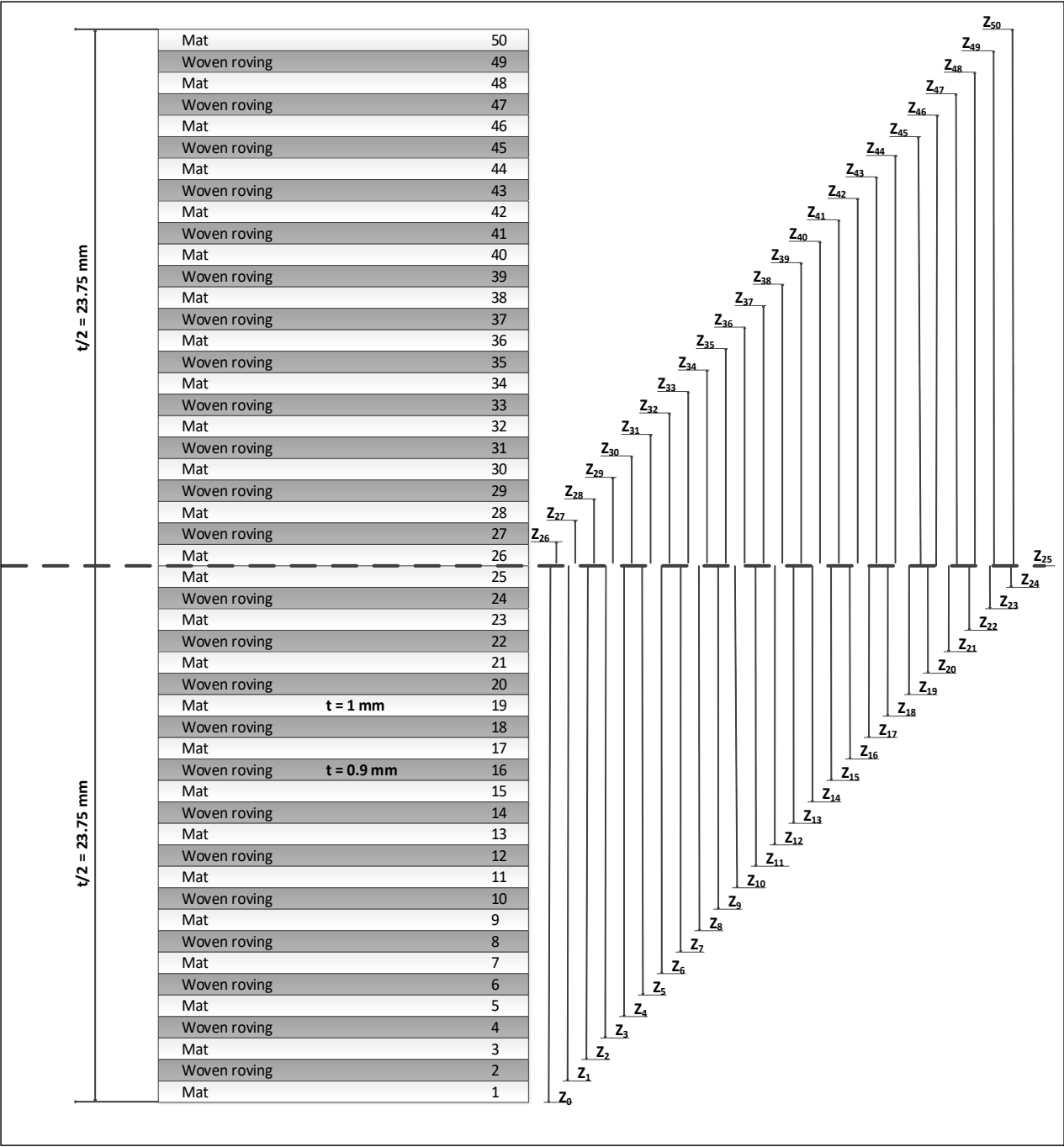
Figure 3-15 General laminate for the ring of the NPS 12 flange with the hub

3.5.1.3 Meshing and contacts

In ANSYS® Mechanical, all parts of the flange are modeled using Solid185 element which is a 3D 8-node element and exhibits quadratic displacement behavior that has three degrees of freedom per node. This type of element supports plasticity, hyper-elasticity, and large deflection. Figure 3.16 shows the mesh of the model for the NPS 12 flange without the hub.
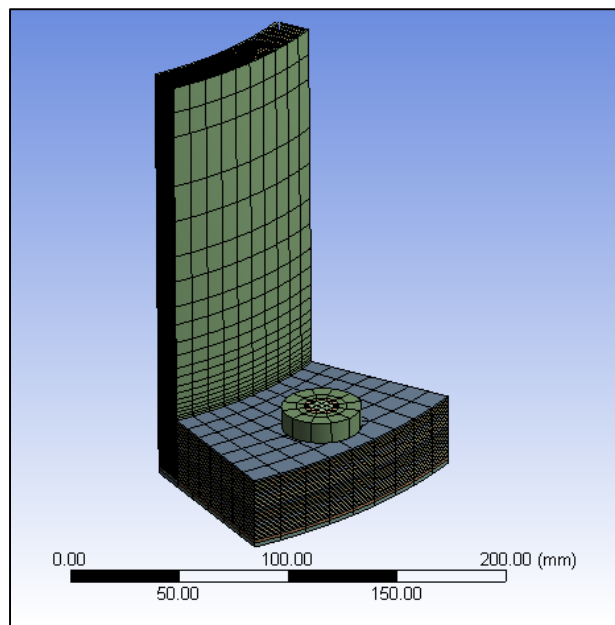
Figure 3-16 FE mesh model for NPS 12 flange

The mesh of the gasket is made with SOLID186 elements which are 3D 20-node similar elements to SOLID185. This element exhibits quadratic displacement behavior and has three degrees of freedom per node.

One of the fundamental building blocks of a good simulation to reproduce the real behavior of the bolted flange joint is employing the correct element of the contact surface in the FE model. In this model, the contact between the bolt and flange ring is to be simulated with a frictional surface having a coefficient of friction of 0.15. As to the other contact between the ring and

gasket a coefficient of friction of 0.7 is used due to the surface roughness. The contact element used in the model is CONTACT174 having eight nodes and used in conjunction 3D target interface surface elements. The element TARGE170 is employed in this case and is associated with CONTACT174 elements.

As mentioned before in section 3.2.1 the bolt load is applied through the command "pretension". In the numerical model, the element PRETS179 is involved in the application of bolt load pretension. This type of element can be used in a 2D or 3D model and has one degree of freedom that can be defined in a direction specified by the pretension force.

In the second step, the pressure on the inside surface of the flange was applied while the bolt pretention varies as a result of the flexibility of the bolted joint. During the pressurization phase, the pretension bolt load is locked to maintain the torque load on the bolts. The SURF154 elements used to simulate the hydrostatic end effect and they are defined by 8 nodes and are specific to surface in 3D FE models.
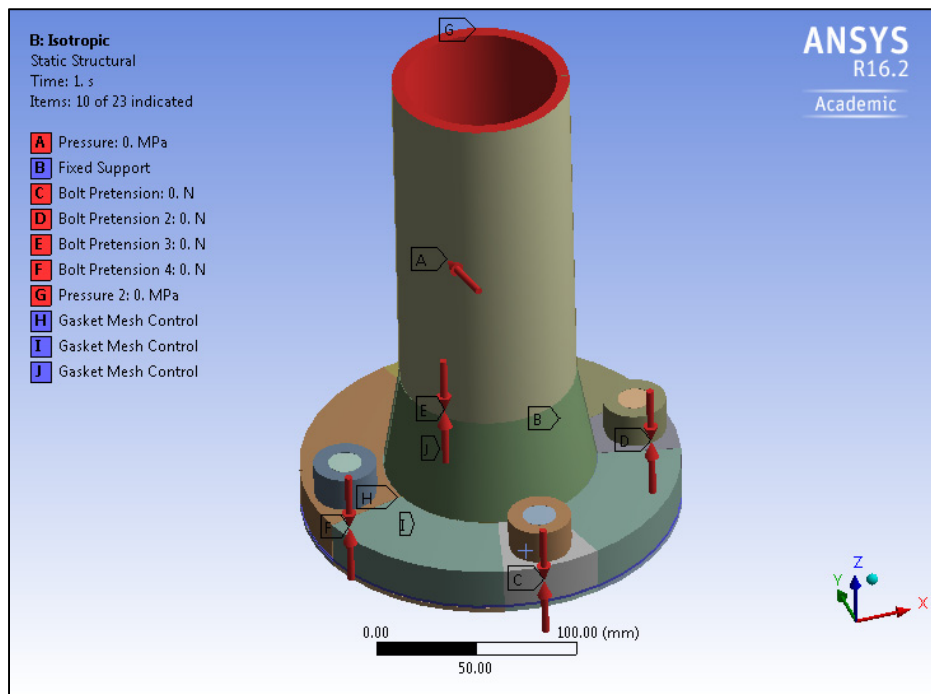

Figure 3-17 Finite element model of the isotropic NPS 3 FRP flange

3.5.2   Finite element model for the flange with NPS 3 class 150

Two different finite element models were developed to study the behavior of the NPS 3 class 150 FRP flange joint under the software ANSYS® Mechanical.

The two FE models considered in the study are:

1-   FE model with an isotropic behavior:
      In this model, the material behavior of FRP flange is assumed to be linear elastic with an equivalent isotropic elastic modulus equal to 13927 MPa. The corresponding linear elastic finite element model of the isotropic FRP flange is depicted in Figure. 3.17.

2-   FE model with an anisotropic behavior:
      This model was developed to introduce the real anisotropic behavior of FRP flange. This model is basically the same as the previous model. According to the manufacturer drawings the material properties of the composite are listed below:
      E_L = 13445 MPa
      E_T = 14686 MPa.
      $v_L = v_T = 0.28$

G_{LT} = 25442 MPa.

where E_L and E_T are the young's moduli in longitudinal and tangential directions, v_L and v_T are the Poisson's ratio in longitudinal and tangential directions, G_{LT} is the shear moduli in L-T plane.

   3.5.2.1 Geometry of the flange

Figure 3.18 and Table 3.8 illustrates the geometry and dimensions of the NPS 3 FRP flange with the hub. As mentioned earlier, the flanged connection is assumed to be sufficiently far from the end enclosures of the vessel, such that the longitudinal and bending has a local effect.

Table 3-8 Geometry of the NPS 3 flange (ZCL Composite Co.)

| | Flange NPS 3 | | | | | | Flange and nozzle thickness, | | | |
| | | | | | | | 1.034 MPa, 150 Psi | | | |
Unit	Inside dia., D	Outside dia., A	Bolt circle, B	Bolt hole dia.	Dia. spot facing	Bolts size dia.	No. of bolts	FT	Hub TH.	Hub HT.	NT
mm	76.2	190.5	152.4	19.05	36.58	15.87	4	20.65	15.42	54.33	6.35
in	3	7.5	6	0.75	1.44	0.625	4	0.813	0.607	2.139	0.250

The flange dimensions that are listed in Table 3.8 were obtained from ZCL Dualam Inc. composite flange manufacturing company.
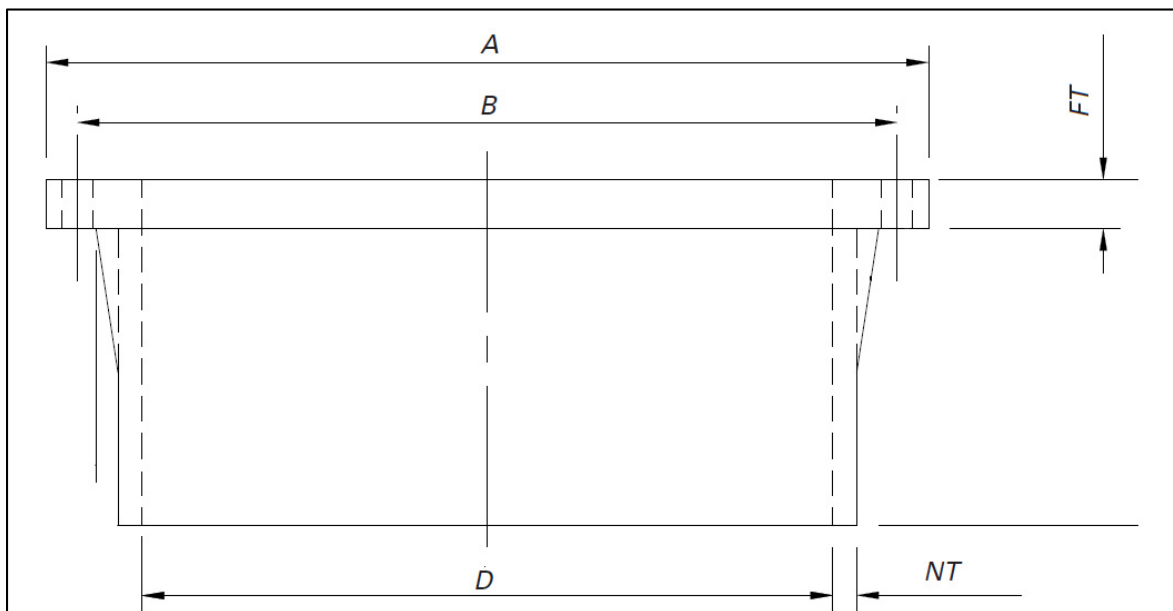

Figure 3-18 Geometry of the NPS 3 flange with the hub

Similar to the FE model of NPS 12 FRP flange, the geometry of the NPS 3 flange is designed in Catia and transferred to ANSYS using IGES file format. Figure 3.19 depicts the designed NPS 3 FRP flange in Catia and ANSYS workbench.
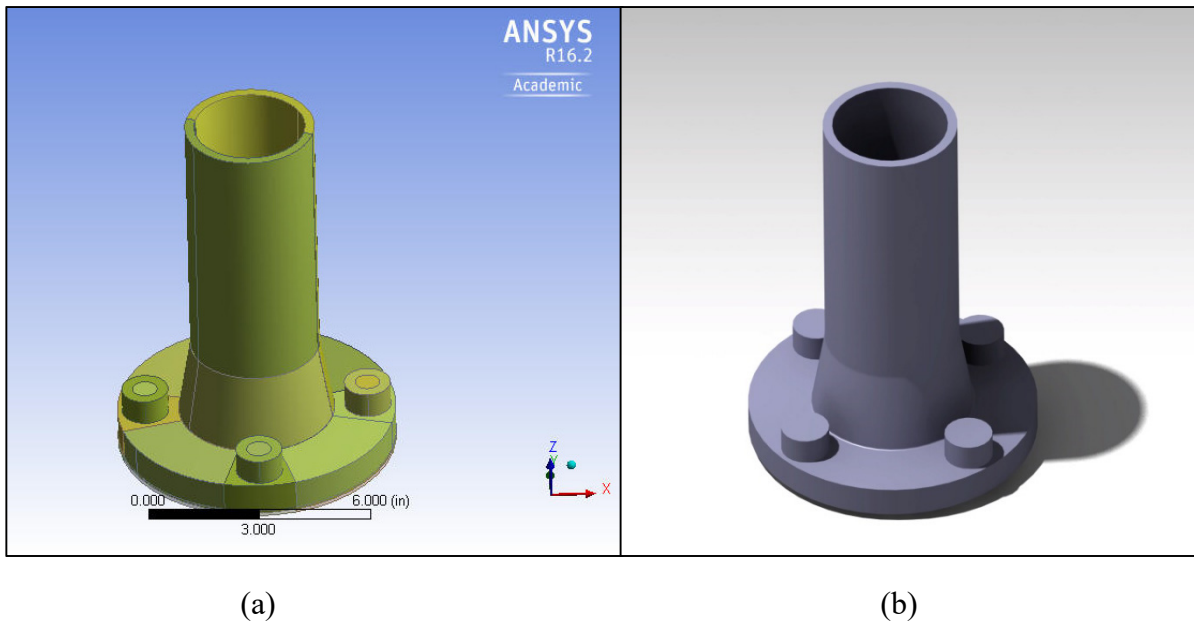
(a)   (b)

Figure 3-19 Geometry of the NPS 3 FRP bolted flange joint in (a) ANSYS and (b) Catia

3.5.2.2 Mesh of flange and contacts

The FE mesh model of the NPS 3 FRP bolted flanged joint is shown in figure 3.20. The elements used in these models are the same as those used in 3.5.1.4. The flange is modeled using Solid185 elements and the gasket is modelled using Solid186 elements. The contact elements used between flange ring and bolt head and gasket are CONTA174 associated with TARGE170 elements. The element PRETS179 and SURF154 are used to apply the bolt load pretension and hydrostatic end effect.

3.5.3   Finite shell element model ANSYS Composite PrepPost (ACP)

This model is composed of layered composites represented by shell elements. In this model, the mesh is generated using ANSYS Workbench while the composite layup with fiber orientation and material details were defined in ANSYS Composite PrepPost (ACP). ANSYS Composite PrepPost is an add-on module dedicated to the modeling of layered composite structures and provides all necessary functionalities for the analysis of layered composite

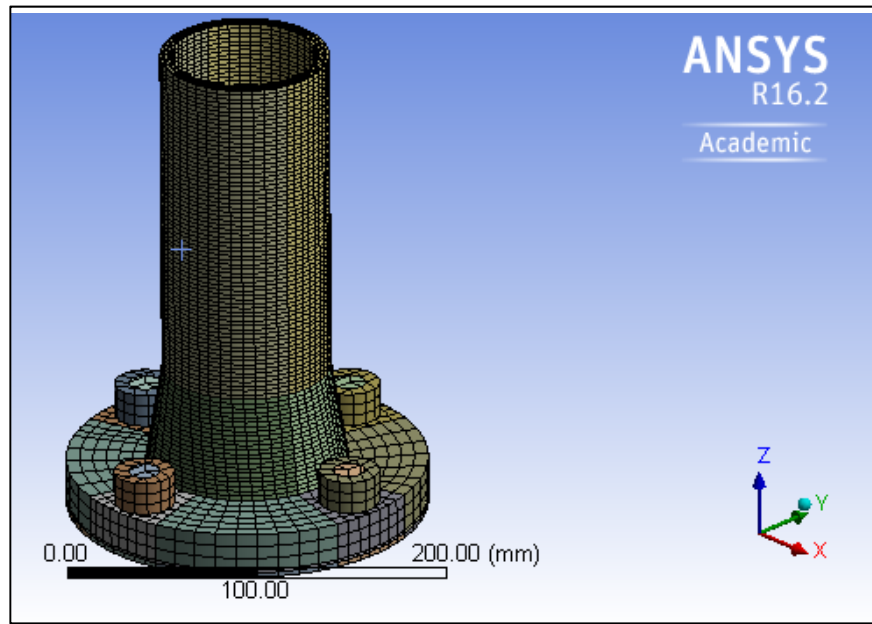structures. In order to build a solid model out of shell elements in ACP, the extrusion method was used.

Figure 3-20 FE Mesh model for the NPS 3 FRP bolted flanged joint

In this model, it is necessary to divide the bolted flange joint into two parts. The first part is the flange made from composite material and the rest is the group of parts like the bolts and gasket that are made from none-composite materials. The flange is defined in ANSYS ACP which is linked to the other parts in ANSYS Workbench. In ANSYS ACP, first, the composite fabrics including materials and the thickness of the layers as well as the assembly and element orientation of laminate are defined. Then, the ply sequence for the groups of elements in the composite is defined. Figure 3.21 shows the structure of the numerical model in ANSYS Composite PrepPost (ACP).

As shown in figure 3.21, in part B or ACP (Pre), the geometry of the flange, as well as the material properties of the laminas and the laminate arrangement and orientation of the flange, are defined. The non-composite parts such as bolts and gasket are modeled in parts D (Geometry) and E (Mechanical model). Then, by connecting parts B and E, the final model is

generated in part F (Static structural). Finite element model for NPS 3 FRP bolted flange joint in ANSYS ACP is illustrated as an example in figure 3.22.
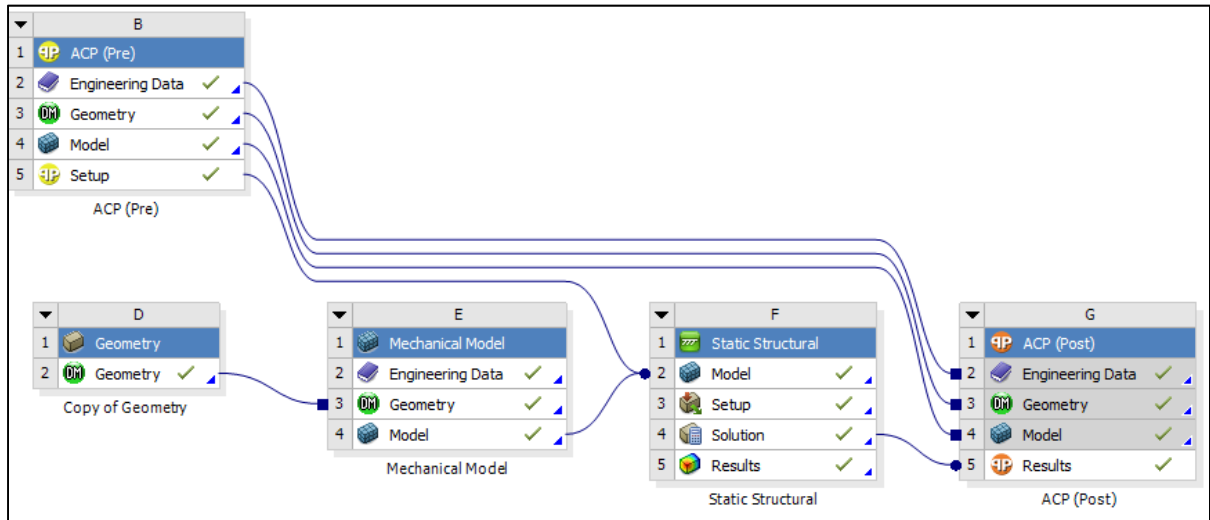

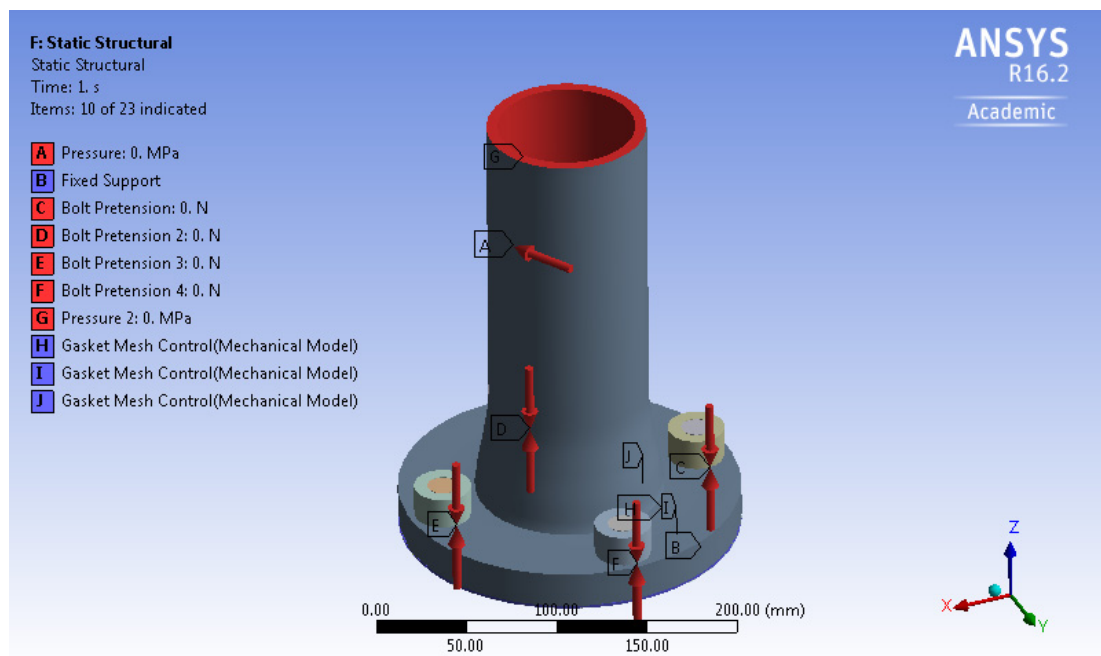Figure 3-21 Structure of the numerical model in ANSYS Composite PrepPost (ACP)

Figure 3-22 Finite element model for NPS 3 FRP bolted flange joint in ANSYS ACP

3.5.3.1 Lamina properties

There is three types of laminas used in this composite. The elastic, mechanical and physical properties of M for Chopped strand Mat, R for Woven roving and C for C-Glass veil are listed in table 3.7. The properties of Chopped strand Mat and Woven roving laminas are explained in details in 3.5.1.2.

The third material used in FRP flange composite is C-Glass veil which consists of fibers to reinforce plies and are resistant to corrosion. Thus, because of the high corrosion resistance, this type of ply is installed on the inside or outside surface of the composite flange that is in contact with the corrosive environment to protect the composite flange from chemical damages. The thickness of this ply is very small and has a very low proportion of fibers that is about 10% of carbon. According to Conlinsk, P. (2008), C-Glass veil is followed by two or three layers of chopped strand mat ply to increase the corrosion resistance of the flange.

3.5.3.1 Flange laminates

The sequence of the layers used in the construction of the NPS 3 FRP flange laminate according to the company (ZCL Dualam Inc.) is as follows:

Flange face sequence: CMM/2(MRMRM)/3(MRM);
Hub sequence: CMM/MRMM/3(MRM);
Shell sequence: CMM/MRMM.

where C = C-Glass veil, M = Chopped strand mat, and R = Woven roving

It is worth noting that each layer has different material properties in three directions, therefore, the final result is a flange with anisotropy and multilayered composite behavior. The general laminate layouts of all parts of the NPS 3 FRP flange are shown in figures 3.23 to 3.25. The number of plies in the ring is 22 with a thickness of 20.65 mm, the number of plies in the hub is 16 with a thickness of 15.42 mm and the number of plies in the shell is 7 with a thickness of 6.34 mm. Figure 3.25 illustrates FRP flange laminate as modeled in ANSYS ACP.
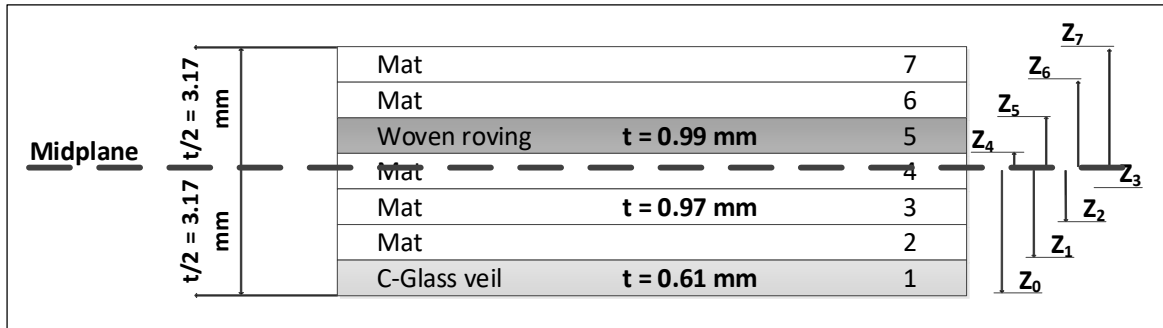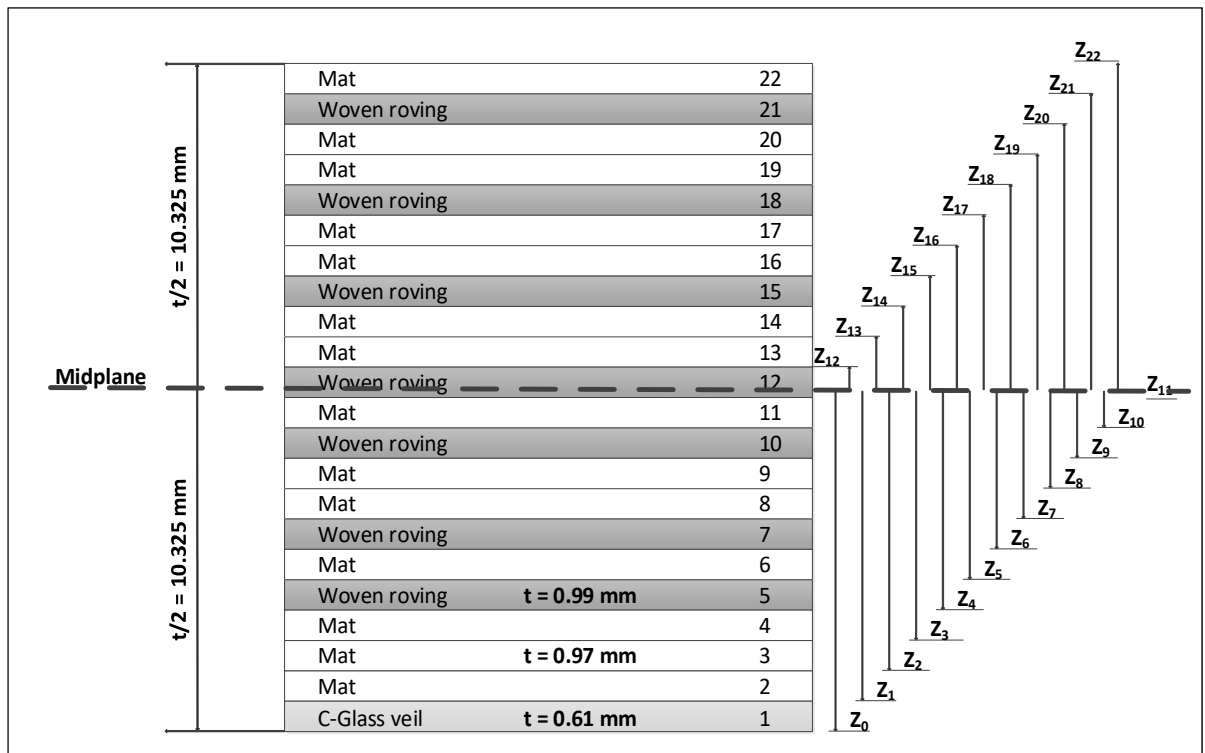
Figure 3-23 General laminate for the shell

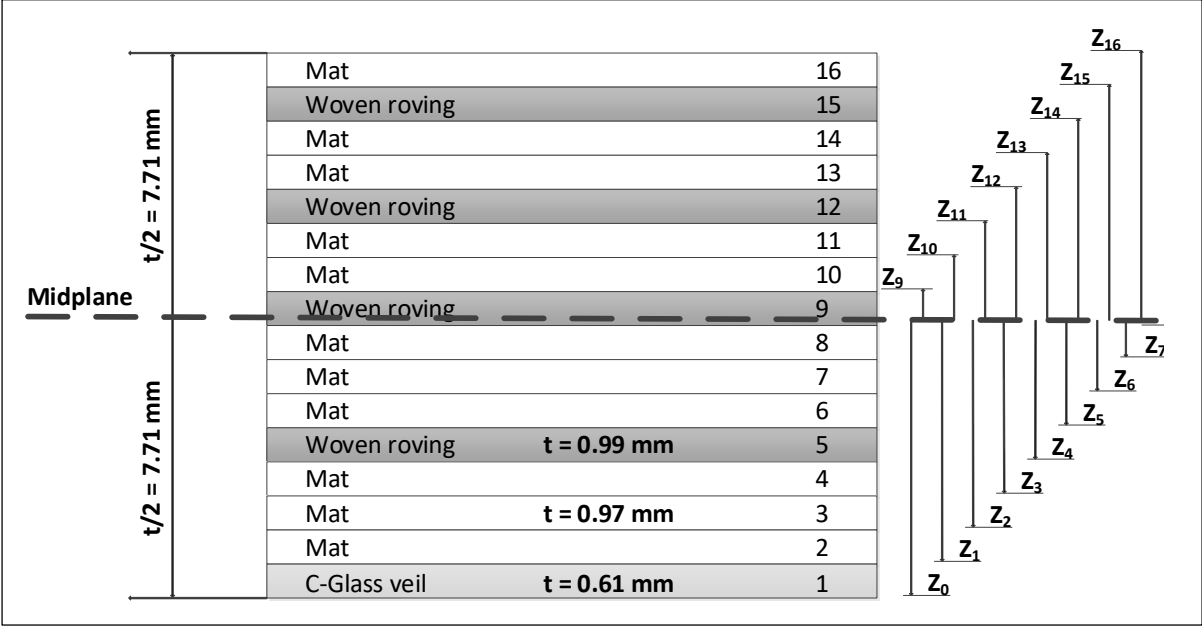Figure 3-24 General laminate for the ring

Figure 3-25 General laminate for the hub
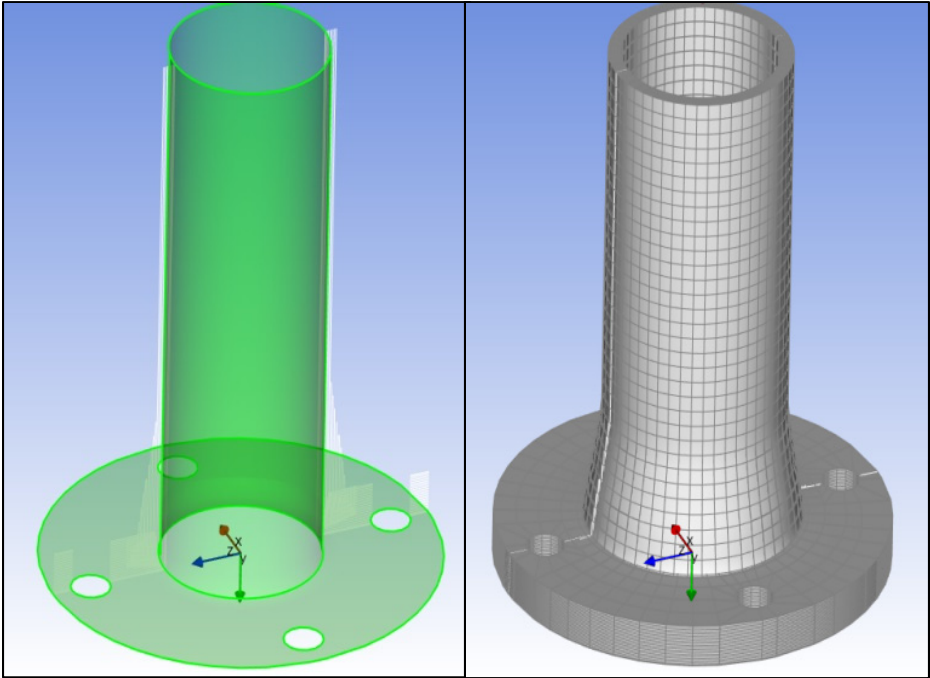
Figure 3-26 FRP flange laminate in ANSYS ACP

3.5.3.2 Geometry of the flange

The geometry of the NPS 3 FRP flange is the same as that given in 3.5.2.1. In this model, ANSYS Composite PrepPost (ACP) is used to define layered composites represented by shell elements. The extrusion method is used to build a solid model out of shell elements in ACP environment. Figure 3.27 shows the geometry of the flange model in ANSYS ACP.

As shown in figure 3.28 the model of FRP flange begins with the shell model and after transferring the model to ANSYS ACP, the laminate is modeled according to the sequence of the layers and their thickness. The geometry of bolts and gasket is then added as shown in figure 3.29. As mentioned earlier the non-composite parts of FRP bolted flange joint are modeled separately.
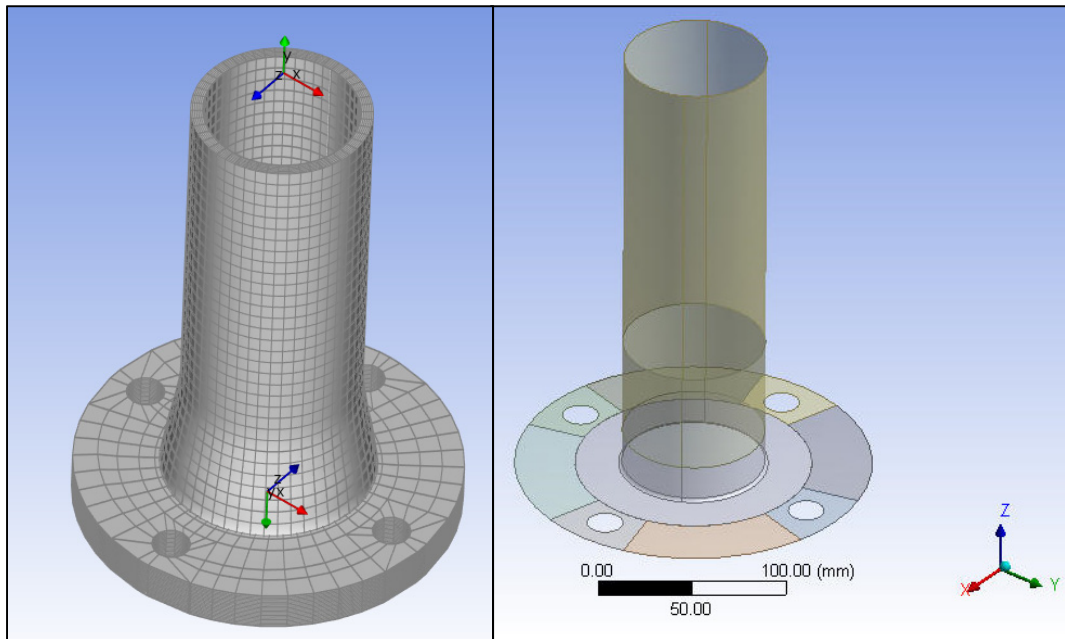
Figure 3-27 Geometry of the flange in ANSYS ACP

Figure 3-28 Geometry of the flange in ANSYS geometry
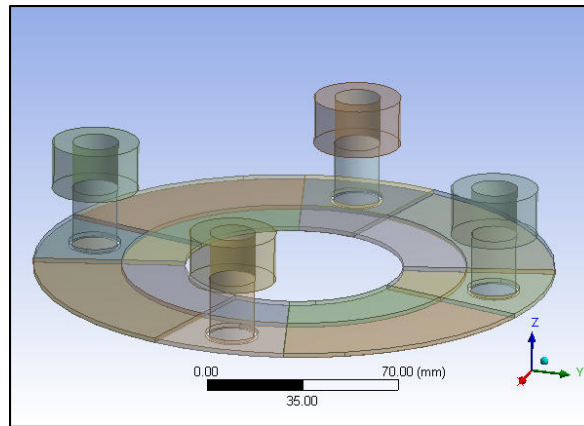
Figure 3-29 Geometry of the bolts and gasket

3.5.3.3 Meshing and contacts

The complete FE mesh of the NPS 3 FRP bolted flanged joint is shown in figures 3.30. The elements used in this model are the same as those used in 3.5.1.4. the flange is modeled with ANSYS Composite PrepPost (ACP) using a different type of element layers. Solid185 elements are used for the flange and Solid186 elements are used for the gasket. Contact elements of the type CONTACT174 associated with TARGE170 elements are employed to model the various contact surfaces between flange ring and bolt head and gasket. The element PRETS179 and SURF154 are used to apply bolt load pretension and hydrostatic end effect.

Figure 3-30 FE mesh model for the flange

Figure 3-31 FE model mesh for bolts and gasket

Figure 3-32 Final FE mesh model for the FRP bolted flange joint

CHAPTER 4

EXPERIMENTAL SET-UP

4.1 Introduction

The relevant experimental tests used to carry out on real fiber reinforced plastic bolted flanged assemblies designed according to ASME BPV Code Section X as is described in this section. An experimental investigation conducted on a well-equipped test rig is a reliable approach to evaluate the proposed numerical and analytic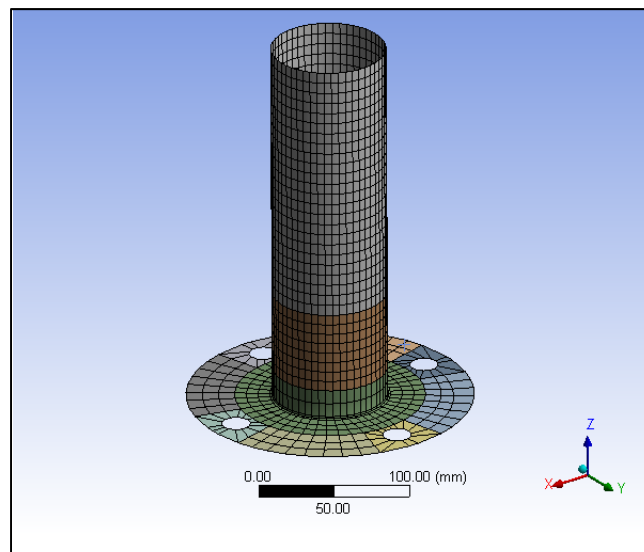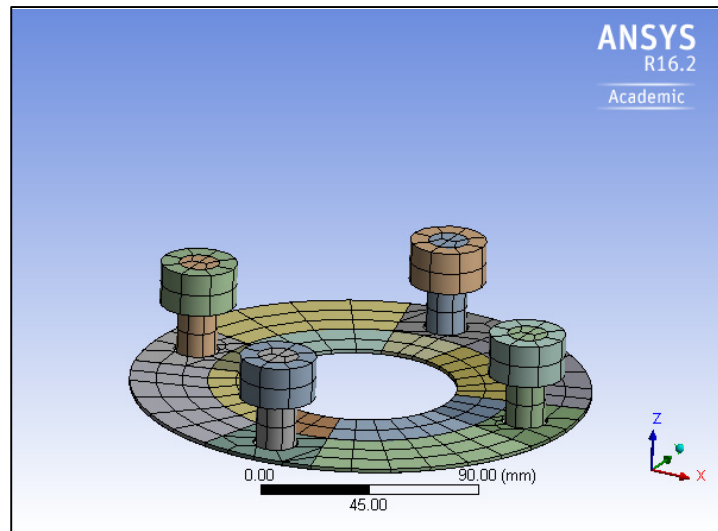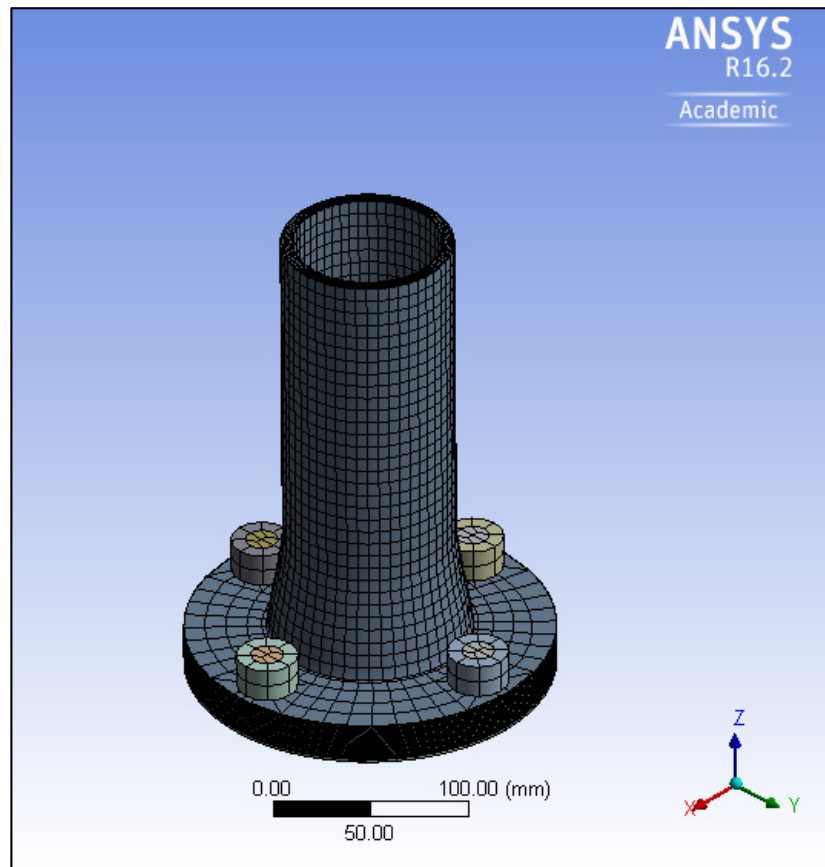al model for the NPS 3 FRP bolted flange joint. The detailed explanation of the intrigue mechanisms of the test bench used in the study of the bolted flange joint behavior with high-level instrumentation is vital.

The primary purpose of the designed experimental test stand was to measure the real behavior of the composite bolted flange joint. The existing Hot Blow Out Test Bench (HOBT) was adapted and equipped with accurate measurement devices such as strain gauges, LVDTs, thermocouples, and pressure transducers to measure the different parameters of FRP flange. This chapter elaborates the operational mechanisms of the HOBT rig and test procedure involved in this study.

4.2 Bolted flanged rig

The HOBT test rig shown in figure 4.1, was used throughout the experimental investigation. This test rig is made of ANSI B16.5 NPS 3 Class 150 FRP full-face flanges used with a 1/16 Teflon gasket. The HOBT rig was initially designed and built for the Static and Dynamic Sealing Laboratory to perform hot blowout tests of Teflon gaskets used in with a metallic raised face bolted flange joint configuration. This test rig was modified to accommodate for the analysis of FRP bolted flange joint with full-faced gasket. As depicted in figure 4.1, the general configuration of this test rig is composed of 8 parts to carry out the stress analysis validation of FRP bolted flange joint. These parts are as follows:

A. Proportional integral derivative (PID) controller;

B. Data acquisition system;

C. FRP flange with a cap;

D. Strain gauges attached to the flange surface;

E. Thermocouples;

F. Bolt load measurement system;

G.   Pressurization system;

H. Control panel of the pressurization system and leak detection.

Figure 4-1 General configuration of HOBT test rig
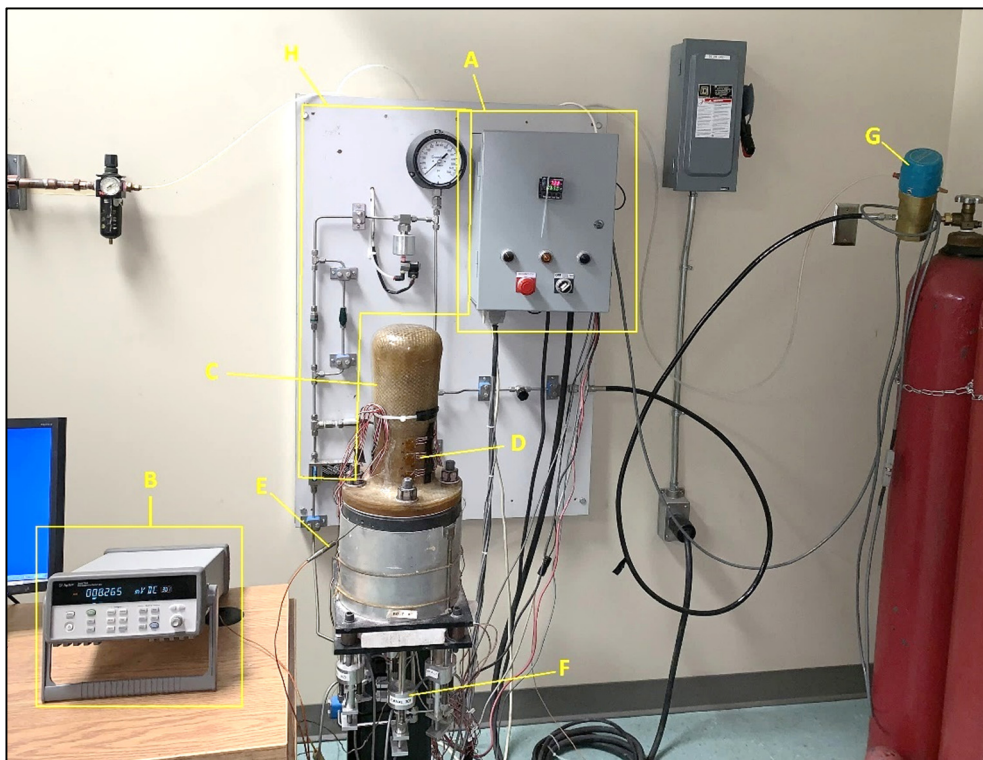
The bottom flange of the rig is bolted to a solid shaft core that is welded to a supporting base in the form of a pedestal. As shown in fig 4.2 a 2000-Watt cartridge heater is inserted into the metal core to heat up the entire fixture from the inside surface to the outside surface of the flange. There are four thermocouples on the HOBT test rig one of which is connected to a

proportional integral derivative (PID) controller which continuously monitors and controls the temperature. In order to measure the temperature lag between the flange and bolts, one thermocouple is installed one of the bolts. Another thermocouple is installed in the flange to measure the flange temperature at the vicinity of the gasket. There is also a removable insulation cover to reduce heat loss to the outside boundary and provides a uniform thermal distribution to the flange. The test rig includes the flanges made of FRP flanges. The pressurization system of the test rig is designed to apply internal gas pressure of up to 3.447 MPa (500 psi). The test rig is designed in such a way that the gasket load can easily be deduced from the measured bolt load.
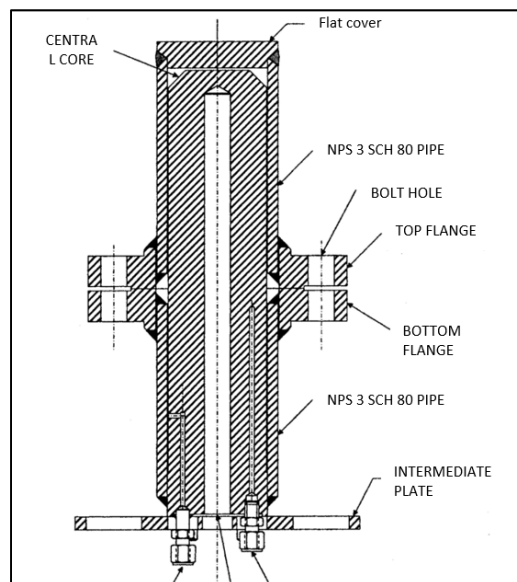
Figure 4-2 Typical cross section of
HOBT fixture (Bouzid, 2015)

4.2.1   Bolt load measurement

The bolt load measurement system known as the extensometer is shown in figure 4.3. In order to tighten and seal the lower and upper mounting flanges, four UNB 5 / 8-18 (in) ASTM A193 bolts are used. The measurement of the load through the elongation of each bolt is achieved by

the extensometer which is connected to the ceramic tube and rod. As shown in the figure, the ceramic rod is attached to the steel rod that is inserted into the drilled hole at the center of the bolt. The ceramic rods are connected to a full-bridged strain gauged beam that picks up bolt stretch through a bending mechanism. The reason for using the ceramic rods to measure the bolt load and displacements is to perform the tests at high temperatures. By applying bolt torque, the relative movement between the bolt and the steel rod inside the bolt are picked up by the ceramic rod and tube that put the beam under bending to transmit the deformation to the strain gauges and thereby obtain the bolt force.
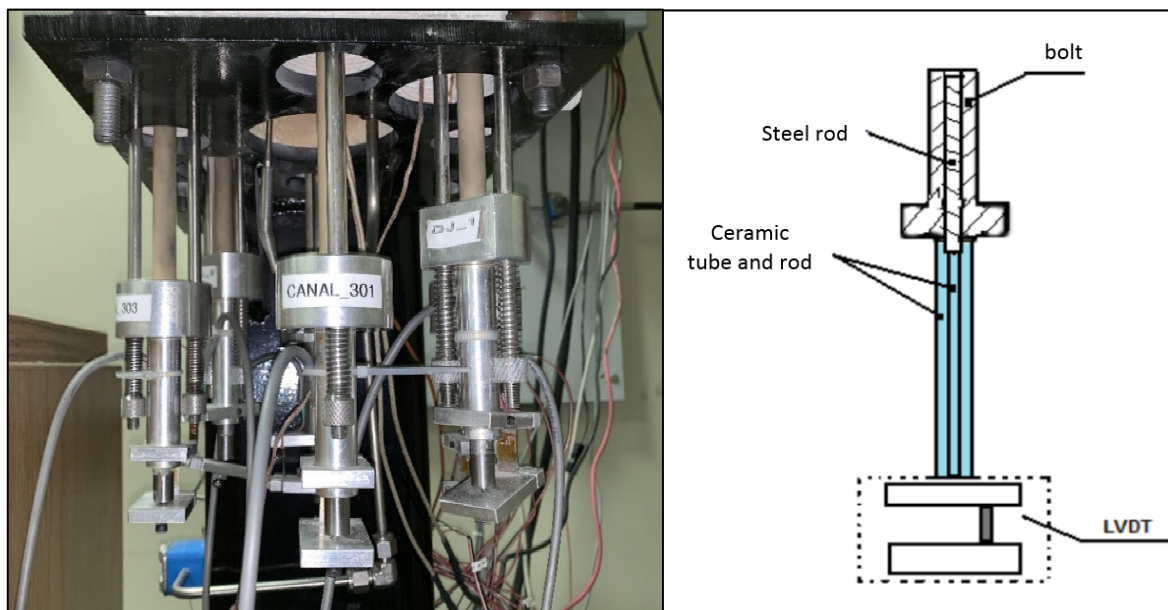
Figure 4-3 HOBT bolt load measurement system and the bolt-rod assembly

4.2.2   Displacement and rotation measurements

The measurement of the gasket displacement is achieved at two diametrally opposite position using the extensometers that have been described previously. As shown in figure 4.4 there are two ball bearings which are used to transmit the axial compression from the metallic screws to the ceramic rods.
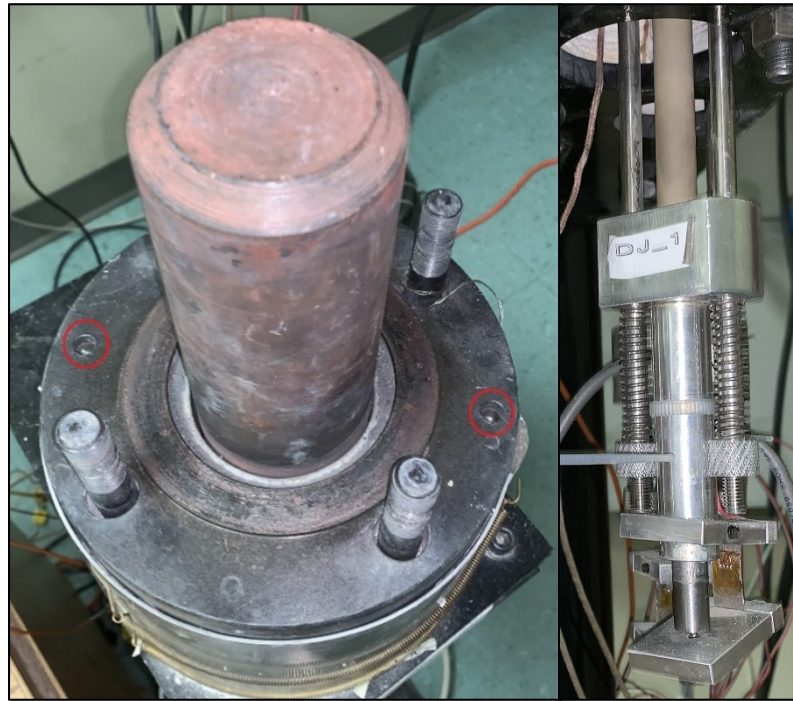
Figure 4-4 HOBT displacement measurement system

4.2.3 The data acquisition system

The bolt load, axial displacement of the gasket, temperature, strains and time are measured and recorded through Agilent 34970a data acquisition system, National Instrument and PID controller that are is connected to the computer under the LabVIEW program. Therefore, a special LabView program was developed to control and monitor the experiment parameters and record data from the various sensors. Appendix B describes the exposed panel of the LabVIEW to control the HOBT test rig and monitor data.

4.3 FRP flange set-up

To evaluate the stresses three 45° strain rosettes were loaded to the outside surface of the FRP flange near the critical position of the hub to shell junction. A close view of the strain gauges bonded to the FRP flange is shown in figure 4.6. As shown in this figure, the three strain

rosettes SG1 SG2 and SG3 are used to evaluate the longitudinal and tangential stress for comparison with the analytical and numerical models.

Figure 4.7 depicted the 45° strain rosette aligned with the x-y axes. In order to convert the longitudinal strain from each strain gage into strain expressed in the x-y coordinates, the following equation is used:

$$\varepsilon_x = \varepsilon_a \tag{4.1}$$

$$\varepsilon_y = \varepsilon_c \tag{4.2}$$

$$\varepsilon_{xy} = \varepsilon_b - \frac{\varepsilon_a + \varepsilon_c}{2} \tag{4.3}$$
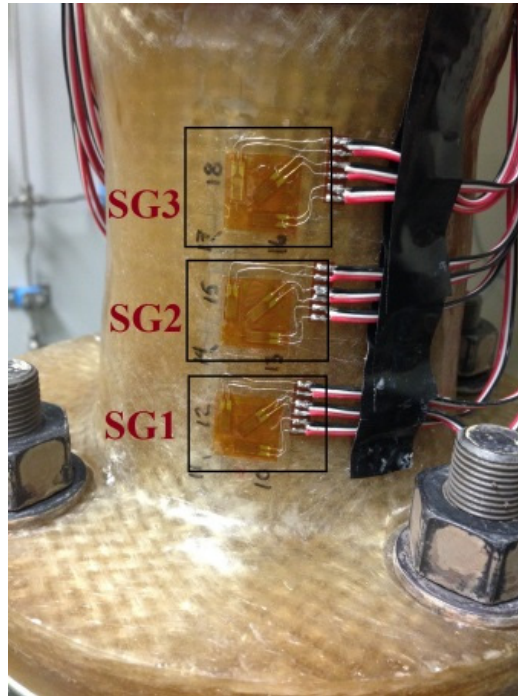
Figure 4-5 Strain gauges attached on
FRP flange
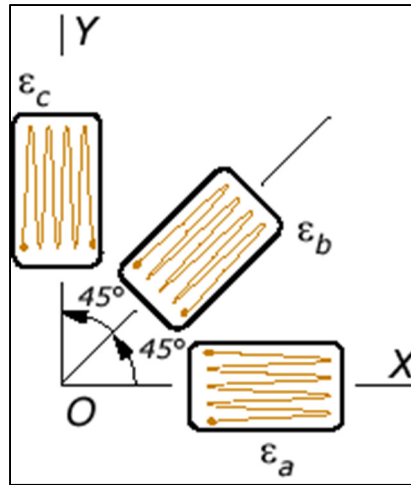
Figure 4-6 45° strain rosette
aligned with the x-y axes

4.4 Test procedure

The test procedure starts by introducing the dimension of FRP flange and gasket in the LabVIEW program along with the test conditions. A 1/16 Teflon full-face gasket is first placed on the top of the bottom flange, then the top flange is mounted on the gasket and is positioned to make sure that the two contact screws are in line with the extensometers to measure displacement. Afterward, the bolts are hand tightened. This point is considered as the zero references for bolt load and gasket displacement.

After mounting and verifying the gasket and flange position, the next step is to apply the desired compressive load by tightening the nuts with a torque wrench. An initial bolt load of 3270 lb was applied gradually on each instrumented bolt based on the guidelines provided in the ASME code section X and the manufacturer recommendation. The detailed calculation of bolt load is explained in 2.1.11. Equation 4.4 gives the total bolt load according to the recommended torque for the NPS 3 in. FRP flange.

$$T = K \times P \times D \tag{4.4}$$

where: T= tightening torque (in-lbs), K= dynamic coefficient of friction, P= total bolt load / number of bolts (lbf), D= nominal bolt diameter (in).

A special tightening procedure based on the criss-cross pattern was used to apply the required bolt load. The bolt torque sequence order followed is 1, 2, 3, 4 as illustrated in Figure 4.8. After applying the bolts loads, a gas pressure equal to 1.034 MPa (150 psi) is applied to the inside of FRP bolted flange joint through a regulator valve which is controlled by the LabView program.

All the measuring parameters such as the bolt force, the strains at selected locations of the flange hub surface, the temperature and internal pressure are continuously monitored through the data acquisition system and the LabView program. The room temperature is held constant around t 22° C during the test. It is worth noting that all measuring sensors were calibrated at this temperature.
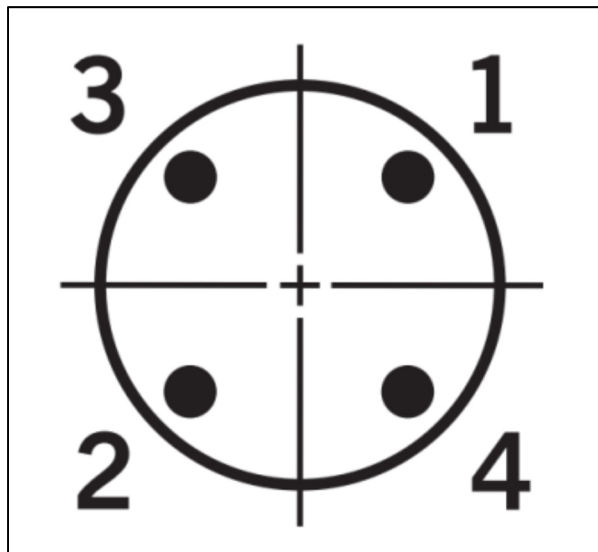

Figure 4-7 Torque sequence (SPEARS, 2014)

CHAPTER 5

RESULTS AND DISCUSSION

5.1 Introduction

In order to validate the analytical model developed for FRP bolted flange joints, the stress distribution at the outside and inside surface of the flange as well as its radial displacements are compared to the results obtained from the experimental rig and the numerical finite element model. A MATLAB program was used to code the analytical model equations that were developed in chapter 2. This program and all data used in the analytical study are available in Appendix A.

This chapter is dedicated to present by the results obtained from the analytical model, the numerical finite element model and the experiments under the two operating conditions of bolt-up (pre-tightening) and pressurization (operating). It treats the three different types of flanges namely the NPS 3 FRP flange class 150, the NPS 12 FRP flange class 50 without the hub and the NPS 12 FRP flange class 150 with the hub. In addition, a comprehensive analysis, a comparison and a discussion of the results are provided.

5.2 Results for the NPS 3 FRP flange

In this part, the experimental and analytical results of the NPS 3 FRP flange are presented and compared to the numerical results obtained with the three FE models of FRP flange joints with three different approaches; isotropy, anisotropy and shell element anisotropy composite using ANSYS ACP. The analytical results were obtained using the MATLAB program as indicated previously. It should be noted that the experimental results are limited to the stresses related to the outside surface of the flange as the stresses at the internal surfaces could not be measured due to the difficulty in getting the wires out of the flange when the latter was pressurized.

5.2.1   Flange stresses

In figures 5-1 to 5-4, the longitudinal and tangential stress distributions at bolt-up are shown. Each graph shows five curves; three curves obtained from the different FE models and two other curves representing the experimental and analytical results. As mentioned before, the stresses at the internal surfaces could not be measured during the experimental testing however theses stresses are shown in figures 5-2 and 5-4 for the other methods. A similar trend of the distribution of stress along the hub and cylinder between the FE models, analytical model and the experimental result is observed. The anisotropic FE model results are very close to the analytical results and experimental data.
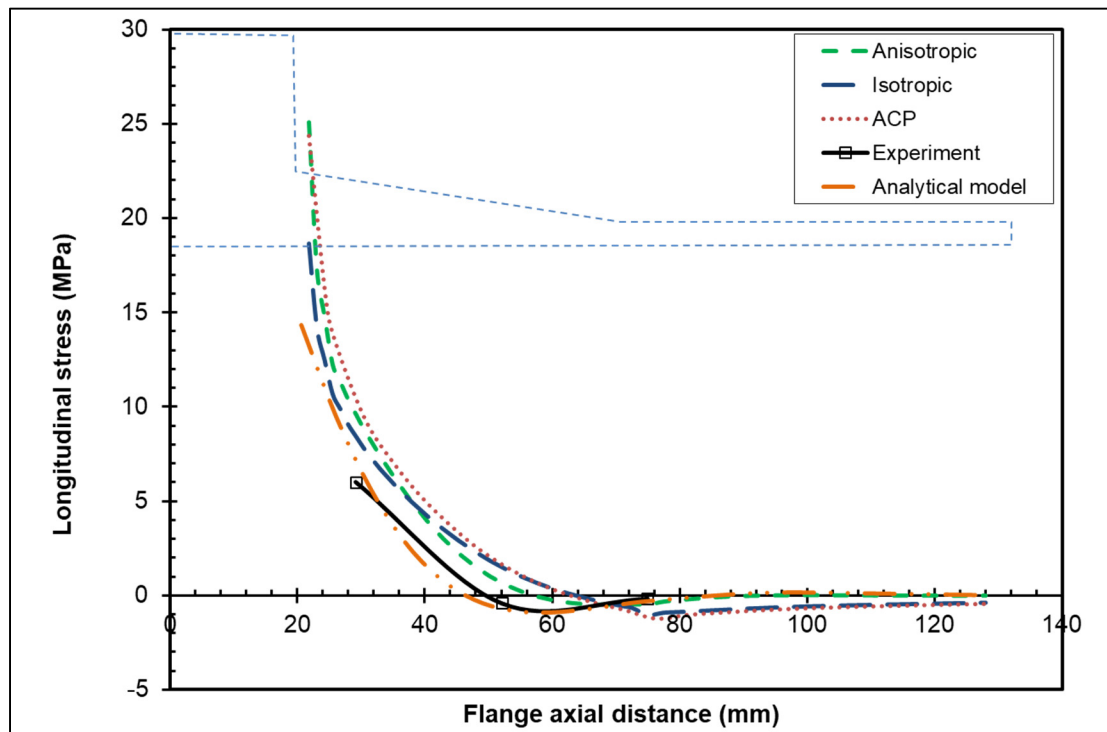
Figure 5-1 Longitudinal stress distribution at the outside flange surface during bolt-up

The graphs indicate that the results of the stress distribution at the outside surface of the flange obtained from the analytical model, experimental test and the anisotropic model are in good agreement with each other. Due to the stress concentration at the hub to flange ring junction, there is a significant difference with the average around 46% between ACP model and

analytical model. As anticipated like metallic bolted joints at bolt-up, the stresses in the cylindrical part of the FRP bolted joints far away from the hub and ring junction due to the lack of the inside pressure are nil.

The longitudinal and tangential stress distribution at 1.345 MPa inside pressure are shown in figures 5-5 to 5-9. In this case, the distributions of the longitudinal and tangential stresses at the outside surface of the flange during operation (figures 5-5 and 5-7) show a good agreement between the FE model, the analytical model, and the experimental data. A similar trend of the distribution of longitudinal and tangential stresses at the inside surface of the flange between the FE models are observed as indicated in figures 5-6 and 5-8. The graphs show that the FE anisotropic material model is more representative and the results are closer to the experimental data, as the difference observed between the two is less than 6%.
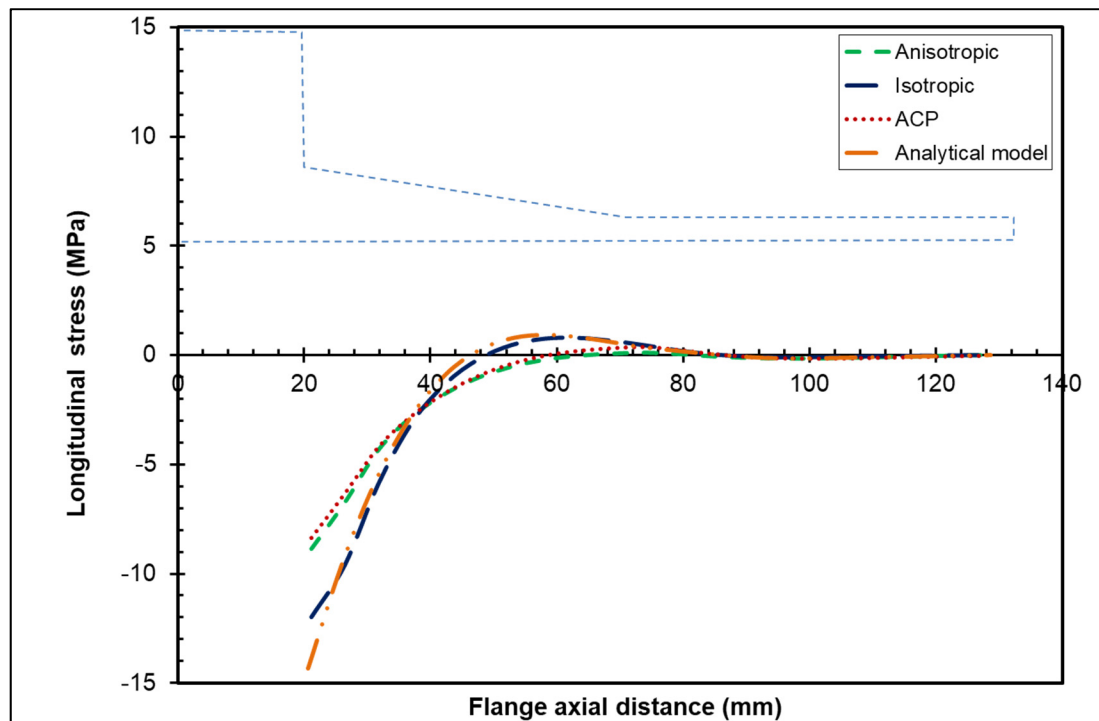

Figure 5-2 Longitudinal stress distribution at the inside flange surface during bolt-up

Figure 5-3 Tangential stress distribution at the outside flange surface during bolt-up

Figure 5-4 Tangential stress distribution at the inside flange surface during bolt-up

In spite of the fact that the anisotropic and ACP model are in better agreement with the analytical and experimental result compared to isotropic model due to the high-stress concentration at the hub and flange ring junction, it is difficult to make a judgment at this location and such a study is out of the scope of this work. In addition, the difference observed at the ring and hub junction is related to the laminate junctions that realistically cannot be duplicated either by the analytical model or by the ANSYS ACP PrepPost model. It can be noted that in the ACP model, the connection between the hub laminate and ring laminate is difficult to model exactly like the real FRP flange. Consequently, some discrepancies are observed between the results obtained from the ACP model and the other FE models. In fact, the ACP model of the composite flange is not precise as the difficulty to define the exact number of layers used for each flange part, the angle of the fibers in composite and the exact material properties in the different directions of the composite. It is worth noting that because the FRP flange manufacturing processes are hand made and not automated and the manufacturing technique varies from one composite flange size to the other, it is difficult to have defined the exact material properties in the various directions of the flange.
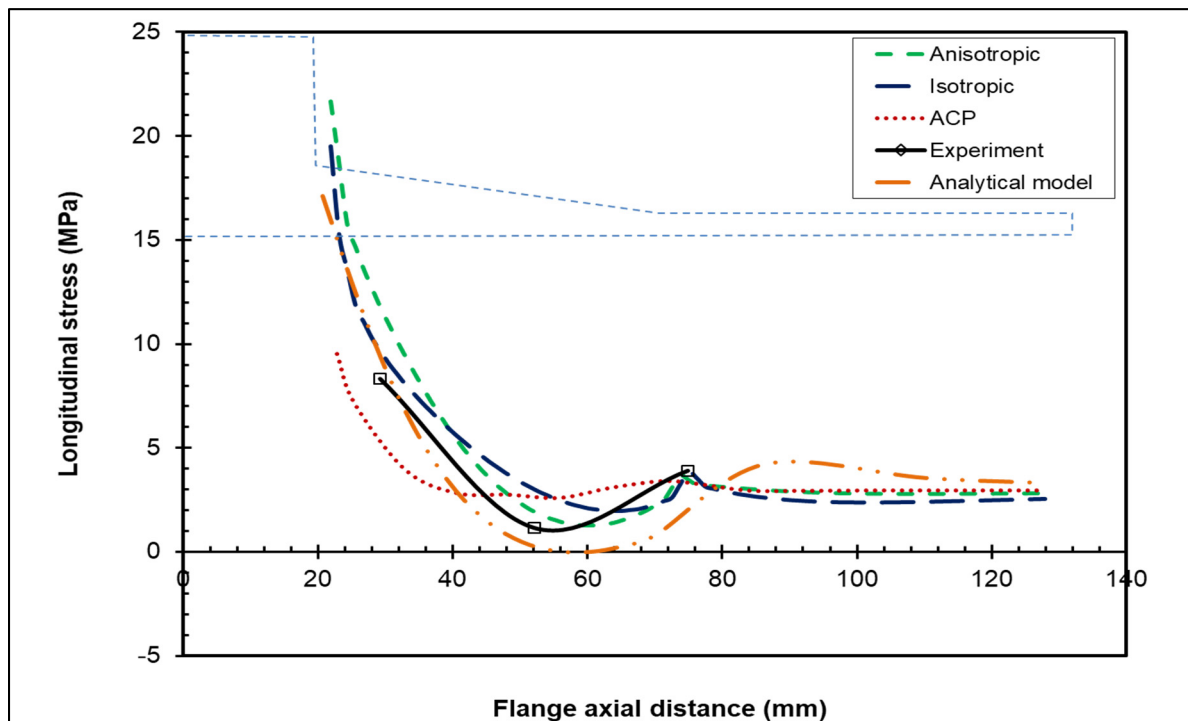
Figure 5-5 Longitudinal stress distribution at the outside flange surface during pressurization
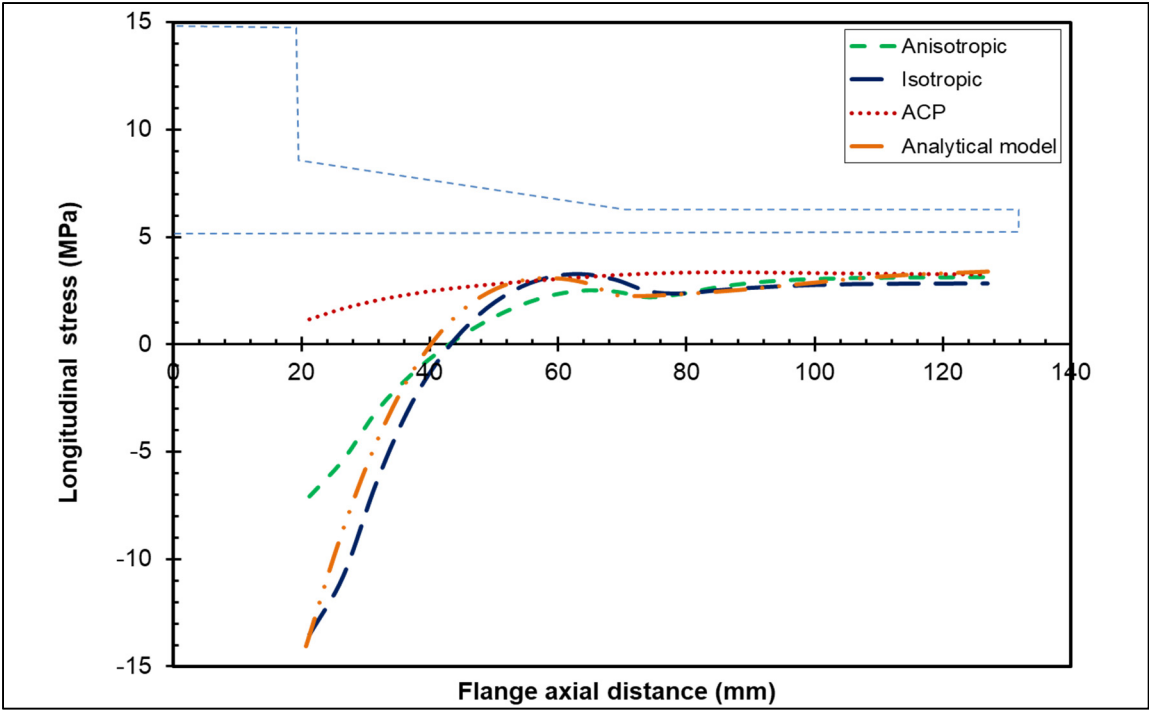
Figure 5-6 Longitudinal stress distribution at the inside flange surface during pressurization
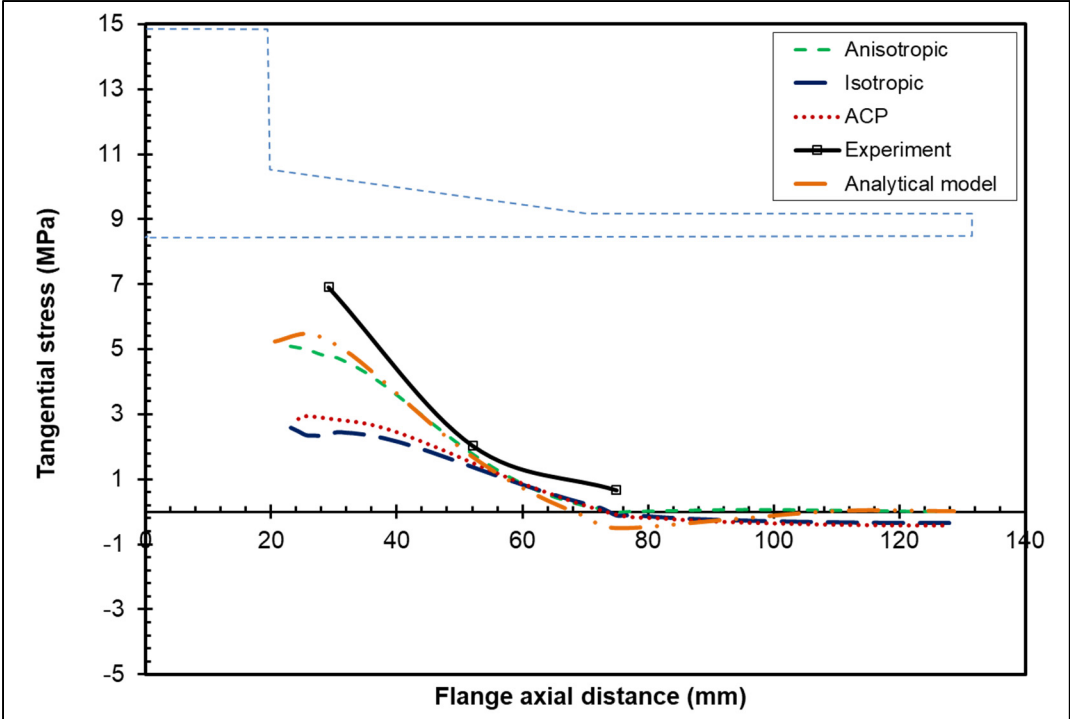

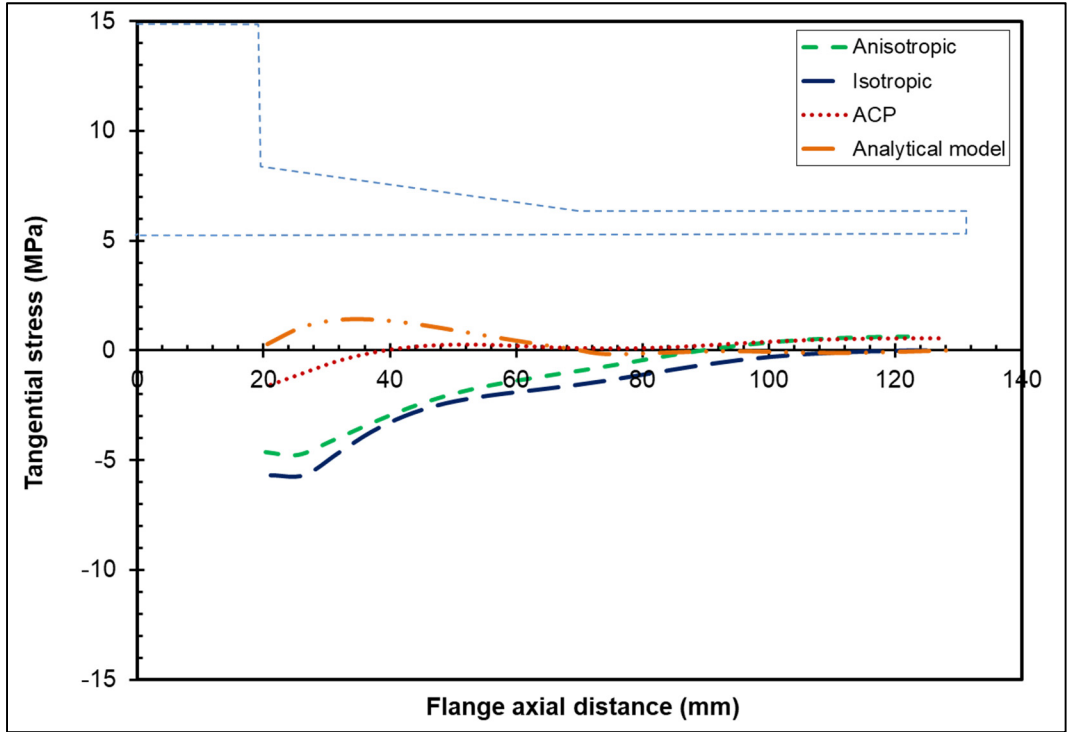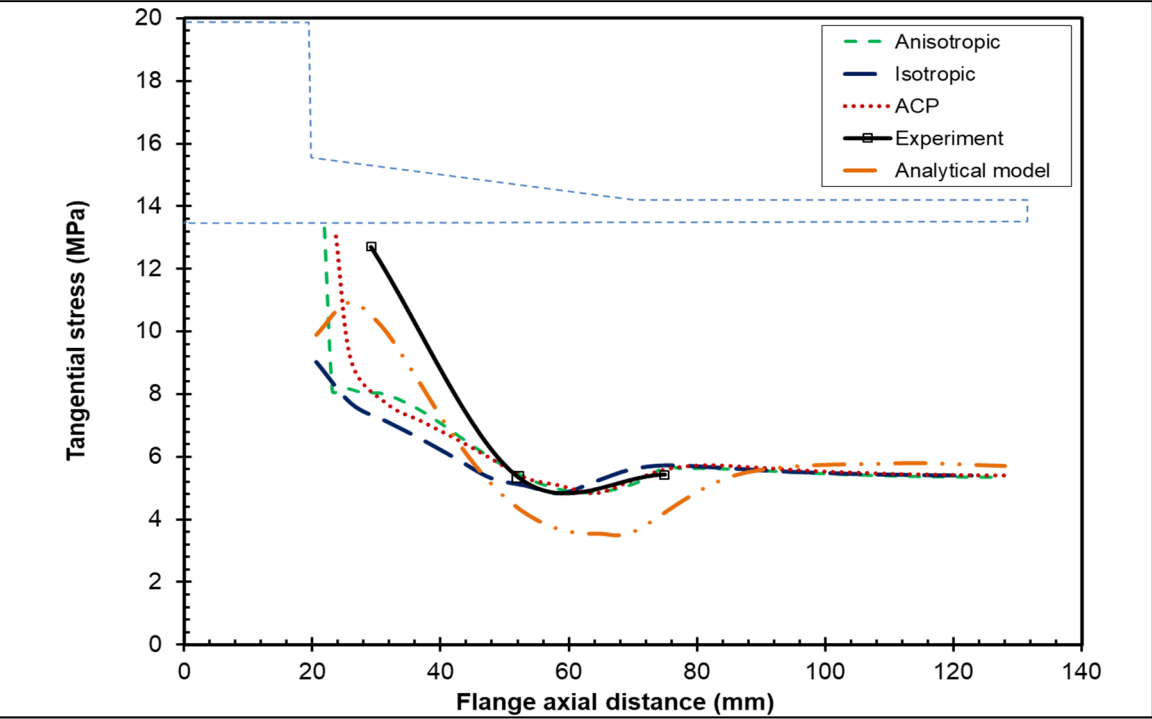Figure 5-7 Tangential stress distribution at the outside flange surface during pressurization
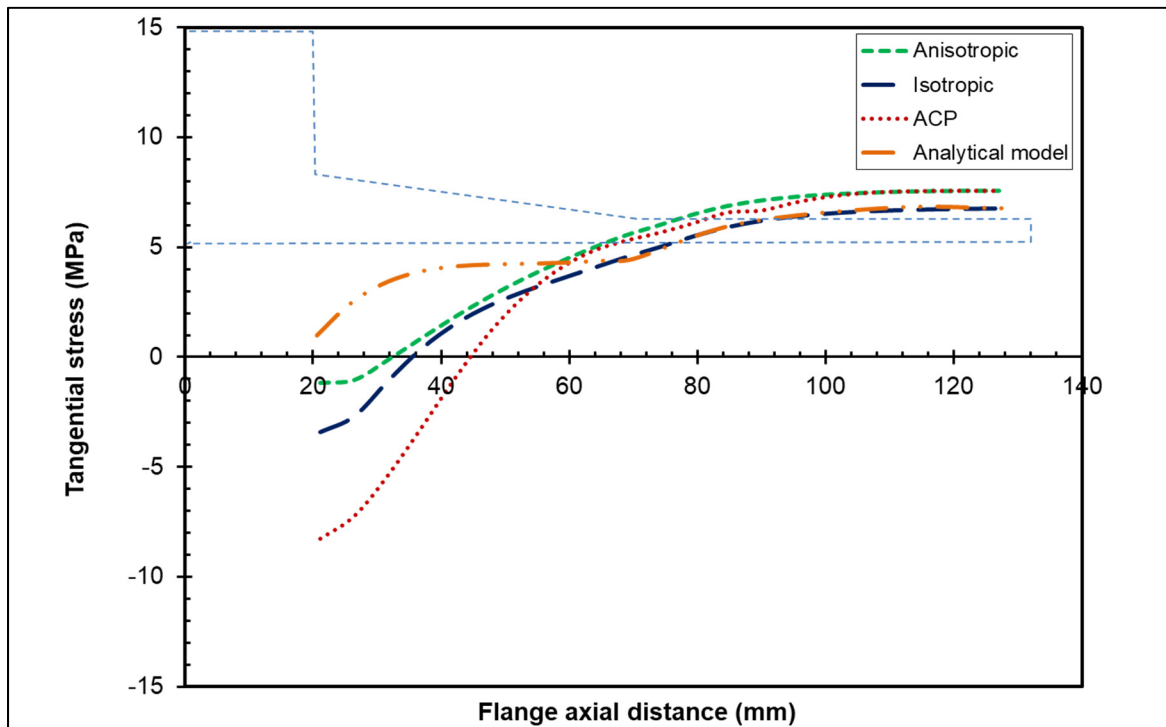
Figure 5-8 Tangential stress distribution at the inside flange surface during pressurization

Although in the cylindrical part of the flange, the tangential stress at the inner surface show around 15% difference at the hub to flange ring junction. The difference is even smaller far away from the junction as shown by the stress distribution at the inside and outside surfaces of the flange during pressurization. In general, the graphs show the importance of including material anisotropy in FE models of composite flanges. Comparing the tangential and longitudinal stresses obtained from ACP and other models based on anisotropy the difference is small as compared to the model with isotropic material behavior. Increasing the size of the flange will also lead to a larger result difference. Nevertheless, the importance of including material anisotropy to predict the stresses and strains in composite flanges is acknowledged.

The results obtained from different finite element models and the experimental test data points to the fact the analytical model is reliable and the methodology used to predict the stresses and strains in bolted flange joint is robust.

5.2.2 Radial displacement

The radial displacement at the inside radius of the flange for bolt-up and at 1.345 MPa internal pressure is illustrated in figures 5-9 and 5-10. Each graph has four curves; three curves obtained from the three different FE models and one curve is obtained from the proposed analytical model. These figures show that the radial displacements all models follow a similar trend during bolt-up and pressurization. Furthermore, the anisotropic FE model and analytical model are in a good agreement, in particular, in the cylindrical part of the flange. Although the trend is the same, the ACP model tends to underestimate the displacements.
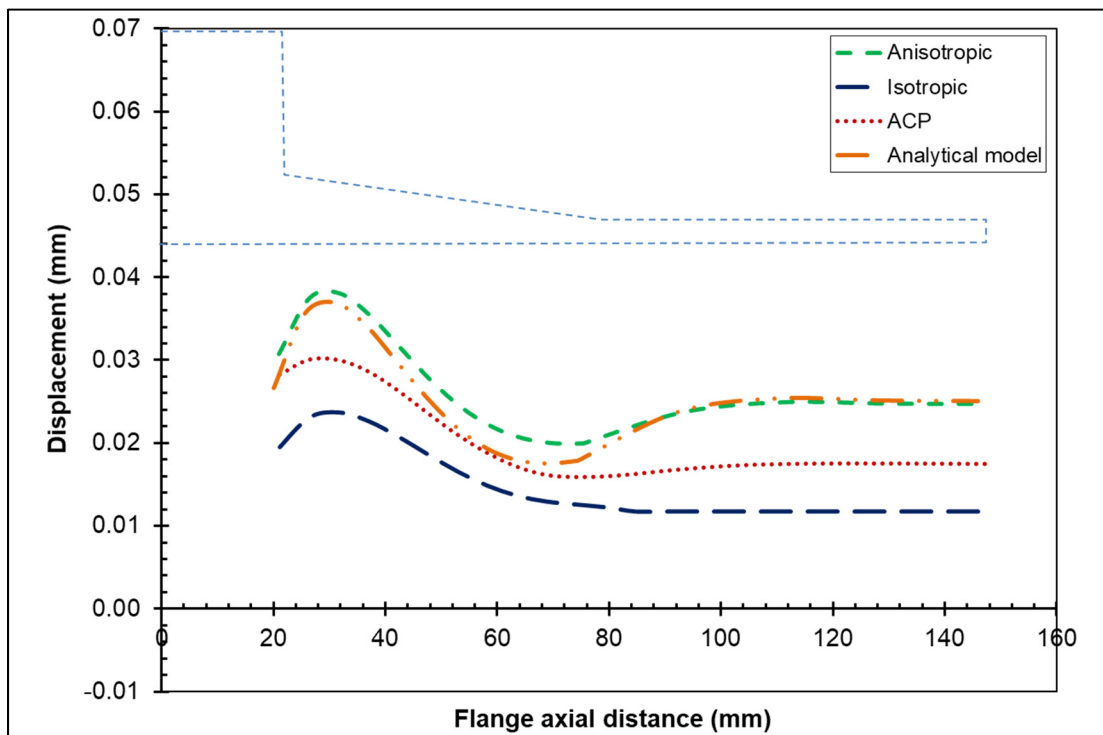
Figure 5-9 Radial displacement of the flange during bolt-up
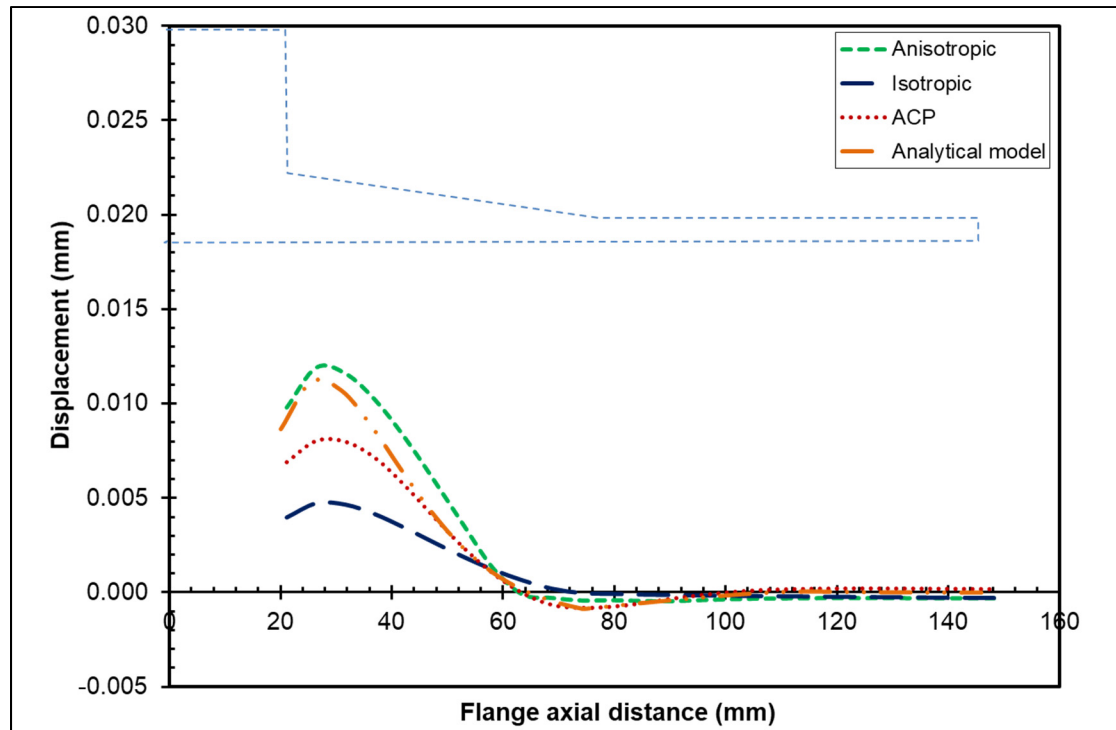
Figure 5-10 Radial displacement of the flange during pressurization

The highest difference is around 40% located at shell side when isotropic material properties of the flange are considered. Once again, the anisotropy of composite materials is important to estimate the radial displacement of the FRP flange. The anisotropic analytical developed model based on the laminated composite theory is justified.

5.2.3   Gasket contact stress

In figure 5-11 the distribution of the gasket contact stress for the three different FE models are shown. In this graph, the gasket contact stress distribution is depicted as a function of the normalized gasket width. As anticipated and like in metallic flange joints, the maximum contact stress occurs at the gasket outside diameter and is caused by flange rotation that produces a higher flange axial displacement at the outer edge of the gasket. In general, the distribution of contact stress depends on two factors; the rotation of the flange and the nonlinear behavior of the gasket.
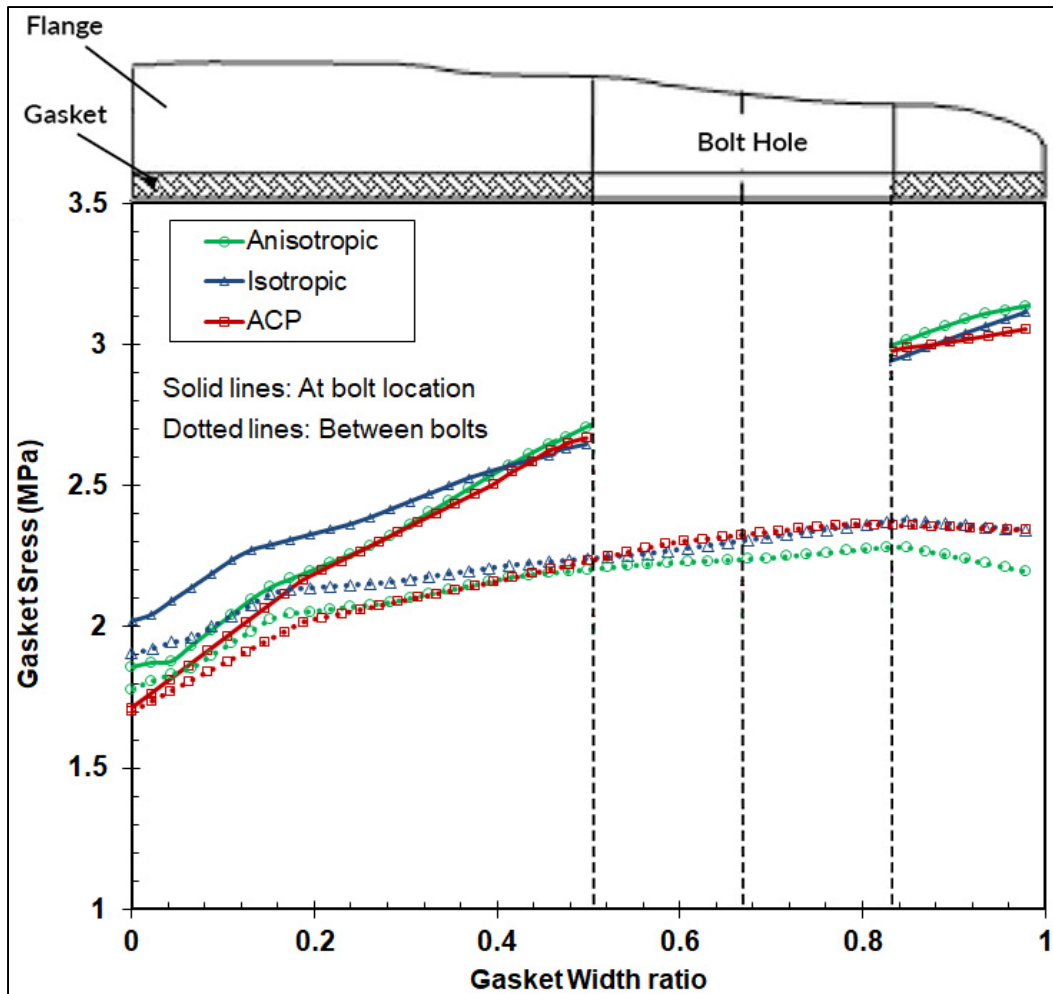
Figure 5-11 Distribution of the gasket contact stress as a function of a gasket width

The graphs in figure 5-11 indicate that the critical stress occurs at the vicinity of the bolt and it would appear that the gasket stress distribution has a similar trend for all three FE models. However, in comparison with the metallic bolted flange joints (Black, 1994), the contact stresses in the gasket at the bolt location are much higher than those between bolts. This is expected since there is higher flexibility with FRP materials like other composite materials as compared to steel and other ferrous materials.

5.3   Results for the NPS 12 flange without the hub

In this part, the analytical results are presented and compared to the numerical results obtained from the FE modeling of the NPS 12 FRP bolted flange joint with multilayered composites. Each graph gives compares the analytical to the numerical results. The analytical results are obtained through the MATLAB program for the NPS 12 FRP bolted flange joint the theory of which is detailed in chapter 2.

5.3.1   Flange stresses

Longitudinal and tangential stress distribution at the outside and inside surfaces of the flange for the two conditions of bolt-up and pressurization are illustrated in figures 5-12 to 5-20. From these figures, it can be stated that analytical results are consistently close to the numerical results.

Figure 5-12 Longitudinal stress distribution at the outside flange surface during bolt-up
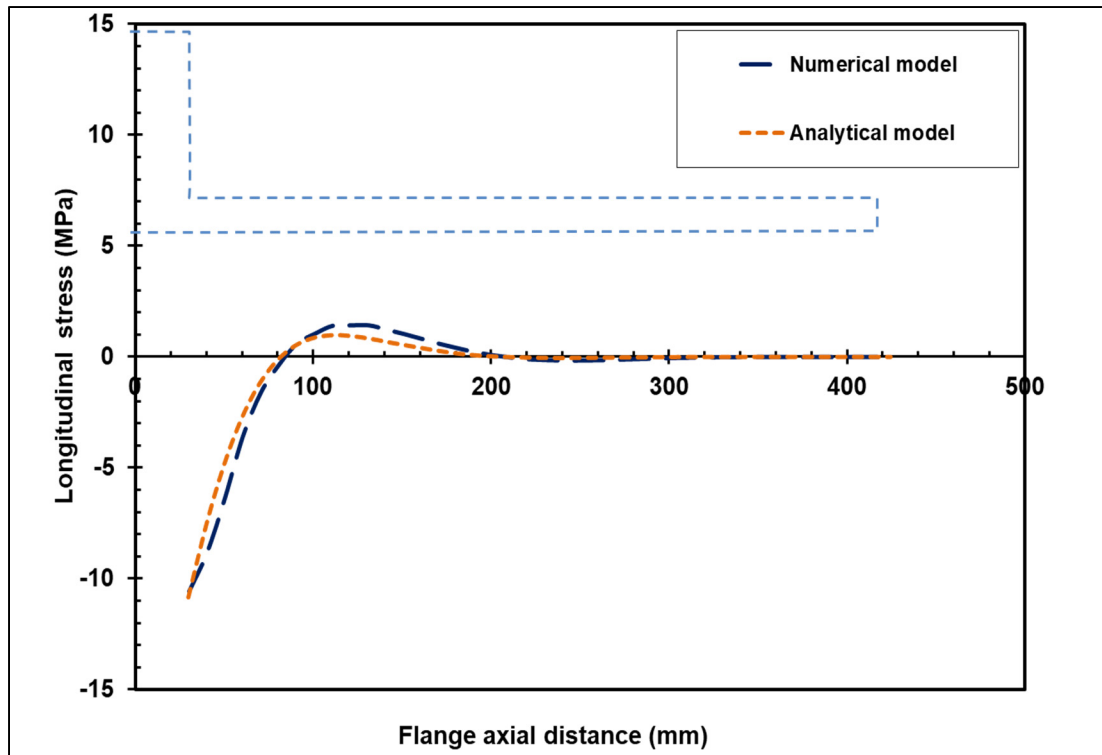
Figure 5-13 Longitudinal stress distribution at the inside flange surface during bolt-up

As shown in the figures 5-12 to 5-16, during bolt-up, the stress distribution in the shell far from the flange ring is not significant.

As can be observed in figures 5-18 and 5-19 there is some slight difference around 14% in the stresses at the junction of the ring and shell. Although in the FE multi-layered composite model the junction of the ring and shell laminates are not adequately bonded together to ensure continuity there is a slight difference in longitudinal and tangential stress distributions between the analytical and numerical models. The stresses near the junction dramatically increased by 43% but the general behavior as a result of discontinuity is picked up by both models. Although the tendency is similar, the FE model lacks accuracy due to the ring and shell laminate bounding discrepancy.
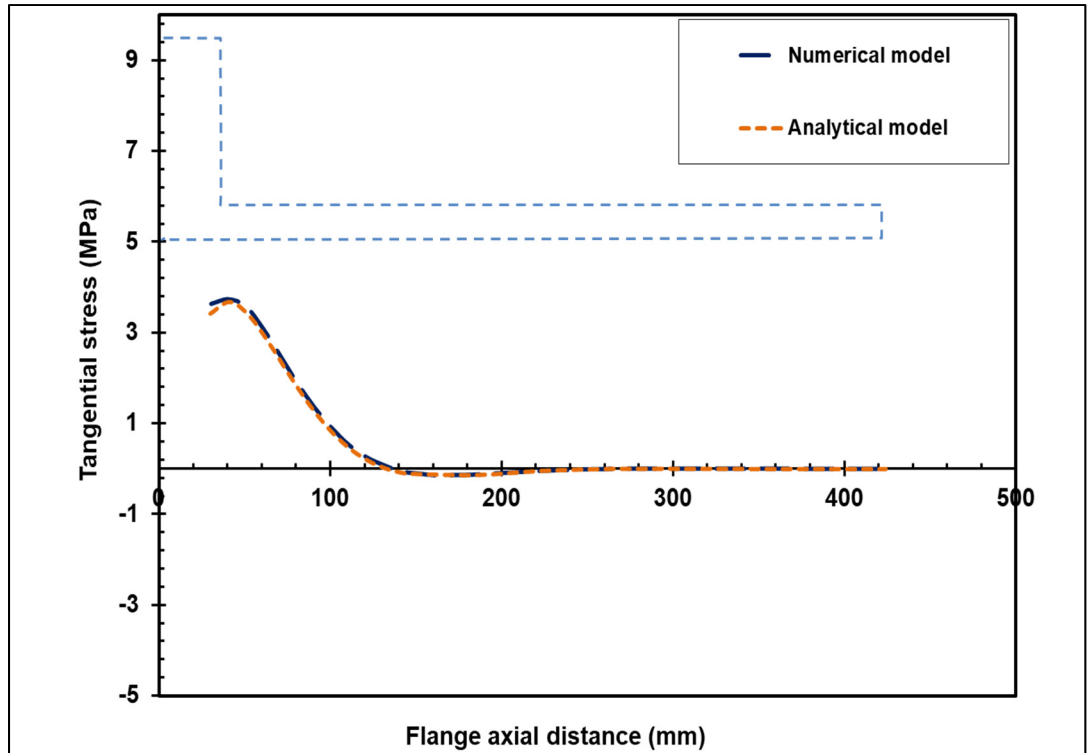
Figure 5-14 Tangential stress distribution at the outside flange surface during bolt-up
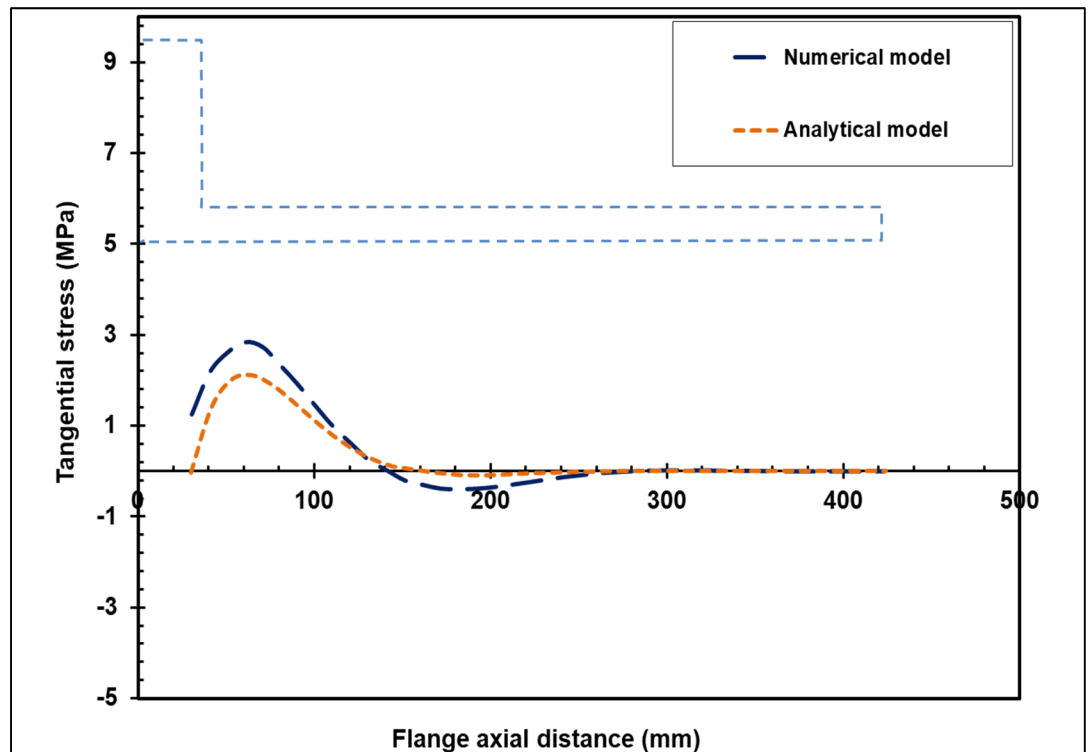
Figure 5-15 Tangential stress distribution at the inside flange surface during bolt-up

In general, the graphs show a good agreement between the results of the analytical model and numerical model; this supports the robustness and accuracy of the proposed analytical model. In fact, the analytical approach and the FE model show the stress increase at the junction of the ring and the shell where the maximum stress concentration exists. Furthermore, a thorough investigation of the distribution of stresses in the specific laminate lay-up of the bolted flange joint with the hub will be conducted and presented in section 5.4.
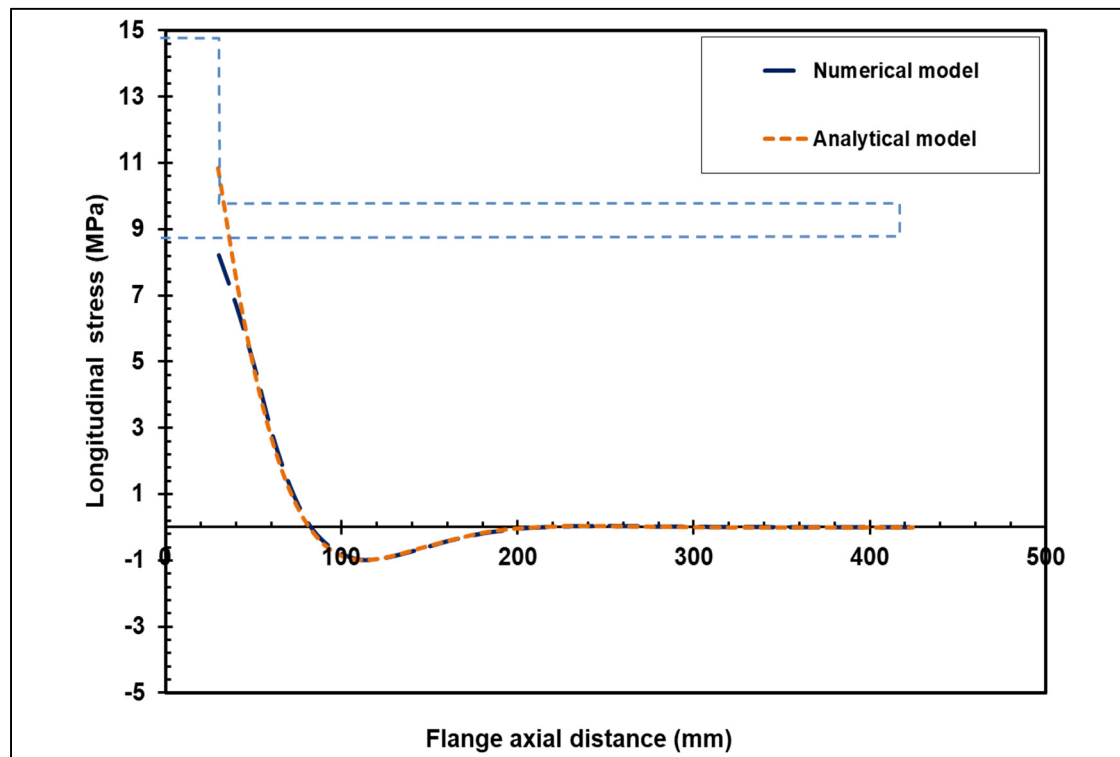

Figure 5-16 Longitudinal stress distribution at the outside flang surface during pressurization

Figure 5-17 Longitudinal stress distribution at the inside flange surface during pressurization

Figure 5-18 Tangential stress distribution at the outside flange surface during pressurization

Figure 5-19 Tangential stress distribution at the inside flange surface during pressurization

5.3.2   Radial displacement

The radial displacement of the flange during bolt-up and pressurization are depicted in Figure 5-20. The comparison between the results obtained from the analytical and FE models show a good agreement at all locations along the shell axial length of FRP flange. The difference observed between the analytical and numerical models is less than 9% and 5% during bolt-up and pressurization respectively. Obviously, the good agreement between the two models confirms the accuracy of the analytical approach of FRP bolted flange joint.
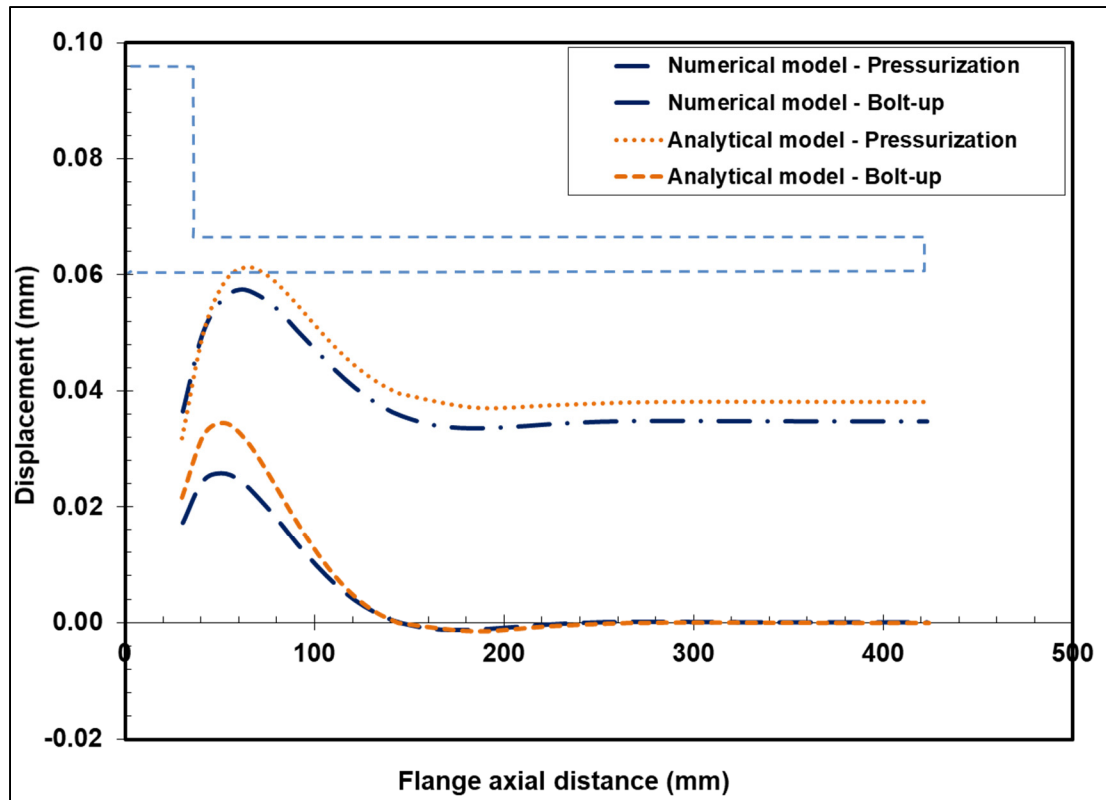
Figure 5-20 Radial displacement of the flange during bolt-up and pressurization

5.4 Results for the NPS 12 flange with the hub

In this section, the results for the NPS 12 class 150 FRP bolted flange joints with the hub are presented. Comparisons of the longitudinal and tangential flange stresses and radial displacement obtained from the analytical and FE models are conducted with special focus on the hub region. FRP flange with the hub requires a more elaborate model that includes the three parts; shell, hub, and ring. The analytical results obtained from the MATLAB program for a bolted flange joint with the hub is available in Appendix A.

5.4.1 Flange stresses

The longitudinal and tangential stress distributions at the inside and outside surface of the flange at bolt-up are illustrated in Figures 5-21 to 5-24. These figures show clearly that the

analytical and FE distributions at the inside and outside flange surfaces during bolt-up have the same tendency. In this case, the distributions of the longitudinal and tangential stresses are in a good agreement and the results are in concordance, with a difference of less than 4%. As anticipated during bolt-up, due to the lack of the pressure inside of FRP bolted flange joints, the stresses in the shell far away from the hub and shell junction are nil.

Figures 5-25 to 5-28 present the longitudinal and tangential stress distributions after the application of internal pressure of 1.345 MPa. A similar stress distribution trend along the hub and cylinder length is observed in both the analytical and FE models. However, the FE numerical results show higher stress values at the outside flange surface near the junctions of the hub and the shell and the hub and ring flange (see figure 5-25 and 5-26). In comparing the analytical and numerical results near the junctions of the hub and the ring, the difference observed between the two is around 22% and 18% for the longitudinal stress distribution at the outside and inside flange surface respectively. Such differences are anticipated because these junctions are smoother and the laminates are not interconnected in the FE models. Moreover, the presence of the high local stresses in the composite flanges affects considerably the stress distribution particularly at the outside surface of the hub and shell. Since the material properties vary through the thickness of the composite flanges, there is an even distribution of stresses. Although in the junction of hub and ring, the longitudinal stress at inner and outer surfaces show around 20% maximum difference, the distributions very consistent (figures 5-25 and 5-26).
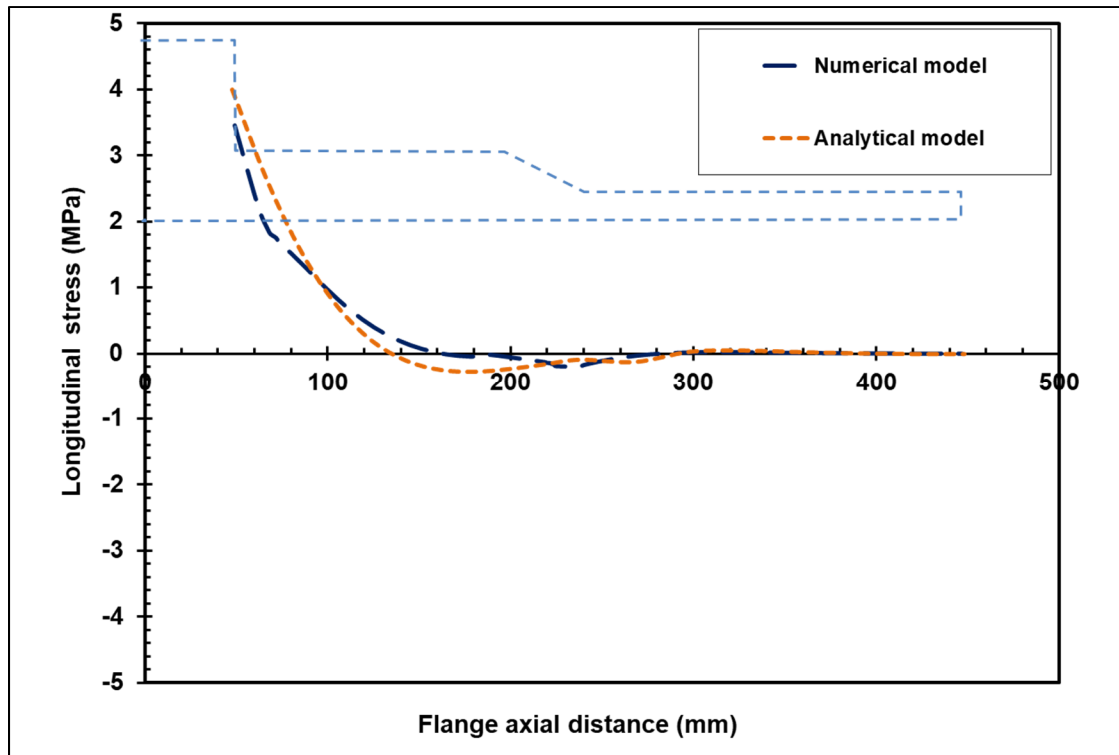
Figure 5-21 Longitudinal stress distribution at the outside flange surface during bolt-up
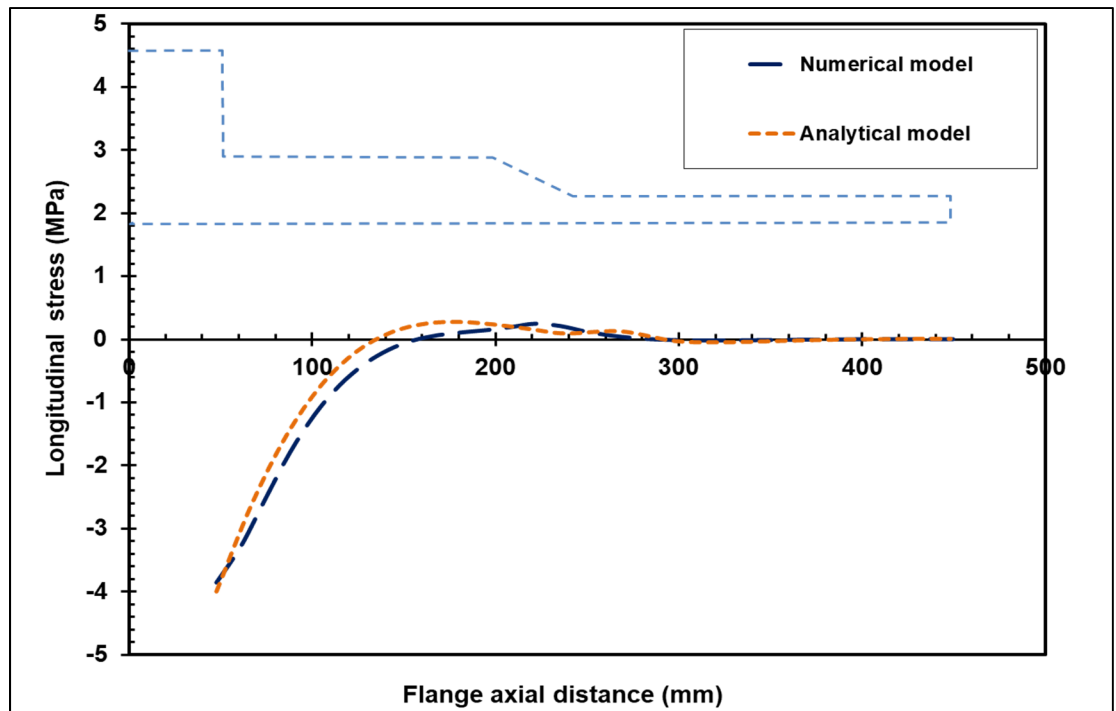
Figure 5-22 Longitudinal stress distribution at the inside flange surface during bolt-up
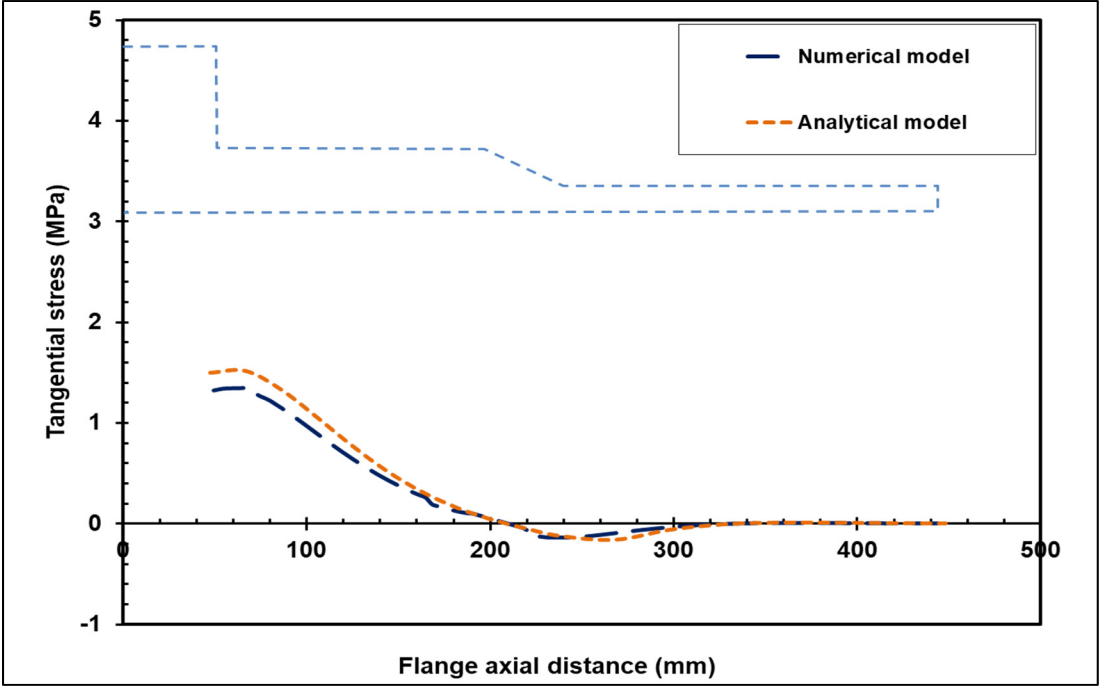
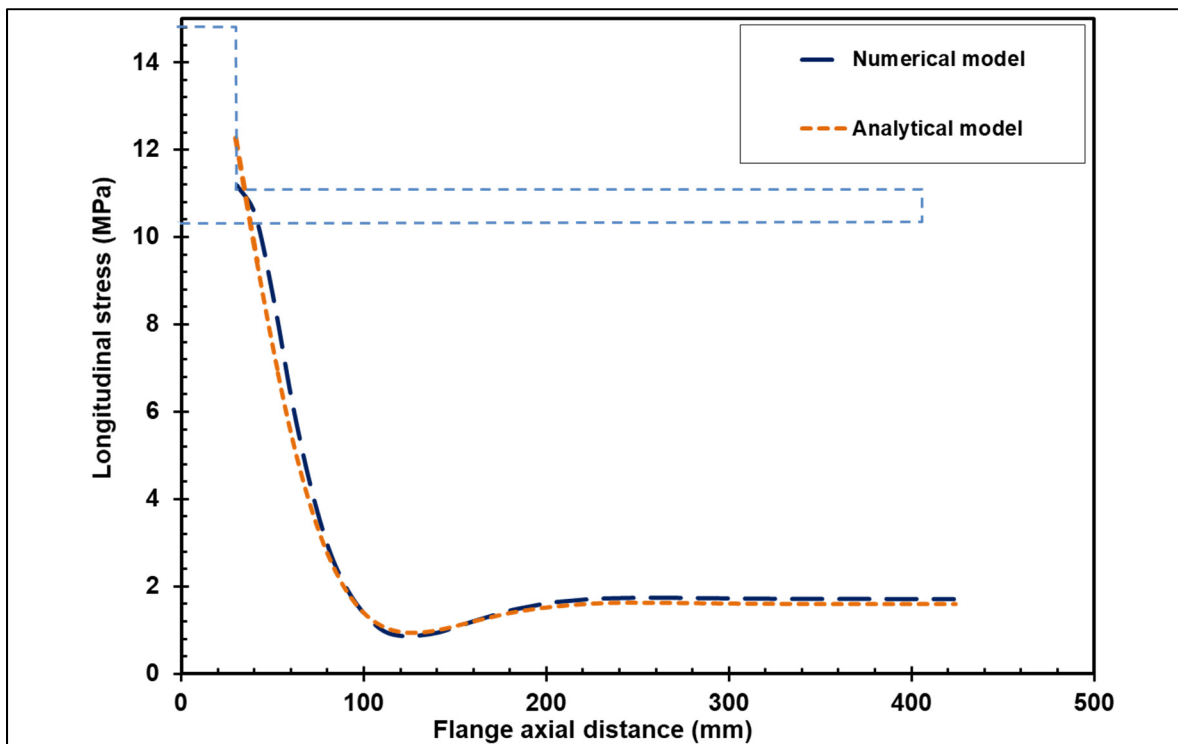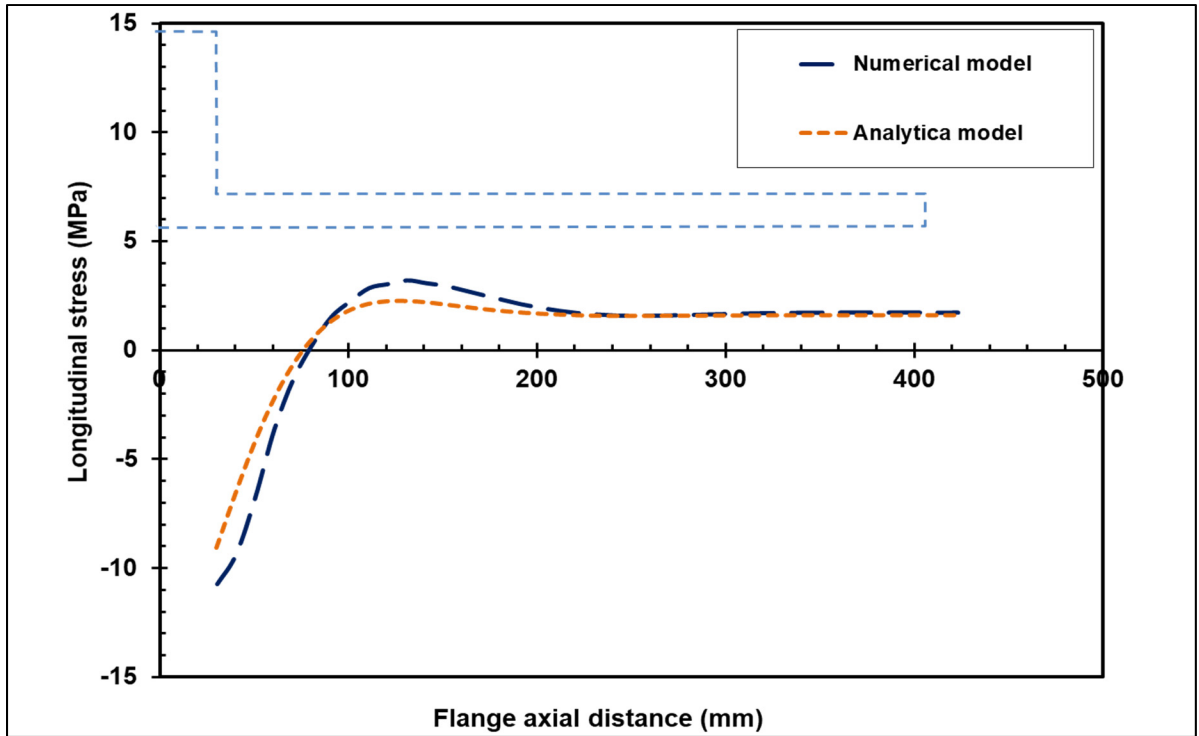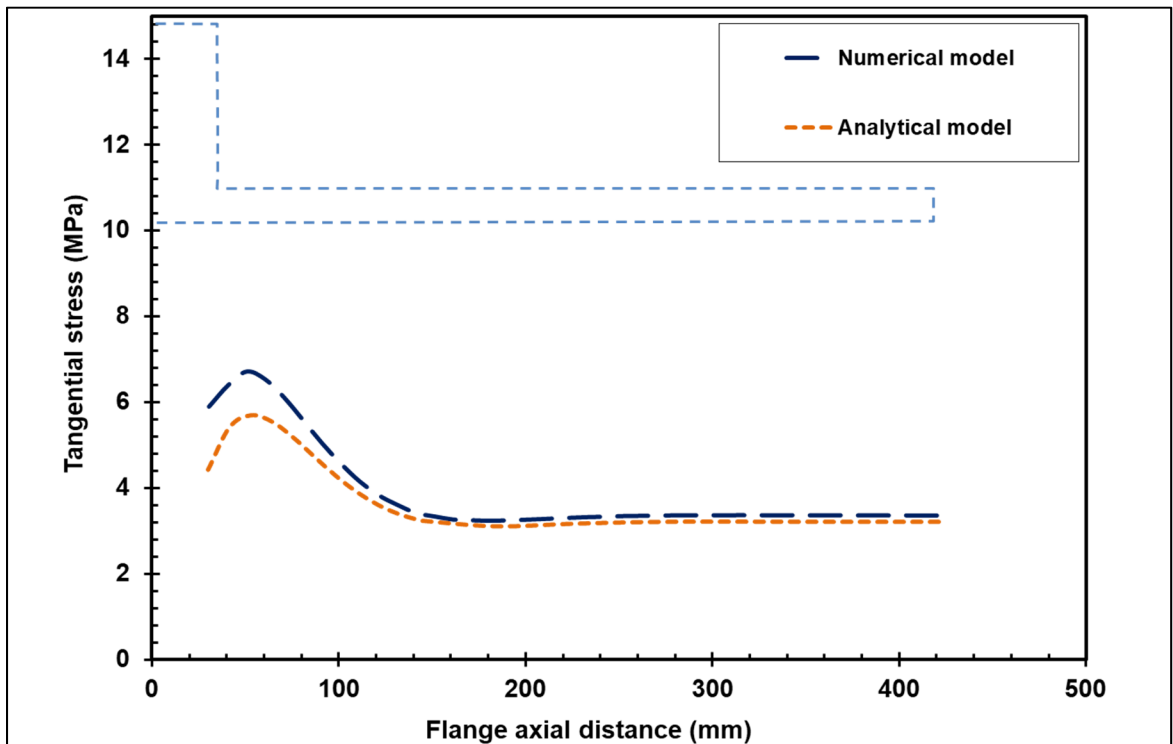Figure 5-23 Tangential stress distribution at the outside flange surface during bolt-up
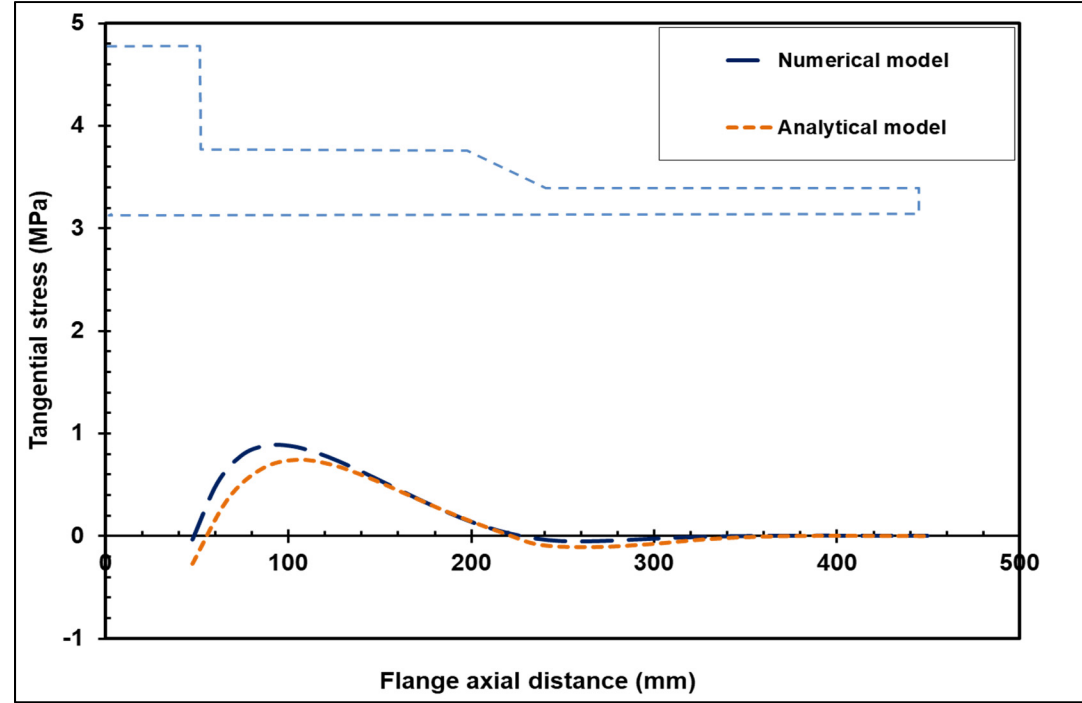
Figure 5-24 Tangential stress distribution at the inside flange surface during bolt-up

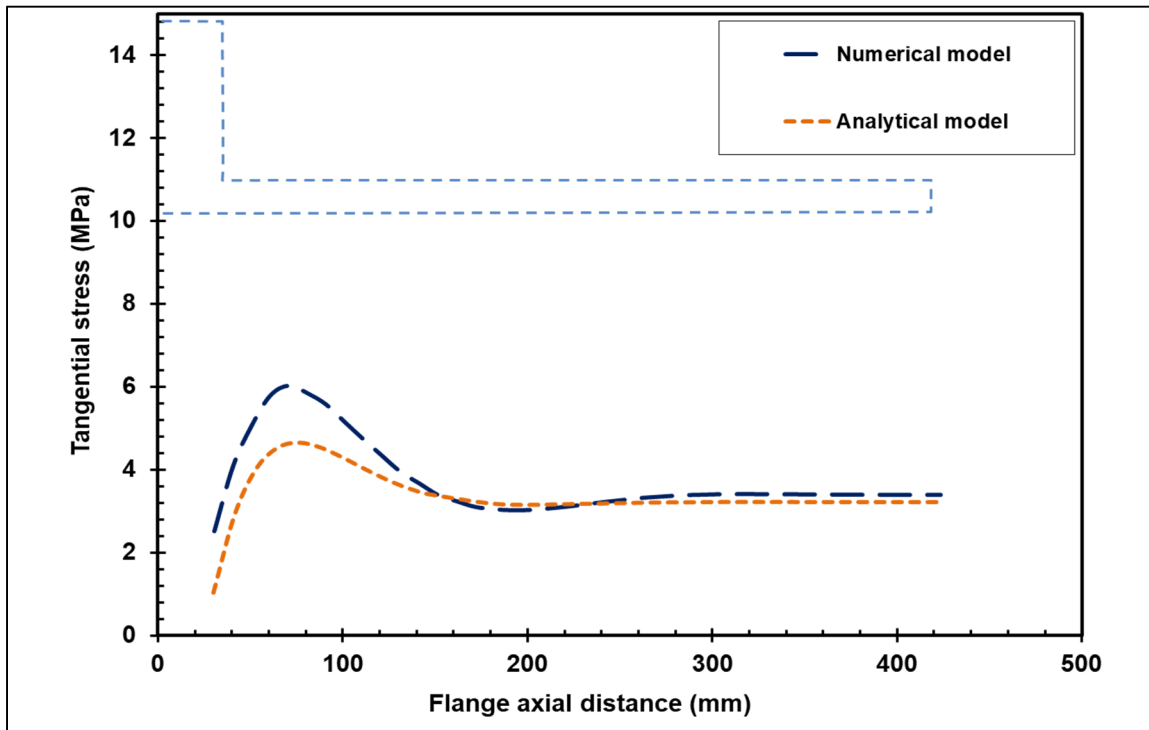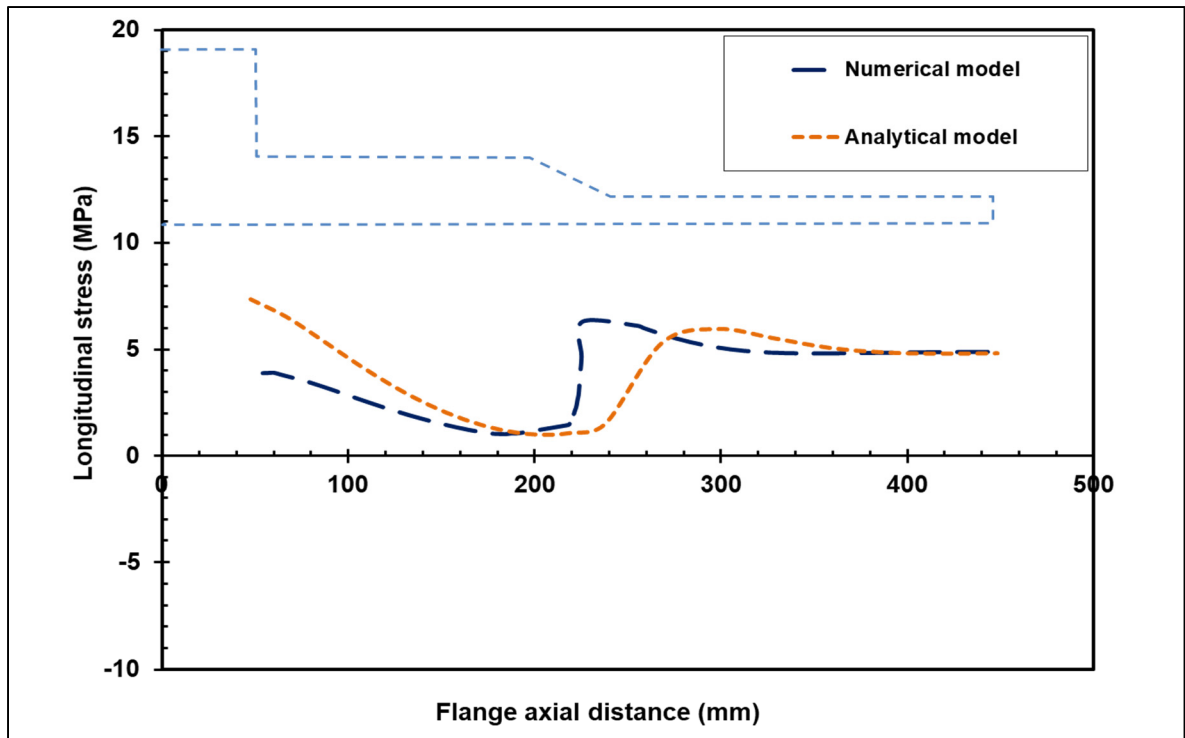Figure 5-25 Longitudinal stress distribution at the outside flang surface during pressurization
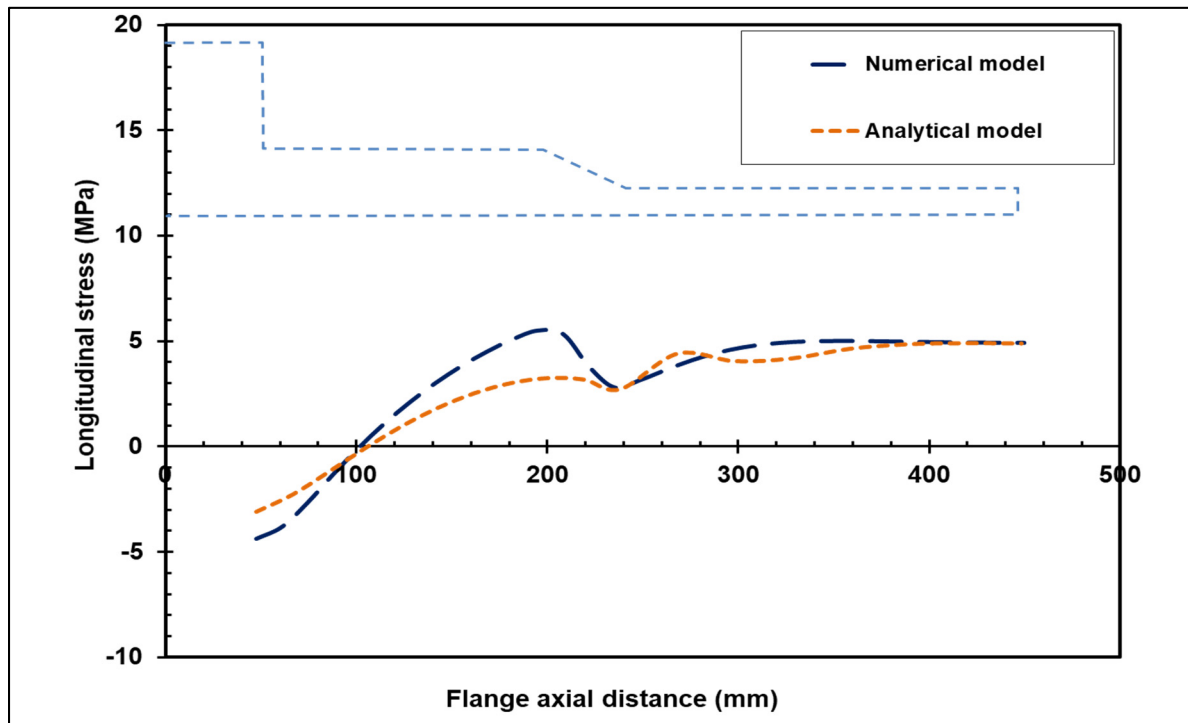
Figure 5-26 Longitudinal stress distribution at the inside flange surface during pressurization

Figures 5-27 and 5-28 show a relatively good agreement between the analytical and FE models during pressurization with a difference of less than 4% except in the junctions. Nevertheless, while the results of the tangential stresses at the inner and outer flange surface are shown to have the same trend, those at the hub show a slight discrepancy that is acceptable in the design since some simplifications were made at the junctions. Indeed as expected, at the junction of the hub and the shell where the maximum stress concentration exists, the stresses at this location increased drastically by around 92%. This phenomenon also occurs near the hub to the flange ring junction. It is to be noted that considering the small tapered portion of the hub that is not considered in the analytical model, the results would be affected. Nonetheless, the difference is not significant and is acceptable for design purposes.
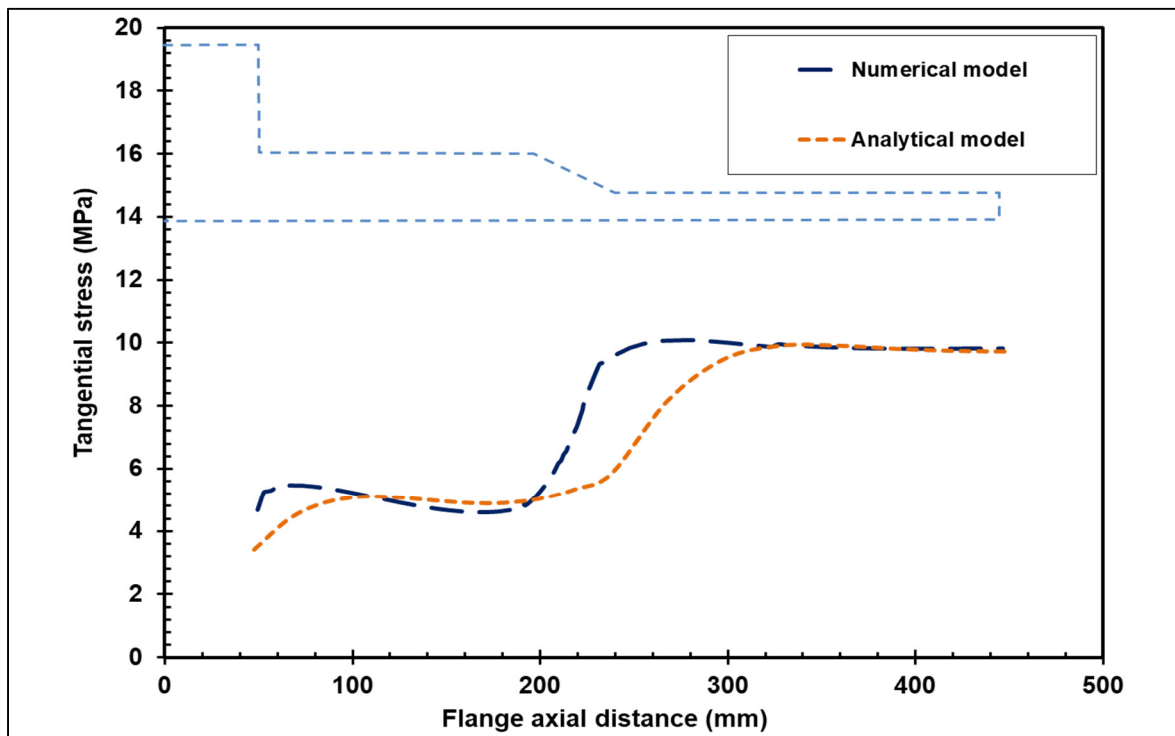
Figure 5-27 Tangential stress distribution at the outside flange surface during pressurization
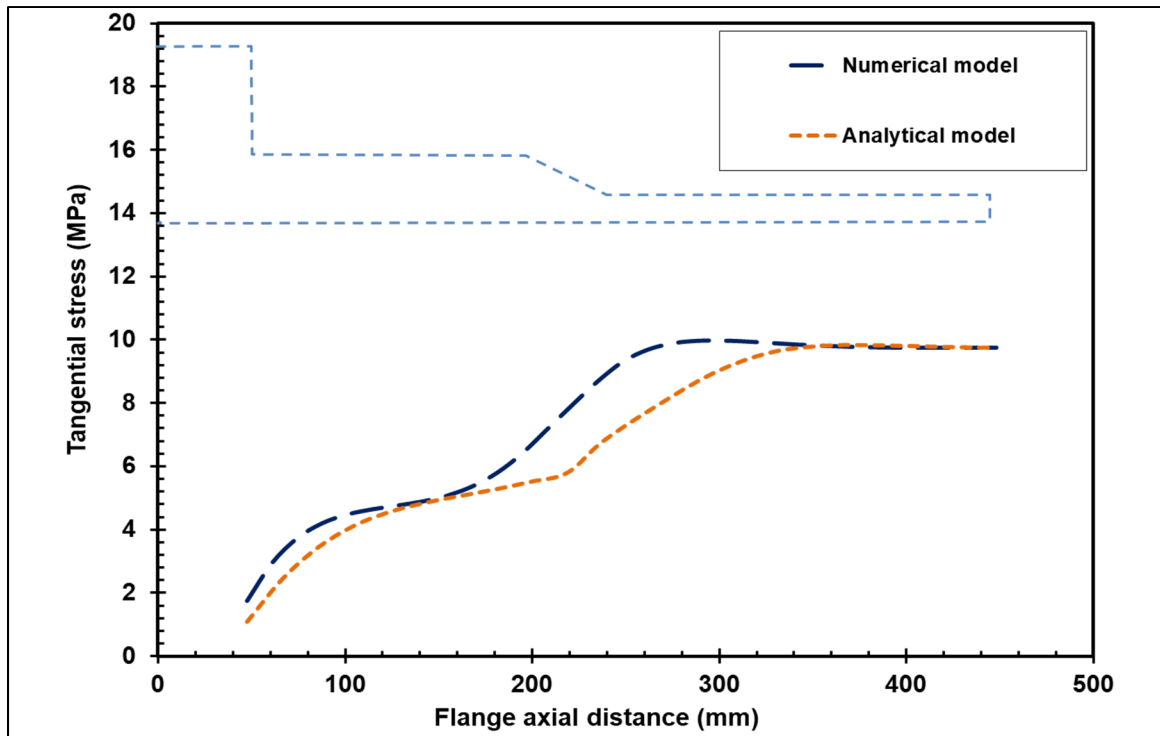
Figure 5-28 Tangential stress distribution at the inside flange surface during pressurization

5.4.2 Radial displacement

The radial displacement results obtained from numerical and analytical models of FRP bolted flange joint with the hub at bolt-up and pressurization are compared in figure 5-29. As shown in the figures, there has not a similar trend but are in good agreement with each other. The difference observed between the analytical and numerical results is less than 3% and 5% during bolt-up and pressurization respectively.

From these figures, the radial displacement of the shell is shown to be much higher than the flange ring and hub because these two structures are much stiffer.
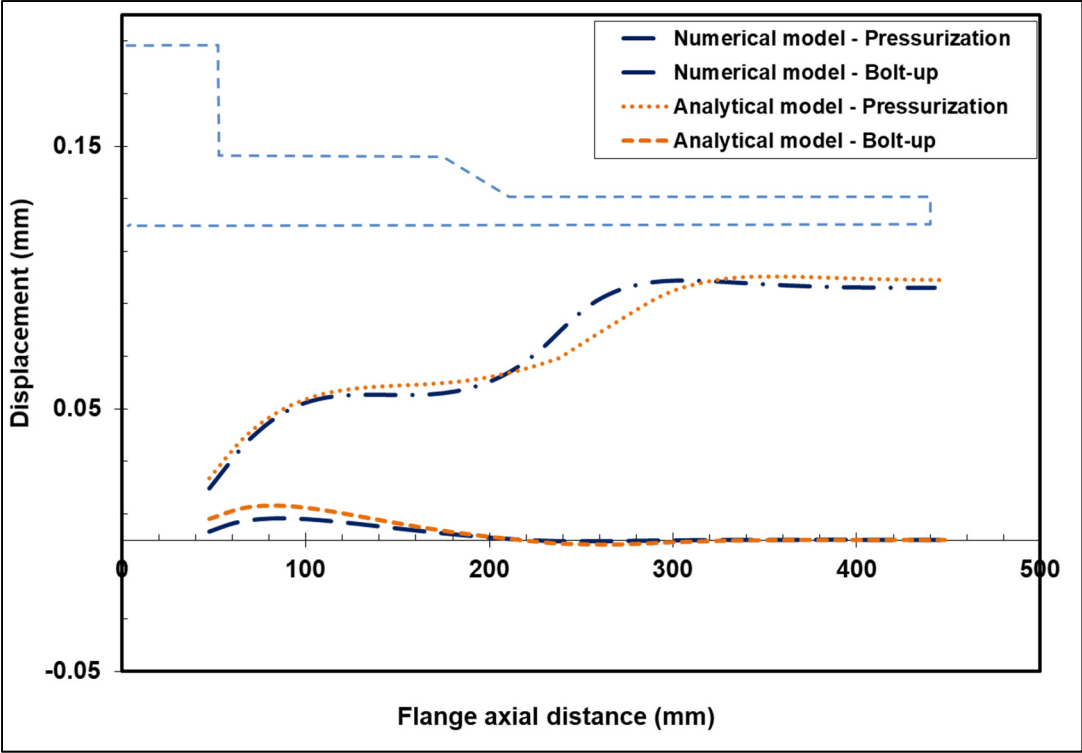
Figure 5-29 Radial displacement of the flange during bolt-up and pressurization

CONCLUSIONS

The ability of FRP materials to resist in harsh and chemical environments and their comparatively high corrosion resistance has made them the best choice in pressure vessels and piping applications related to chemical, water, gas services, nuclear and petrochemical industries. A comprehensive study of the literature on FRP bolted flange joints was carried out. According to the literature, the current procedure used for the design of FRP flanges is a major concern because of their inappropriateness to address the anisotropic behavior of composite materials.

The main objective of this work was to address this need and develop an accurate analytical model to evaluate the stresses and strains of FRP bolted flange joints taking into consideration the anisotropy of the flange material.

In order to achieve the main objective of this study, a methodology for the analytical, numerical and experimental study was developed. The study is prominent in dealing with the behavior of FRP bolted flange assembly subjected to internal pressure. To allow verification of results, experimental and FE methods were used as complementary methods to validate the robustness of the developed analytical model.

The composite flange was divided into three structures, namely the shell, the hub, and the flange ring or plate. The developed analytical model of FRP flange is based on the theory of composite thin cylinders, the theory of thin plates subjected to transverse loading, and the short cylinder theory adapted for composite materials.

The proposed model was then validated by comparison with the results obtained from experimentation and finite element modeling. The novelty of this analytical model is to treat the integrity and tightness of FRP bolted joint taking into account the anisotropy material behavior and the flexibility of all joint elements including the gasket, bolts, and flanges.

The analytical approach has been developed for FRP bolted flange joints with and without the hub and is based on classical lamination theory for composites and the elastic interaction between all bolted joint assembly components. The developed analytical model presented in chapter 2 includes the flexibility of all parts of the bolted flange joint in both axial and radial direction. The complex design and geometry of FRP flanges make it difficult to develop general analytical studies for this kind of flange. Despite the complexity and rigorous mathematical analysis of the composite flanges, the developed analytical model successfully and accurately reproduced the real behavior of FRP bolted flange joints during bolt-up (or initial tightening) and pressurization (operating) conditions.

Experimentation and numerical finite element modeling are the two-method used for validation of the proposed analytical model. The experimental tests were conducted on a well-equipped test bench that uses a NPS 3 class 150 FRP flange with a hub. Three different FE models for three different type of FRP flanges were modeled; an NPS 3 class 150 with a hub and an NPS 12 class 150 with and without the hub. The stress analysis and comparison are focused on the radial displacement and the tangential and longitudinal stresses at the inside and outside of the flange surfaces. The FE models were developed based on isotropy and anisotropy behavior of FRP materials and anisotropy shell element model using ANSYS PrepPost (ACP).

The stresses obtained from strain measurements in the hub and those from FEM considering anisotropy are reasonably well predicted by the analytical model. The maximum differences observed between the analytical model and experimental measurement and FE numerical models are as follows. In the case of NPS 3 class 150 FRP flange with a hub:

Tangential stress 19%;

Longitudinal stress 14%;

Radial displacement 6%.

In the case of NPS 12 FRP flange without the hub:

Tangential stress 13%;

Longitudinal stress 9%;

Radial displacement 5%.

In the case of NPS 12 FRP flange with the hub:

Tangential stress 17%;

Longitudinal stress 12%;

Radial displacement 5%.

In addition, the work points to the fact that the reliability and accuracy of the FE model of FRP bolted flange joints strongly depends on the consideration of the anisotropy behavior of the flange FRP material. The study shows that isotropy material properties underestimate stresses by around 35%. From the results obtained by both numerical FE model and experimental investigation, the proposed analytical model for FRP flanges with and without the hub has proved to be efficient, accurate and reliable in predicting the longitudinal and tangential stress distribution on the flange surface and radial displacement of the flange. Furthermore, it can be deduced that the FE model which is developed for FRP flanges with and without the hub can explain with acceptable accuracy the stress distribution of FRP bolted flange joints even at the hub part of the flange as well as the junction of the ring and the hub where the maximum stress concentration exists.

The results of this investigation have led to this conclusion that the approach presented in this study provides a formulation consistent with the ASME BPV Code Section X standard, allowing an accurate, reliable and thorough design and evaluation of FRP bolted flange joints. However, additional experimental tests on FRP materials with different properties in the two longitudinal and tangential directions and larger diameter FRP flanges are required to confirm these findings.

RECOMMENDATIONS

Additional experimental tests on larger diameter FRP flanges and other FRP materials with different properties in the two longitudinal and tangential directions could be conducted to further support and validate the accuracy and robustness of the analytical and numerical models for different FRP flange size.

The behavior of FRP materials is affected by the harsh environment and by temperature and humidity. Therefore, future work can be directed towards an investigation of FRP bolted flange joints when exposed to elevated temperature and high humidity. That study involves the use of a combination of experimental, analytical and numerical methods to analyze bolted flange joints made of composite materials from integrity and leak tightness standpoints.

Another major concern of FRP bolted flange joints is their long-term creep-relaxation behavior. The analytical model presented in this thesis could be extended to incorporate load relaxation caused by the creep of the composite flange. The investigation could also include the influence of thermal ratcheting caused by temperature thermal cycling of the composite flange on the bolt load drop.

And finally, experimental studies on the leak rates of FRP bolted flange joints at the ambient and high temperature used with different gasket materials would be valuable work in the future. The current study could be extended to a wider range of application that includes polymeric flange joints and in particular those flanges made out of PVC and HDPE since these are increasingly used in domestic gas and water services.

APPENDIX A

ANALYTICAL PROGRAM FOR FRP BOLTED FLANGE JOINT

```
%-------------------------------------------------------------------------
% ANALYTICAL PROGRAM FOR FRP BOLTED FLANGE JOINTS
% Flange NPS 3
% Flange NPS 12 with the hub
% Flange NPS 12 without the hub
%-------------------------------------------------------------------------
clc;
clear;
% ------------------------------------------------------------------------
%Notations
%h: hub
%s: shell
%p: ring/plate


%-------------------------------------------------------------------------
% Flange NPS 12 with the hub
% ------------------------------------------------------------------------

r_go = 241.3;                       % Outside gasket radius mm
r_gi = 152.4;                       % Inside gasket radius mm
d = 22.7;                           % bolt diameter
d_h = 25.4;                         % bolt hole diameter
p_t = 2;                            % number of thread per mm
l_h = 190.5;                        % hub length _mm_
l_s = 300;                          % effective length of the shell _mm_
r_i = 152.4;                        % flange/shell inner radius _mm_
r_o = 241.3;                        % outer radius of the flange _mm_
r_b = 215.9;                        % bolt circle radius _mm_
t_f = 47.625;                       % thickness of the flange _mm_
t_h = 41.8;                         % equivalent thickness of the hub
_mm
t_s = 17.1;                         % thickness of the shell _mm_(c)
r_h = r_i+t_h/2;                    % hub mean radius mm_
r_s = r_i+t_s/2;                    % inner radius of shell mm
t_g = 3;                            % thickness of the gasket _mm
E_g  = 55;                          % compression modulus of gasket MPa
l_b = 0.5*1.125*d+2*t_f+t_g;        % initial bolt length _mm_
p   = 1.034;                        % internal pressure MPa __
nu_f = 0.2;                         % Poisson's ratio of flange
E_b = 210000;                       % Young's modulus of bolts MPa
S_b = 175.00;                       % bolt stress MPa
n = 12;                             % Number of bolts
nu_s = 0.3;                         % Poisson's ratio of shell
nu_h = 0.3;                         % Poisson's ratio of joint element
```

```
%-------------------------------------------------------------------------
% Flange NPS 12 without the hub
% -------------------------------------------------------------------------

% r_go = 495.3/2;                    % Outside gasket radius mm
% r_gi = 300/2;                      % Outside gasket radius mm
% d = 16;                            % bolt diameter
% d_h = 19;                          % bolt hole diameter
% p_t = 2;                           % number of thread per mm
% l_h = 114.3;                       % hub length _mm_
% l_s = 147.6;                       % effective length of the shell _mm_
% r_i = 300/2;                       % flange/shell inner radius _mm_
% r_o = 495.3/2;                     % outer radius of the flange _mm_
% r_b = 425/2;                       % bolt circle radius _mm_
% t_f = 38.1;                        % thickness of the flange _mm_
% t_h = 27;                          % equivalent thickness of the hub
_mm_
% t_s = 17;                          % thickness of the shell _mm_(c)
% r_h = r_i+t_h/2;                   % hub mean radius mm_
% r_s = r_i+t_s/2;                   % inner radius of shell mm
% t_g = 3;                           % thickness of the gasket _mm
% E_g  = 55;                         % compression modulus of gasket MPa
% l_b = 0.5*1.125*d+2*t_f+t_g;       % initial bolt length _mm_
% p   = 0.3450;                      % internal pressure MPa __
% nu_f = 0.2;                        % Poisson's ratio of flange
% E_b = 210000;                      % Young's modulus of bolts MPa
% S_b = 175.00;                      % bolt stress MPa
% n = 12;                            % Number of bolts
% nu_s = 0.3;                        % Poisson's ratio of shell
% nu_h = 0.3;                        % Poisson's ratio of joint element


% -------------------------------------------------------------------------
% Flange NPS 3
% -------------------------------------------------------------------------

r_go = 7.5/2*25.4;                   % Outside gasket radius mm
r_gi = 3/2*25.4;                     % Inside gasket radius mm
d = 0.625*25.4;                      % bolt diameter mm
d_h = 0.75*25.4;                     % bolt hole diameter mm
p_t = 11*25.4;                       % number of thread per mm
l_h = 2.139*25.4;                    % hub length mm
l_s =  7.048*25.4;                   % effective length of the shell mm
r_i = 3/2*25.4;                      % flange/shell inner radius mm
r_o = 7.5/2*25.4;                    % outer radius of the flange mm
r_b = 6/2*25.4;                      % bolt circle radius mm
t_f = 0.813*25.4;                    % thickness of the flange mm
t_h = 0.607*25.4;                    % equivalent thickness of the hub
mm
t_s = 0.25*25.4 ;                    % thickness of the shell mm
r_h = r_i+t_h/2;                     % hub mean radius mm
r_s = r_i+t_s/2;                     % inner radius of shell mm
t_g = 0.125*25.4;                    % thickness of the gasket mm
E_g  = 55;                           % compression modulus of gasket MPa
l_b = 0.5*1.125*d+2*t_f+t_g;         % initial bolt length mm
```

```
p   = 1.034;                            % internal pressure MPa
nu_f = 0.2;                             % Poisson's ratio of flange
E_b = 210000;                           % Young's modulus of bolts MPa
S_b = 175;                              % bolt stress MPa
n = 4;                                  % Number of bolts
nu_s = 0.3;                             % Poisson's ratio of shell
nu_h = 0.3;                             % Poisson's ratio of shell

% --------------------------------------------------------------------
%Laminate Data for NPS 3

% As=[21.5, 21.5,3.38]*10000;
% Bs=[0,0,0];
% Ds=[5190,5190,825.3]*1000;
%
% Ah=[21.5, 21.5,3.38]*10000;
% Bh=[0,0,0];
% Dh=[5190,5190,825.3]*1000;
%
%As=Ah;
%Ds=Dh;
%
% Ap=[39.7,39.7,6.09]*10000;
% Bp=[0,0,0];
% Dp=[29484,29484,4615]*1000;


%--------------------------------------------------------------------

A_b = n*pi*(d-0.9382/p_t)^2/4;      % Bolt stress area mm^2
A_br = n*pi*(d-1.22687/p_t)^2/4;    % Bolt root area mm^2
F_b = S_b*A_br;                     % bolt force _N_
F_g  = F_b;                         % gasket force _N_

r_g = 2/3*(r_gi^2+r_go^2+r_gi*r_go)/(r_gi+r_go);% effective gasket radius
_mm_
r_g=r_gi+2/3*(r_go-r_gi)/2;
A_p = pi*r_g^2;

K_b = A_b*E_b/l_b;                      % bolt uniaxial stiffness _N/mm_
A_g = pi*(r_go^2-r_gi^2);               % gasket are mm^2
K_g = A_g*E_g/t_g;                      % gasket uniaxial stiffness _N/m_

%Shell laminate
beta_s = ((As(2)*As(1)-(As(3))^2)/(4*r_s^2*Ds(1)*As(1)))^(1/4);
D_s = Ds(1);
%Hub laminate
beta_h = ((Ah(2)*Ah(1)-(Ah(3))^2)/(4*r_h^2*Dh(1)*Ah(1)))^(1/4);
D_h = Dh(1);

B11=(sinh(2*beta_h*l_h)-sin(2*beta_h*l_h))/(2*((sinh(beta_h*l_h))^2-
(sin(beta_h*l_h))^2));
B12=(cosh(2*beta_h*l_h)-cos(2*beta_h*l_h))/(2*((sinh(beta_h*l_h))^2-
(sin(beta_h*l_h))^2));
B22=(sinh(2*beta_h*l_h)+sin(2*beta_h*l_h))/((sinh(beta_h*l_h))^2-
(sin(beta_h*l_h))^2);
```

```
G11=-(cosh(beta_h*l_h)*sin(beta_h*l_h)-
sinh(beta_h*l_h)*cos(beta_h*l_h))/((sinh(beta_h*l_h))^2-
(sin(beta_h*l_h))^2);
G12=-2*sinh(beta_h*l_h)*sin(beta_h*l_h)/((sinh(beta_h*l_h))^2-
(sin(beta_h*l_h))^2);
G22=-
2*(cosh(beta_h*l_h)*sin(beta_h*l_h)+sinh(beta_h*l_h)*cos(beta_h*l_h))/((si
nh(beta_h*l_h))^2-(sin(beta_h*l_h))^2);


C_5 = 2;
C_6 = 0;
C_7 = 0;
C_8 = 0;


K = r_o/r_i;

D0=2*(r_o-r_i)/log(K);
D0=D0-(d_h/(pi*2*r_b/n)*(D0-2*d/log((2*r_b+d)/(2*r_b-d))));


r_m=D0/2;

%Plate theory
L2=(r_i*r_o^2)/((r_o^2-r_i^2)*(Ap(3)-Ap(1)));
L1=(r_i^3)/((r_o^2-r_i^2)*(Ap(3)+Ap(1)));
L23=(r_i-2*r_i*log(r_i/r_o))/(8*Dp(1)*pi);
L24=-r_i*((r_o^2-r_i^2)*(Dp(3)-
Dp(1))+2*r_i^2*log(r_i/r_o)*(Dp(1)+Dp(3)))/(8*Dp(1)*pi*(r_o^2-
r_i^2)*(Dp(1)+Dp(3)));
L25=-r_o^2*r_i*log(r_i/r_o)*(Dp(1)+Dp(3))/(4*Dp(1)*pi*(r_o^2-
r_i^2)*(Dp(1)-Dp(3)));
L20=-r_i^3/((r_o^2-r_i^2)*(Dp(1)+Dp(3)));
L22=-r_o^2*r_i/((r_o^2-r_i^2)*(Dp(1)-Dp(3)));
L26=L20+L22;
L27=L23+L24+L25;


C_9 = 1/K_b + 1/K_g;
C_10 = A_p/K_g;


D = [-
B11/(2*beta_h^3*D_h),B12/(2*beta_h^2*D_h),G11/(2*beta_h^3*D_h),G12/(2*beta
_h^2*D_h),-1,0,0,0,0 ...
    ; -
B12/(2*beta_h^2*D_h),B22/(2*beta_h*D_h),G12/(2*beta_h^2*D_h),G22/(2*beta_h
*D_h),0,-1,0,0,0 ...
    ; -
G11/(2*beta_h^3*D_h),G12/(2*beta_h^2*D_h),B11/(2*beta_h^3*D_h),B12/(2*beta
_h^2*D_h),0,0,-1,0,0 ...
    ; G12/(2*beta_h^2*D_h),-G22/(2*beta_h*D_h),-B12/(2*beta_h^2*D_h),-
B22/(2*beta_h*D_h),0,0,0,-1,0 ...
    ; 1/(2*beta_s^3*D_s) , 1/(2*beta_s^2*D_s),0,0,-1,0,0,0,0 ...
    ; -1/(2*beta_s^2*D_s) , -1/(beta_s*D_s),0,0,0,-1,0,0,0 ...
    ; 0,0,-(L1-L2),0,0,0,-1,t_f/2, 0 ...
    ; 0,0,t_f/2*L26 , -L26,0,0,0,-1, (r_b-r_g)/(2*pi*r_m)*L27 ...
    ; 0,0,0,0,0,0,0, C_5*(r_b-r_g) , C_9];
```

```matlab
U = zeros(9,9);

D(9,:)=0;
U(9)=F_b;
D(9,9)=1;

Coefficient_Matrix = [D];

Results = Coefficient_Matrix\U;

% ------------------------------------------------------------------------

P_1(1) = Results(1);
M_1(1) = Results(2);
P_2(1) = Results(3);
M_2(1) = Results(4);
u_h1(1) = Results(5);
theta_h1(1) = Results(6);
u_h2(1) = Results(7);
thetaf(1) = Results(8);
Fb_b(1) = Results(9);

% ------------------------------------------------------------------------

D(9,8)=C_5*(r_b-r_g);
D(9,9)=C_9;

U = [ -(Ah(1)-Ah(3)/2)/(4*beta_h^4*Ah(1)*Dh(1))*p ; 0 ...
    ; -(Ah(1)-Ah(3)/2)/(4*beta_h^4*Ah(1)*Dh(1))*p ; 0 ...
    ; -(As(1)-As(3)/2)/(4*beta_s^4*As(1)*Ds(1))*p ; 0 ; -(L1-L2)*t_f*p ; -
(r_g-r_i)*(r_g^2+r_i^2)*p/(4*r_m)*L27 ...
    ; C_9*F_b + 2*(r_b-r_g)*thetaf(1) + C_10*p - (C_8)];

Coefficient_Matrix = [D];

Results = Coefficient_Matrix\U;

% ------------------------------------------------------------------------

P_1(2) = Results(1);
M_1(2) = Results(2);
P_2(2) = Results(3);
M_2(2) = Results(4);
u_h1(2) = Results(5);
theta_h1(2) = Results(6);
u_h2(2) = Results(7);
thetaf(2) = Results(8);
Fb_b(2) = Results(9);

k=50;

% ------------------------------------------------------------------------
% Stress Calculation in the hub part
% ------------------------------------------------------------------------
```

```matlab
Slih=zeros(k,2);            % Longitudinal stress at the inside surface of the
hub [MPa]
Sloh=zeros(k,2);            % Longitudinal stress at the outside surface of
the hub [MPa]
Stih=zeros(k,2);            % Tangential stress at the inside surface of the
hub [MPa]
Stoh=zeros(k,2);            % Tangential stress at the outside surface of the
hub [MPa]
xh=zeros(k,1);
u_h2sp=zeros(2,1);
u_h=zeros(k,2)              %Radial displacement [mm]
theta_h=zeros(k,2)         %Rotation
Mh=zeros(k,2)              %Moments [N.mm]
Qh=zeros(k,2)             %Shear forces [N]
Nxh=zeros(k,2)
Nth=zeros(k,2)


for j=1:1:2
u_h2sp(j)=u_h2(j)-(Ah(1)-Ah(3)/2)/(4*beta_h^4*Ah(1)*Dh(1))*p*(j-1);
i=0;
for x = 0:l_h/(k-1):l_h
   i=i+1;
   xh(i)=x;
   F11= (cosh(beta_h*x) * sin(beta_h*x) - sinh(beta_h*x) *
cos(beta_h*x))/2;
   F12= sin(beta_h*x) * sinh(beta_h*x);
   F13= (cosh(beta_h*x) * sin(beta_h*x) + sinh(beta_h*x) *
cos(beta_h*x))/2;
   F14= cosh(beta_h*x) * cos(beta_h*x);

   u_h(i,j)=P_2(j)/(2*beta_h^3*Dh(1))*F11+ M_2(j)/(2*beta_h^2*Dh(1))*F12+
thetaf(j)/beta_h*F13+u_h2sp(j)*F14;
%   u_h(i,j)=(P_2(j)/(beta_h^3*Dh(1))*F11+ M_2(j)/(beta_h^2*Dh(1))*F12+
2*thetaf(j)/beta_h*F13+2*u_h2sp(j)*F14);
   theta_h(i,j)=beta_h*(P_2(j)/(2*beta_h^3*Dh(1))*F12+
2*M_2(j)/(2*beta_h^2*Dh(1))*F13+thetaf(j)/beta_h*F14-2*u_h2sp(j)*F11);

Mh(i,j)=2*beta_h^2*Dh(1)*(P_2(j)/(2*beta_h^3*Dh(1))*F13+M_2(j)/(2*beta_h^2
*Dh(1))*F14-thetaf(j)/beta_h*F11-u_h2sp(j)*F12);
   Qh(i,j)=2*beta_h^3*Dh(1)*(P_2(j)/(2*beta_h^3*Dh(1))*F14-
2*M_2(j)/(2*beta_h^2*Dh(1))*F11-thetaf(j)/beta_h*F12-2*u_h2sp(j)*F13);

   Nxh(i,j)=p*(j-1)*r_h/2;
   Nth(i,j)=(u_h(i,j)+(Ah(1)-Ah(3)/2)/(4*beta_h^4*Ah(1)*Dh(1))*p*(j-
1))/r_h*(Ah(2)-(Ah(3))^2/Ah(1))+Ah(3)/Ah(1)*Nxh(i,j);
   Slih(i,j) = Nxh(i,j)/t_h+6*Mh(i,j)/(t_h^2);
   Sloh(i,j) = Nxh(i,j)/t_h-6*Mh(i,j)/(t_h^2);
   Stih(i,j) = Nth(i,j)/t_h+6*Dh(3)/Dh(1)*Mh(i,j)/(t_h^2);
   Stoh(i,j) = Nth(i,j)/t_h-6*Dh(3)/Dh(1)*Mh(i,j)/(t_h^2);
end
end


% --------------------------------------------------------------------------
% Stress Calculation in the shell part
% --------------------------------------------------------------------------
```

```
Slis=zeros(k,2);          % Longitudinal stress at inside surface of the
shell [MPa]
Slos=zeros(k,2);          % Longitudinal stress at outside surface of the
shell [MPa]
Stis=zeros(k,2);          % Tangential stress at inside surface of the shell
 [MPa]
Stos=zeros(k,2);          % Tangential stress at outside surface of the
shell [MPa]
xs=zeros(k,1);
u_s=zeros(k,2)            %Radial displacement [mm]
theta_s=zeros(k,2)        %Rotation
Ms=zeros(k,2)             %Moments [N.mm]
Qs=zeros(k,2)             %Shear forces [N]
Nxs=zeros(k,2)
Nts=zeros(k,2)

Rs = r_i+t_s/2;
for j=1:1:2
i=0;
for x = 0:l_s/(k-1):l_s
    i=i+1;
   xs(i)=x;

   f1= exp(-beta_s*x) * cos(beta_s*x);
   f2= exp(-beta_s*x) * (cos(beta_s*x)-sin(beta_s*x));
   f3= exp(-beta_s*x) * (cos(beta_s*x)+sin(beta_s*x));
   f4= exp(-beta_s*x) * sin(beta_s*x);

   u_s(i,j)= P_1(j)/(2*beta_s^3*Ds(1))*f1+ M_1(j)/(2*beta_s^2*Ds(1))*f2;
%   u_s(i,j)=(P_1(j)/(beta_s^3*Ds(1))*f1+ M_1(j)/(beta_s^2*Ds(1))*f2);
   theta_s(i,j)= beta_s*(-P_1(j)/(2*beta_s^3*Ds(1))*f3-
2*M_1(j)/(2*beta_s^2*Ds(1))*f1);

Ms(i,j)=2*beta_s^2*Ds(1)*(P_1(j)/(2*beta_s^3*Ds(1))*f4+M_1(j)/(2*beta_s^2*
Ds(1))*f3);
   Qs(i,j)=2*beta_s^3*Ds(1)*(P_1(j)/(2*beta_s^3*Ds(1))*f2-
2*M_1(j)/(2*beta_s^2*Ds(1))*f4);

   Nxs(i,j)=p*(j-1)*r_s/2;
   Nts(i,j)=(u_s(i,j)+(As(1)-As(3)/2)/(4*beta_s^4*As(1)*Ds(1))*p*(j-
1))/r_s*(As(2)-(As(3))^2/As(1))+As(3)/As(1)*Nxs(i,j);
   Slis(i,j) = Nxs(i,j)/t_s+6*Ms(i,j)/(t_s^2);
   Slos(i,j) = Nxs(i,j)/t_s-6*Ms(i,j)/(t_s^2);
   Stis(i,j) = Nts(i,j)/t_s+6*Ds(3)/Ds(1)*Ms(i,j)/(t_s^2);
   Stos(i,j) = Nts(i,j)/t_s-6*Ds(3)/Ds(1)*Ms(i,j)/(t_s^2);
end
end

% -------------------------------------------------------------------------
% Stress Calculation in the Flange
% -------------------------------------------------------------------------

xx=[xh xs+l_h];
```

```
i=1;
Sli(i,:)=[Slih(i,:) Slis(i,:)];
Slo(1,:)=[Sloh(i,:) Slos(i,:)];
Sti(1,:)=[Stih(i,:) Stis(i,:)];
Sto(1,:)=[Stoh(i,:) Stos(i,:)];

figure(1);
plot(xx,Sli(1,:),'b*-',xx,Slo(1,:),'r-^',xx,Sti(1,:),'m--
o',xx,Sto(1,:),'k-.s')
legend ('longitudinal inside','longitudinal outside','tangential
inside','tangential outside','Location','SouthEast')
set(findobj(gca,'type','line'),'MarkerSize',5)
grid on
title('Variation of stresses with length (Bolt-up)')
xlabel('axial position from ring, mm')
ylabel('Stress, MPa')

i=2;
Sli(i,:)=[Slih(i,:) Slis(i,:)];
Slo(i,:)=[Sloh(i,:) Slos(i,:)];
Sti(i,:)=[Stih(i,:) Stis(i,:)];
Sto(i,:)=[Stoh(i,:) Stos(i,:)];

figure(2);
plot(xx,Sli(2,:),'b*-',xx,Slo(2,:),'r-^',xx,Sti(2,:),'m--
o',xx,Sto(2,:),'k-.s')
legend ('longitudinal inside','longitudinal outside','tangential
inside','tangential outside','Location','SouthEast')
set(findobj(gca,'type','line'),'MarkerSize',5)
grid on
title('Variation of stresses with length (Pressurization)')
xlabel('axial position from ring, mm')
ylabel('Stress, MPa')


u=[uh us];

figure(3);
plot(xx,u(1,:),'b*-',xx,u(2,:),'r-^')
legend ('bolt up','Pressurization','Location','SouthEast')
set(findobj(gca,'type','line'),'MarkerSize',5)
grid on
title('Variation of displacement')
xlabel('axial position from ring, mm')
ylabel('Displacement, mm')

% -------------------------------------------------------------------------
```
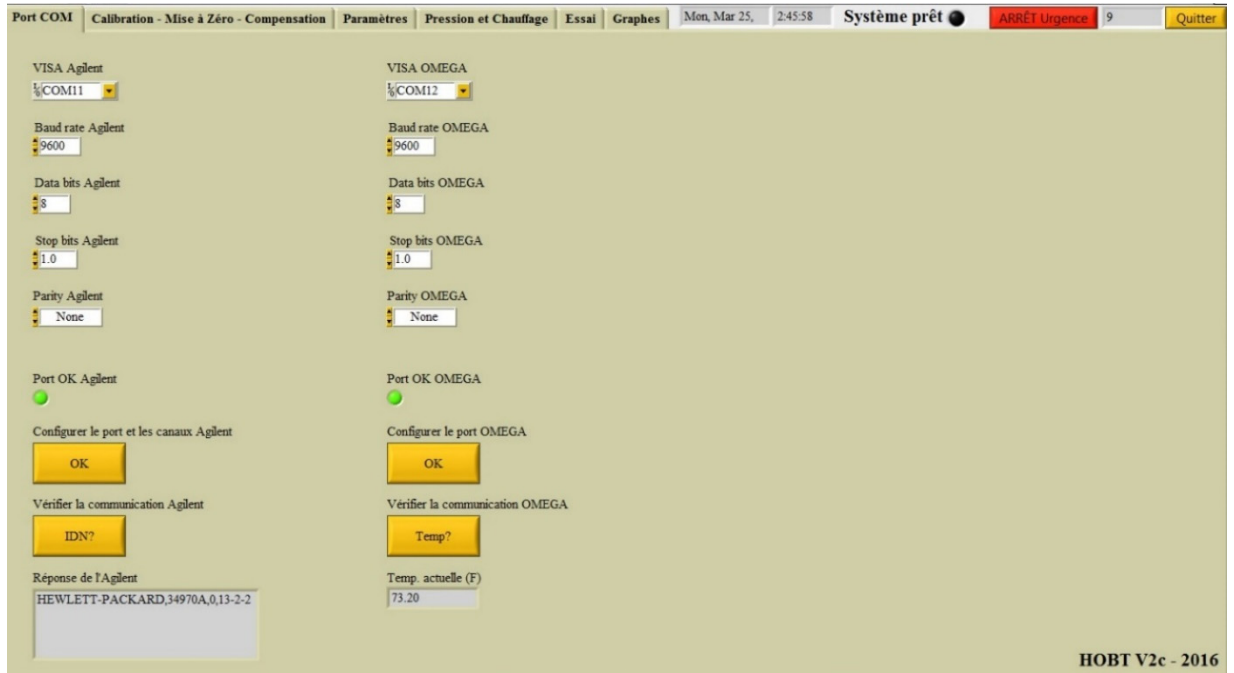
APPENDIX B

LabVIEW program

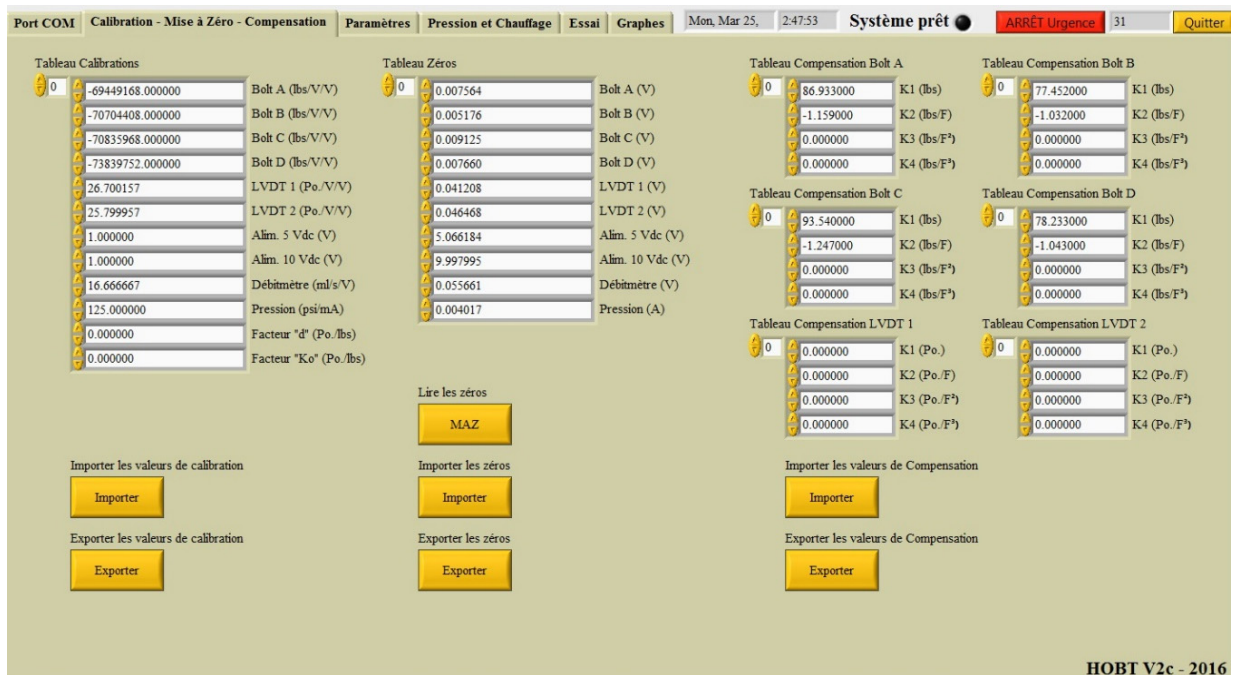Figure B-1 LabView graphical interface

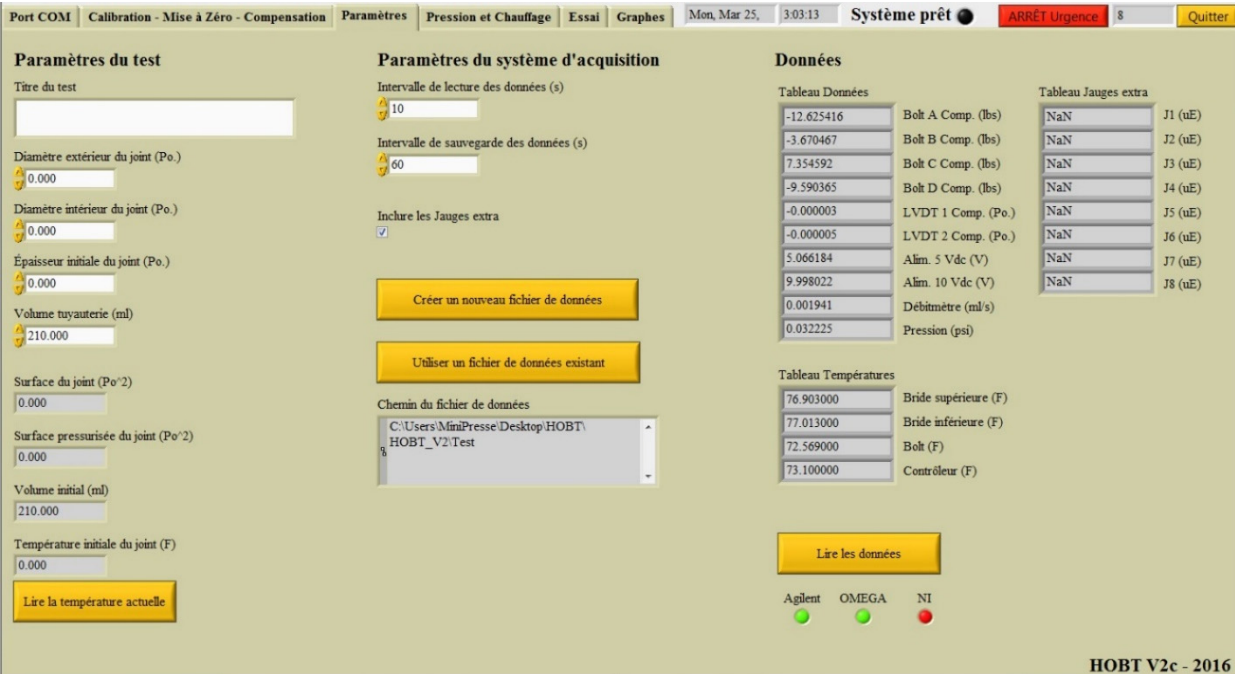Figure B-2 LabView graphical interface

Figure B-3 LabView graphical interface
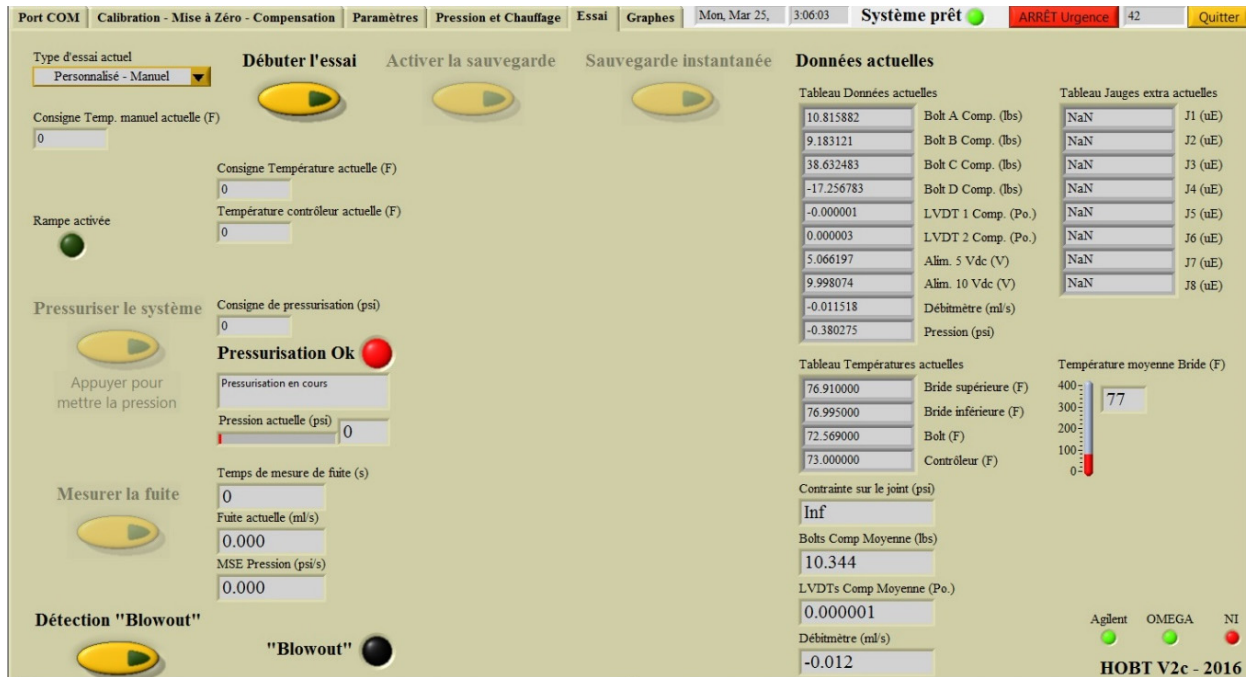

Figure 5-4 LabView graphical interface

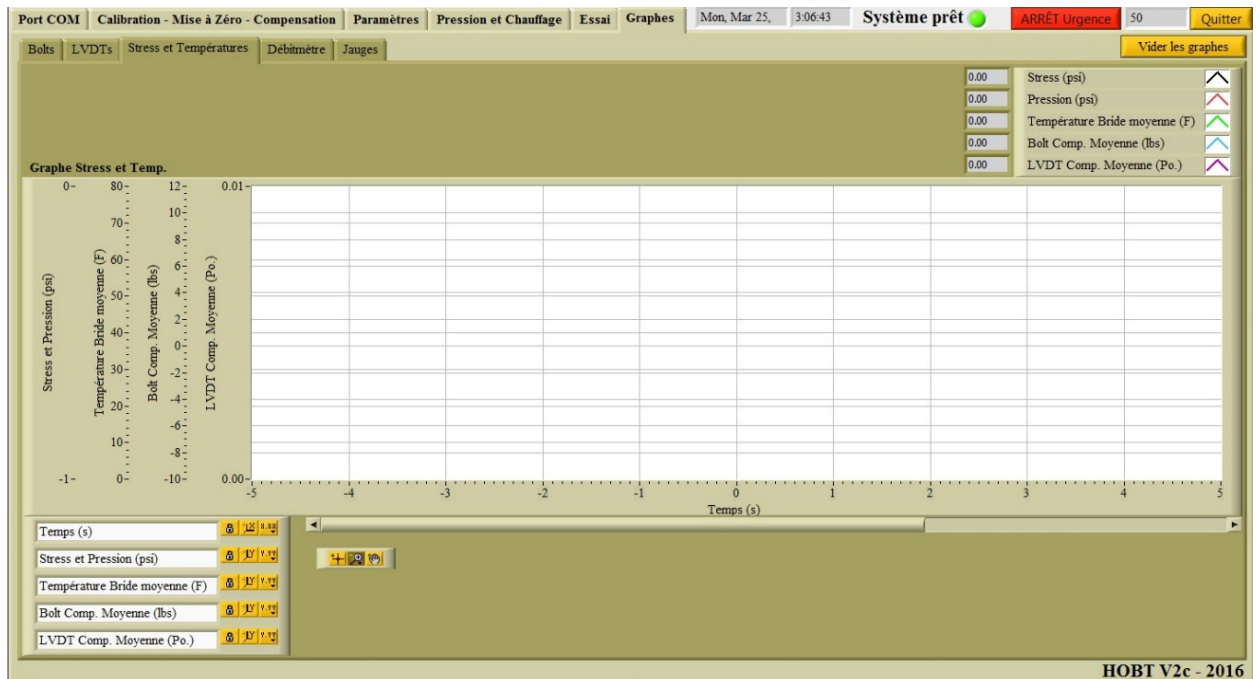Figure 5-5 LabView graphical interface
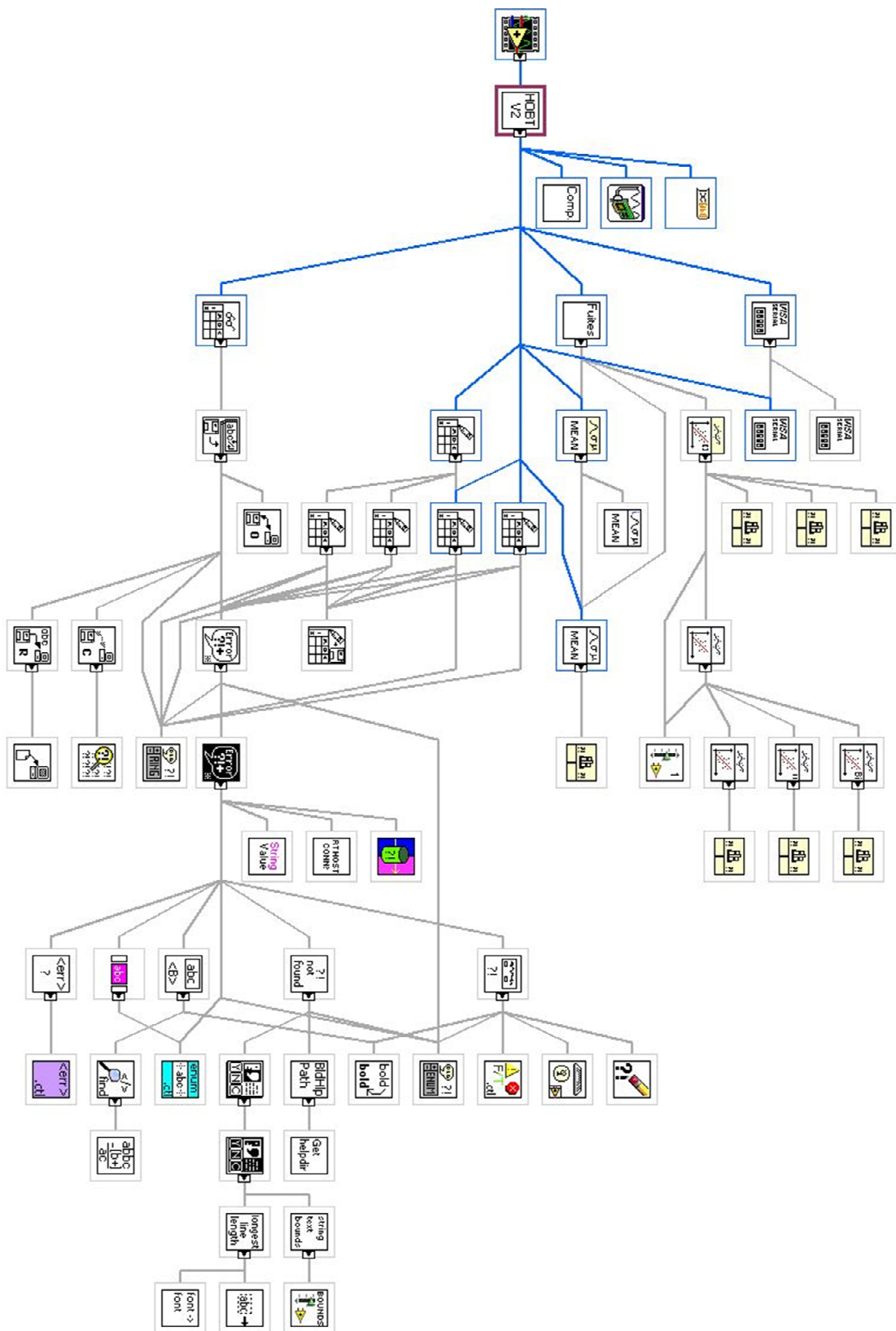

Figure 5-6 LabView graphical interface

Figure 5-7 VI hierarchy of the developed program

BIBLIOGRAPHY

Anonymous, (1979). *Modem Flanges Design, Taylor Forge Inc*., Engineering Department Bulletin No. 502, Chicago.

ASME Boiler and Pressure Vessel Code, Sections X, (2016) *Fiberglass Reinforced Plastic Pressure Vessels*. New York.

ASME/ANSI Standard BI6.5. *Pipe Flanges and Flanged Fittings*, New York.

ASME Boiler and Pressure Vessel Code, Section VIII-Division 2, New York.

ASME Boiler and Pressure Vessel Code, Section VIII-Division I, New York.

ASTM D5421, (2016). *Standard Specification for Contact Molded Fiberglass (Glass Fiber Reinforced Thermosetting Resin) Flanges*.

ASTM D4024, (2016). *Standard Specification for Machine Made Fiberglass (Glass Fiber Reinforced Thermosetting Resin) Flanges*.

ANSYS. (2016). ANSYS Workbench (Version 16.2). Standard manual, Ansys Inc.

Alkelani AA, Housari BA, Nassar SA., (2008). *A Proposed Model for creep relaxation of Soft gaskets in bolted joints at Room temperature*, Journal of Pressure Vessels Technology, pp. 130.

Bailey R.W., (1937). *Flanged Pipe Joints for High Pressure and High Temperatures*, Engineering, Vol. 144, pp. 364-365, 419-492, 538-539.

Blach, A.E., (1983). *Bolted Flanged Connections with Full Face Gaskets*, Ph.D. Dissertation, Ecole Polytechnique, Montreal, Quebec, Canada.

Blach, A.E., (1986). *Bolted Flanged Connections with Full Face Gaskets*, Welding research council bulletin No. 314, pp. 1-13.

Blach, A.E., Hoa S. V., (1988). *The Effects of Pull-Back on Stresses in FRP Flanges. Experimental Techniques,* Vol. 12, pp. 12-16.

Blach, A.E., (1988). *Fabrication and Use. Analytical and Testing Methodologies for Design with Advanced Materials*, Elsevier Science, pp. 349-358.

Blach, A.E., Sun L., (1990), *Fiber Reinforced Plastic Bolted Flanged Connections. Proceedings*, 2nd International Symposium on Fluid Sealing, La Baule, France, September, pp. 445-457.

Blach, A.E., Hoa S. V., (1987). *Bolted Flange Connections for Glass Fiber Reinforced Plastic Pipes and Pressure Vessels,* Proceedings 11th International Conference on Fluid Sealing, Cannes, France, pp. 642-661.

Blach, A.E., (1996). *FRP Bolted Flanged Connections Subjected to Longitudinal Bending Moments*, Computer-Aided Design in Composite Material Technology - International Conference, p 11-20.

Blach, A.E., Bazergui, A., and Baldur, R., (1986). *Full Face Gasketed Bolted Flange Connections*, Weld. Res. Counc. Bull., 314, May.

Blach, A.E., Hoa, S.V., (1988). *Effects of Pull-Back on Stresses in FRP Flanges", Experimental Techniques*, v 12, n 11, p 12s-16s, Nov.

Bouzid A., Chaaban, A., and Bazergui, A., (1994). *The Effect of Gasket Creep Relaxation on the Leakage Tightness of Bolted Flanged Joints*, ASME J. Pressure Vessel Technol., 117, pp. 71–78.

Bouzid A., Chaaban A., (1993). *Flanged joint analysis: A simplified method based on elastic interaction*, CSME Transactions, Vol. 17, No. 2, pp.181-196.

Bouzid A., Nechache A., (2005), *An Analytical Solution for Evaluating Gasket Stress Change in Bolted Flange Connections Subjected to High-Temperature Loading*, J. Pressure Vessel Technol. 127(4), 414-422.

Bouzid A., (1994). *Analysis of bolted flanged gasketed joints*, Ph.D. Dissertation, Ecole Polytechnique de Montreal.

Bouzid A. and Galai H., (2011*). A New Approach to Model Bolted Flange Joints with Full Face Gaskets*, ASME Journal of Pressure Vessel Technology, 133 (2), 021402-6.

Budynas, R. G., Nisbett, J. K., & Shigley, J. E. (2011). *Shigley's mechanical engineering design*. New York: McGraw-Hill.

Campbell J.M., (1990). *FRP Flange for Process Pipe and Tanks,* Proc. FRP Symposium, National Association of Corrosion Engineers, Niagara Frontier section, USA.

Cook R. D., Young W. C., (1985). *Advanced Mechanics of Materials*, Macmillan Publishing Company.

Currie R. D., (1993). *Glass Reinforced Polyester Pipe Engineering and Usage*, C4591024 IMechE, pp 107-116.

Cheremisinoff N. P., (1978). *Fiberglass-Reinforced Plastic Deskbook*. Ann Arbor Science Publishers, Inc.

Conlinsk, P. (2006). *Fiber-reinforced plastic pressure vessels and ASME RTP-1-Reinforced thermoset plastic corrosion-resistance equipment*, Companion Guide to the ASME Boiler & Pressure Vessel Code, Vol. 2. New York.

Cratchley D., Clifford N. J., (1971). *Four Glass Reinforced Thermosetting Resins for Pipeline Applications. Design with Composite Materials*, Institution of Mechanical Engineers.

Derenne, M., Marchand, L., Bouzid, A., and Payne, J. R., (2000), *Long Term Elevated Temperature Performance of Reinforced Flexible Graphite Sheet Gaskets*, Proceedings of the ICPVT-9 Conference, Vol. 2, Operation, NDE, Failure Analysis, Codes, Standards and Regulations, Sydney, Australia, pp. 229–247.

Dynaflow research group, (2011). GRP Flanges design & assessment, Rotterdam

Estrada H., (1997). *A Fiber Reinforced Plastic Joint for Filament Wound Pipes: Analysis and Design*, Ph.D. Dissertation, University of Illinois.

Estrada H., Parsons I.D., (1999). *Strength and Leakage Finite Element Analysis of A GFRP Flange Joint*, International Journal of Pressure Vessels and Piping 76, 543–550

Estrada H., Parsons I.D., (1996). *A GRP Pipe Joint for Filament Wound Pipes: Strength Analysis and Design. Pressure Vessels and Piping Design, Analysis, and Severe Accidents,* ASME, PVP-Vol. 331, pp. 13-19.

EN 1591-1, (2013). *Flanges and their joints. Design rules for gasketed circular flange connections*, Calculation, European Normalization.

Facca, A.G., Kortschot, M.T., and Yan, N., (2007). *Predicting the tensile strength of natural fiber reinforced thermoplastics*, Compos. Sci. Technol., 67 (11), pp. 2454-2466

Graham T. E., (1989). *FRP Flange for Process Pipe and Tanks. In Managing Corrosion with Plastics*, Tenth Biennial Symposium, 1989, San Antonio TX.

Hoa S. V., (1991). *Analysis for Design of Fiber Reinforced Plastic Vessels and Piping*, Technomic Publishing Co., Inc.

Hyer M. W., White S. R., (2009). *Stress Analysis of Fiber-reinforced Composite Materials,* DEStech Publications, Inc.

Jones R.M., (1980). *Mechanics of Composite Materials*. McGraw-Hill Book Company, New York.

Kurz H., Roos E., (2012). *Design of Floating Type Bolted Flange Connections with GRP Flanges*, International Journal of Pressure Vessels and Piping 89, 1e8.

Leon G. F., Chew D. K., Widera G. E. O., Short W. E., (1995). *Comparison of International Design Rules for Plastic Bolted Flange Connections*. Current Topics in Computational Mechanics, pp. 189-203, ASME PVP vol. 305.

MATLAB. (2017). MATLAB (R2017b). MathWorks.

Muscati A., Blomfield J. A., (1977). *Full-Scale Burst Tests on GRP Pipes. Designing with Fiber Reinforced Materials*, Institution of Mechanical Engineers, pp. 7-10.

Mackerle J., (2003). *Finite Element Analysis of Fastening and Joining: A Bibliography (1990-2002)*, International Journal of Pressure Vessels and Piping, Volume 80 (4), pp. 253-271.

National Bureau of Standards Voluntary Product Standard, PS 15-69, Custom Contact Molded Reinforced Polyester, Chemical-Resistant Process Equipment.

Nechache A, Bouzid A., (2007). *Creep Analysis of Bolted Flange Joints*, International Journal of Pressure Vessels and Piping 84, 185–194

Nechache A., Bouzid A., (2003). *The Determination of the Load Changes in Bolted Gasketed Joints Subjected to Elevated Temperatures*, in Proceedings of the ASME-PVP Conference, PVP2003–1883, Cleveland, Ohio, pp. 139–148.

Nassar, S. A., Abboud, A., (2009). *An Improved Stiffness Model for Bolted Joints*. ASME Journal of Mechanical Design, 131 (12), pp. 121001-11.

Roy A. Parisher, Robert A., (2011). *Rhea Pipe Drafting and Design, Chapter 4*, Flange basics.

Rudolph S., (2004). *Theory and Analysis of Plates, Classical and Numerical Methods,* Hoboken, NJ: Wiley, 2004, 1024p.

Rosato D. V., Grove C. S., (1964). *Filament Winding,* Wiley, New York.

Sun L., (1995)., *Bolted Flanged Connections Made of Fiber Reinforced Plastic Materials*, Ph.D. Dissertation, Concordia University, Montreal, Canada.

Takaki, T. (2004). *Effects of Flange Rotation on the Sealing Performance of Pipe Flange Connections*, Paper Presented at the Proceedings of the ASME/JSME Pressure Vessels and Piping Conference, San Diego, CA, USA.

Timoshenko, (1930). *Theory of plate and shells*, NY, J. Wiley.

Tsai S.W., (1987). *Composite Design. Think composites*, Dayton, Ohio, USA, third edition.

Zahavi E., (1993). *A Finite Element Analysis of Flange Connections*, ASME Journal of Pressure Vessel Technology, 115:327-330.

164